Spitzer Space Telescope observations of hot Jupiters

Deepak Prakash Mahtani

This thesis is submitted to Keele University for the degree of Doctor of Philosophy

School of Physical and Geographical Sciences, University of Keele.

December 2015

Abstract

Currently the Spitzer Space Telescope is the most reliable telescope for conducting secondary eclipse observations of exoplanets. The depth and the time of mid-eclipse are two important parameters that come from a secondary eclipse analysis. The eclipse depth gives information on the temperature of the atmosphere, and can provide evidence for the presence of molecules in the atmosphere of the planet. If multiple wavelengths have secondary eclipse depths measured then it is possible to constrain the spectral energy distribution (SED) of the atmosphere given some assumptions on, for example, the metallicity of the planet's atmosphere. The time of mid-eclipse gives $e\cos(\omega)$ which, with an analysis including transit, radial velocity and secondary eclipse data, can strongly constrain the eccentricity of the planet's orbit. To fully understand the conclusions drawn from these two parameters realistic error bars must be quoted on the measurement of these parameters. It is generally understood that error bars that come from MCMC analyses of secondary eclipse observations are underestimated because the correlated noise in the data is not accounted for in the analysis. The goal of this thesis was to find a method to improve the estimates of the uncertainties on these two parameters as derived from Spitzer secondary eclipse lightcurves at $3.6\,\mu$m and $4.5\,\mu$m. This work was conducted through the generation and fitting of semi-synthetic Spitzer secondary eclipse light curves. I estimate the amount the uncertainties on these parameters need to be inflated by and show how my results compare with other similar work in the field. I show that the amount of inflation does affect the conclusions drawn when fitting these data with model atmospheres. This could also mean that for systems where complex chemistry is invoked to explain the observed data, simpler model can now fit the data due to the increase in the error bars. I also find that when multiple realisations of the same, simulated, secondary eclipse lightcurve are fit with the standard MCMC code, the amplitude and time of mid-eclipse can be recovered and found to be more than 3σ away from the true value of the injected signal. This can mean that, because usually only 1 lightcurve is obtained per observation of the secondary

eclipse, some detections of eccentricity and molecules may not be real detections but simply a result of noise in the data.

Acknowledgements

To be able to thank all those who need to be mentioned here would require more pages than are in this thesis. If you are not mentioned here it is not because you have been forgotten, I promise.

First, I must thank my family. They have supported me in following my dreams, and without their love and support I would not be here writing this. So thank you all so much, I love you all.

To my supervisor, Dr Pierre Maxted, it has been a pleasure and an honour to have worked with you over the past few years. During my time here you have given me the opportunity to do things that some people only dream of, whether that be sitting 2500m above sea level, using millions of pounds worth of telescope or climbing in the foothills of Mt Teide, I have enjoyed every moment of it. I thank you from the bottom of my heart, my friend.

To my fellow Ph.D students and Keele friends, everyone one of you has helped me get to this point, you are all like family. We have had many memorable times together, and those memories will remain with me forever. From the KPA lunches, to the nights out together, we always have a fantastic time. When I was at my lowest you all helped me recover, and now I am my happy go lucky self again. Thank you for everything guys!

To the KPA and everyone who runs, works at and frequents the clubhouse, I cannot thank you enough for being so awesome, whether I was their for the quiz, watching sports or just having a drink with you, every moment I spent in with you all was amazing. Thanks to you all, I am going to miss you!

To the Keele astrophysics department, you all made me feel so welcome from day 1. I have had so much fun being part of such an amazing department. The curry nights, coffee times, everything has been amazing. So many laughs, I will miss you all so very much. A special thanks must go to a Barry, even when I managed to crash the network you still laughed. No matter how stupid I have been you always know how to

make me laugh. Joana and Jacco, you both were there for me whenever I needed you, I cannot thank you enough.

To the University of Sheffield Physics and Astronomy, and Mathematics departments, I could not have imagined when I was first accepted on to the course that I would be here now 8 years later writing this. No matter how many questions I asked, no matter how stressed I got, each and everyone of you gave me time and for that I owe you all so very much. I would not be here now if it were not for all of you. I must mention my two supervisors, Stuart and Simon, you both made even the most complicated of topics seem simple, without either of you I could not have believed that I could get here. Carsten, whether we were discussing the latest apple products or talking science, we always had fun, thank you for just being awesome. Susan, thank you so much for telling me when to stop and relax, no matter how much I was over thinking things you knew that I was going to be fine. Ed, thank you for all your advise and guidance both as my advisor and my friend. Thank you all so very much for giving me the opportunity to begin this most amazing adventure.

To the Sheffield Sabres, without everyone of you, I would not have had such a great time as an undergrad. So many memories on and off the field, you all showed me that with hard work, dedication and persistence, everything is possible. Live, breathe, bleed, black and gold!

To my friends at the University of Sheffield, we had some great times. From the nights out at the union, to the long days in the IC. Thanks to you all for being amazing friends!

A very special thank you must go to Dr Rob Jackson, for proofreading through this thesis for me. You are a star!

Contents

List of Figures

List of Tables

1 Introduction

Prior to the discovery of an exoplanet orbiting a Sun-like star (Mayor & Queloz 1995), it was assumed that planetary systems would look like our own Solar System with small rocky bodies close to their parent star and bigger gas giants further away. However, the planet that was discovered, 51 Peg b, is a Jupiter analogue that orbits its host star in 4 days. These analogues are now known as hot Jupiters. This discovery was surprising because in the simple theory of planet formation (core accretion) there is not enough solid material in these regions to form hot Jupiters insitu.

Currently, more that 1500 exoplanets have been detected[1]. With advances in technology we are able now to start characterising hot Jupiters by analysing their atmospheres. There are two main methods that are used to analyse the atmospheres of hot Jupiters, transmission spectroscopy and secondary eclipse photometry. Transmission spectroscopy requires observations of the transit at multiple wavelengths, looking for radius variations in the measured transit depth. These are indicative of stratification of exoplanet atmospheres because different gases exist at different altitudes in the atmosphere. Secondary eclipse photometry uses observations of the secondary eclipse at multiple wavelengths to look for changes in the eclipse depth which would be indicative of extra absorption or emission from opacity sources in the planet's atmosphere. These secondary eclipse observations produce a low resolution, hemispherically averaged spectral energy distribution (SED) of the day-side of the planet.

Given the quality of current data we are on the cusp of being able to detect Earth analogues. Missions such as the Kepler Space Telescope (Borucki et al. 2010) and CoRoT (Rouan et al. 1998; Moutou et al. 2014) have found several candidates but they are very hard to follow up because the stars are very faint. However, before we can begin to understand these small, potentially habitable worlds we first need to be able to understand the giant planets that can be followed up. Studying the atmospheres of hot Jupiters can provide some very interesting information, such as constraints on

[1] http://exoplanet.eu

the chemical compositions of their atmospheres. The Spitzer Space Telescope has been the main source to-date of secondary eclipse observations. These observations are conducted in the infrared because it is closer to the peak of the planet's emission ($\sim 1\,\mu$m). The chemical composition and thermal structure of the atmosphere dictates the emergent spectrum. Different opacity sources exist at different regions (depths) of the atmosphere. As I will show later in this chapter by using the remaining wavelengths available on *Spitzer* it is possible to probe different regions of the atmosphere.

Spitzer was not designed to conduct these (single star) observations. It was designed to take images of large regions of the sky. As such the detectors have large pixels and suffer from intra-pixel sensitivity variations (IPSVs). This means that different regions of the same pixel will have a different sensitivity to the light that is incident upon the pixel. This would not be an issue if the PSF of the star were to remain at the same position on the detector throughout the observation. However, there is a battery heater that is turned off and on every half an hour that induces movement in the instruments which then produces a small (but non-negligible) shift in PSF position. This results in the variations in flux measured and these can be significantly larger than the signal of the secondary eclipse. One method often used to account for IPSVs is to model them as a polynomial function of the x and y coordinates of the star on the detector. The best fitting parameters for both the IPSV model and the eclipse shape are found simultaneously using a Markov Chain Monte Carlo (MCMC) algorithm. One of the main issues is that the MCMC code assumes that the lightcurve is made up of independent points with Gaussian errors (i.e., white noise). This is not the case in reality. There are many sources of correlated noise in the data which can induce systematic errors in the data, such as stellar noise. The goal of this thesis is to find a simple method of inflating the error bars on the depth of the secondary eclipse and time of mid-eclipse such that they account for the correlated noise present in the data. The reason I have chosen to use these two parameters is that the depth of the secondary eclipse provides information on the chemical composition of the atmosphere and also its thermal structure. The time of mid-eclipse constrains $e\cos\omega$, where e is the eccentricity of the planets orbit and ω is the argument of periastron. With constraints

on both $e\cos\omega$ and $e\sin\omega$, which comes from the radial velocity observations of the star, it is possible to constrain the eccentricity of the system. The chemical composition of the atmosphere gives information about the gas in the protoplanetary disc from which the atmosphere was accreted. This may be able to help understand where in the disc these hot Jupiters formed, which is currently an active area of research (Dawson, Murray-Clay & Johnson 2015).

The structure of this thesis is as follows. Chapters 1 and 2 give an overview of the field of exoplanets, the methods used to find them and analyse their atmospheres. Chapter 3 presents a state-of-the-art analysis of *Spitzer* data covering the secondary eclipse of a WASP-26b. The results of this work were published in MNRAS (Mahtani et al. 2013). In Chapter 4 I present my reanalysis of the WASP-12b thermal phase curves. In chapter 5 I present work where I used part of the HAT-P-2b phase curve (Lewis et al. 2013) to conduct signal injection of secondary eclipses to estimate of the instrumental noise of the IRAC detectors. Chapter 6 presents an analysis of *Spitzer* photometry covering the secondary eclipse of WASP-35b, including error estimates of the parameters derived using the techniques developed in Chapter 5. Chapter 7 gives my conclusion and future work prospects.

1.1 Planet formation

The core accretion theory of planet formation predicts that Jupiter analogues are formed from 10 Earth-mass cores which then accrete gas from the protoplanetary disc (Helled et al. 2013). However, the inner regions of young star systems, where hot Jupiters are found, are very hot and as such only dust grains that have high melting points (heavy elements such as iron) will be in solid form (Finkbeiner 2014). Using the Sun as an example, only 1.4% of the solar composition (by mass) is made up of metals (Asplund et al. 2009) and, for example, of this only 0.14% is in the form of iron[2]. The

[2]http://csep10.phys.utk.edu/astr162/lect/sun/composition.html

planets in our Solar system formed from the same material so only a small fraction of material is in the form of solids very close to the star. Combining the masses of the inner planets in the solar system, there is only about $2M_{\oplus}$ of material (Carroll & Ostlie 1996). These two reasons show that there is not enough mass in solid form to form the minimum core mass for gas accretion. Another argument against in situ formation of hot Jupiters is that the gas is going to be very hot in these regions around the host star. Assuming the following;

1. A 10 Earth-mass core is placed at 0.04 AU (the distance of WASP-26b from its host star, Mahtani et al. 2013),
2. The 10 Earth-mass core has a similar density to the Earth (5514 kgm^{-3}) and hence a radius of $13,723.76$ km,
3. The typical temperature for a hot Jupiter atmosphere is ~ 1500 K,
4. The most abundant element in hot Jupiter atmospheres is hydrogen so, for this order-of-magnitude calculation, we assume that the atmosphere is composed purely from molecular hydrogen

Thermal escape of the gas molecules will occur if the escape velocity of the core is less than 10 times the root-mean-square (RMS) velocity of the gas molecules. The escape velocity of the core is given by $\sqrt{2GM/R}$ where G is the gravitational constant, M is the mass of the core, and R is the radius of the core. The RMS velocity of the gas is given by $\sqrt{3kT/m}$ where k is Boltzmann constant and T is the temperature of the gas and m is the molecular mass of the gas. Using the assumptions and equations above the RMS velocity of the gas is ~ 4.3 $\mathrm{km\,s}^1$ and the escape velocity of the core is ~ 24.1 $\mathrm{km\,s}^1$, hence the escape velocity of the core is less than 10 times the RMS of the gas. So if a large rocky core were to be placed very close to its host star, the gas molecules would be too hot to be accreted on to the planetesimal.

Planetary migration has been proposed as a mechanism to explain why hot Jupiters exist. This theory predicts that these planets form at distances where there is

enough rocky material (Finkbeiner 2014) and volatiles such as water, carbon dioxide and ammonia in solid form which coagulate to form the cores of these giant planets[3]. At these distances from the host star the gas is not as hot as in the inner regions so the solid cores are able to accrete gas from their surroundings. Planets are thought to migrate inward due to interactions with the disc. Observations show that there is a build up of hot Jupiters in 3-5 day orbits (Baruteau et al. 2014). The mechanism that stops planets migrating further in and being devoured by their host star is still an open question in the field.

1.2 Methods for Finding Planets

1.2.1 Radial Velocities

There are several methods that are currently being used in planet hunting projects. The method that is finding the most planets is the radial velocity (RV) method. For simplicity consider a single planet system. In this two body scenario, both the planet and the star orbit their common centre of mass (barycentre). As the star orbits the barycentre, it moves both away and toward the observer. This oscillatory motion of the star along the observer's line of sight, causes the light to be red and blue shifted. By taking multiple spectra of the star, this motion can be detected from the oscillation of the stellar spectral lines about their rest frame position. This is a measure of how fast the star is moving towards and away from the observer (its RV). Figure 1.1 is an example of a RV curve that is generated with these observations.

[3]The distance from a star where a volatile condenses is known as the snow line

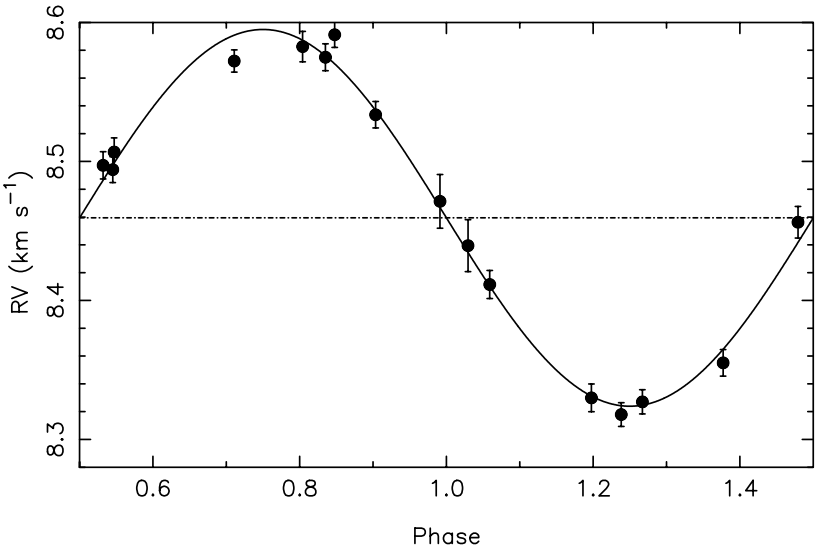

Figure 1.1: RV curve of WASP-26 (Smalley et al. 2010). The points with error bars are the measured radial velocities with their standard errors. The solid black line shows the best fitting model to the data. In the analysis it was assumed that the planet was on a circular orbit. The dotted line is the barycentre velocity.

With the RV data and Kepler's third law we are able to derive equation 1.1, which gives the minimum mass of the planet.

$$M_P \sin i = \frac{K_\star M_\star P \sqrt{1-e^2}}{2\pi a} \tag{1.1}$$

$K_\star$ is the semi-amplitude of the radial velocity of the star, $M_\star$ is the mass of the star, P is the period and a and e are the semi-major axis and eccentricity, respectively, of the planet's orbit. The $\sin i$ term on the left hand side of equation 1.1 is due to the unknown inclination of the planet's orbit. Finding exoplanets with this method is most sensitive to massive planets orbiting very close to their host stars (i.e., hot Jupiters) because these planets induce the biggest RV shifts in their host stars. Most hot Jupiters are observed to have orbits with 3-4 day periods. The shorter a planet's period, the closer to its host star the planet orbits. For comparison, Mercury's orbital period is

88 days, semi-major axis of $\sim$ 0.4AU and a typical hot Jupiter has an orbital period of $\sim$ 3 days and semi-major axis of $\sim$ 0.01 AU. To achieve the precision and accuracy in the RV measurements needed to detect extrasolar planets requires specialised instrumentation, e.g., echelle spectrographs that are very stable and that can achieve very high resolution. For example WASP-26b induces a maximum radial velocity shift of only 0.1355 ± 0.0035 kms^{-1} on its host star. The shift of the spectral line on the detector is incredibly small (e.g., for WASP-26b the shift of the Hydrogen α line is 1/10 of a pixel [4]) and so to be able to detect such a small shift high resolution data is required. The first way to obtain precision is to simultaneously observe a calibration source, where the spectral line positions are known very accurately, during each exposure. This is the method used by the CORALIE and ELODIE spectrographs. It is possible to push the technology one step further and to make the spectrograph extremely stable by putting inside a vacuum container which can significantly reduce spurious wavelength shifts due to variations in temperature or atmospheric pressure. Due to the magnitude of the signal being so small the signal needs to be averaged over many spectral lines, so the star needs to have many well defined spectral lines in the wavelength range at which it is being observed. This problem is further complicated when considering massive stars (spectral type earlier than F6V). These stars have temperatures hotter than about 6500K and are more massive than about $1.4\,\mathrm{M}_{\odot}$. Many of the metals in the atmospheres of these stars are highly ionised. This means that they have very few well defined spectral lines (in the optical region of the electromagnetic spectrum). They do, however, have lines in the UV region of the electromagnetic spectrum. The atmosphere is almost opaque to this radiation so in practice it is hard (but not impossible) to do UV radial velocity searches of early type stars. Not only that, they usually rotate very fast, $\geq$ 20kms^{-1} (Gray 2005). This causes the lines that are observable to be rotationally broadened. This broadening of the spectral lines increases the uncertainty in their measured position and hence on the measured radial velocity of the star.

[4]The HARPS north pixel size is $15\,\mu$m http://www.tng.iac.es/instruments/harps/

If we are looking for life as we know it, we need to find an Earth-like world. This is no easy task. Looking at this from a RV perspective, the RV induced in a solar mass star by an Earth mass planet at 1AU is about 9cms^{-1} (Seager & Dotson 2010). With the best instrumentation currently available, e.g., High Accuracy Radial velocity Planet Searcher (HARPS-North), the precision that is achievable is about 0.3ms^{-1} (Cosentino et al. 2012). However, the most important source of noise that needs to be considered here is the star itself. Convective cells are constantly appearing and disappearing on the surface of stars like the sun. This can induce signals on the order of a few cm s^{-1} (Cegla 2013). The major issue is that this does not average out over the whole disc of the star. This can hinder the search for Earth-like worlds by either masking their signals under the noise or mimic their signal. Dumusque et al. (2011) suggested that the following method can help to beat down the noise in the data in order to get better precision on the measurements of the RVs. In the months that the target is observable, data over 10 consecutive nights must be taken. Every night at least 3, 10 minute exposures separated by 2 hours are required. However, Cegla (2013) explained that this leaves residual signal of the granulation signature in the data. Hence, it may not be possible to reach precision required to find an Earth analogue around a solar-like star using this method. This result, however, is a step in the right direction, because to reach the precision required to find Earth like planets we need to fully understand the effects of the host star.

If there are multiple planets in the system then the RV curve will be much more complicated. Figure 1.2 shows the RV curve of HD10180 (Lovis et al. 2011). It was found that the best fit to the data is a 7 planet system.

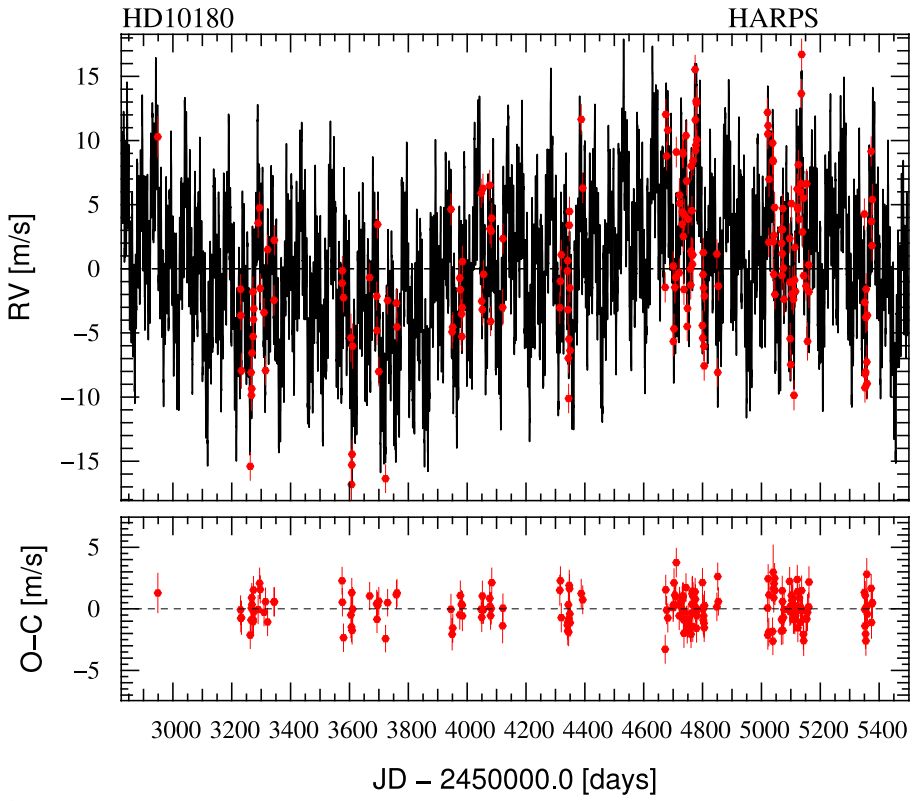

Figure 1.2: RV curve of the HD 10180 system (Lovis et al. 2011). This system contains 7 planets. The red points with error bars are the data that were acquired and the black line is the best fitting model. The lower panel shows the residuals.

Another case is that the planet(s) may be on an eccentric orbit. The RV curve for an eccentric planet is be more saw-tooth shaped than sinusoidal. The reason for this is that the planet's orbital speed is not constant. When the planet is closest to its host star (periastron) it moves quickly and induces a large radial velocity in the star. The opposite is the case when the planet is further away from the star (apastron). An example of a planet on an eccentric orbit is HD156279b, which has an eccentricity of 0.708 ± 0.018 (Díaz et al. 2012). The RV curve for this planet is shown in Figure 1.3.

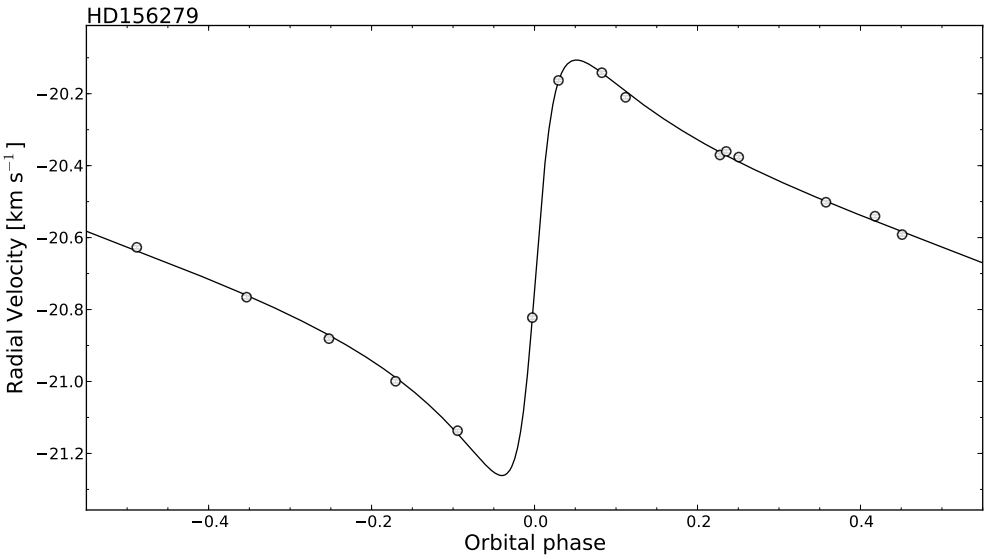

Figure 1.3: RV curve of HD 156279 which hosts an eccentric exoplanet (Díaz et al. 2012). The open white circles are the data and the black line is the best fitting model with $e = 0.708 \pm 0.018$.

1.2.1.1 Rossiter McLaughlin Effect

The angle between the rotation axis of the star and the normal to the orbital plane of the planet is known as the spin-orbit angle, or the obliquity. In the model of planet formation (core accretion) planets form from the disc of dust and gas orbiting the young star. From this theory it is expected that the spin-orbit angle is very close to zero. If the planet transits it is possible to measure the sky project spin-orbit angle by observing the Rossiter-McLaughlin effect (Rossiter 1924; McLaughlin 1924; Anderson et al. 2011a; Kaib, Raymond & Duncan 2011; Albrecht et al. 2011). The star itself is rotating on its axis. This means that the light from one side of the stellar disc is red shifted and light from the other side is blue shifted. A schematic of this is shown in Figure 1.4.

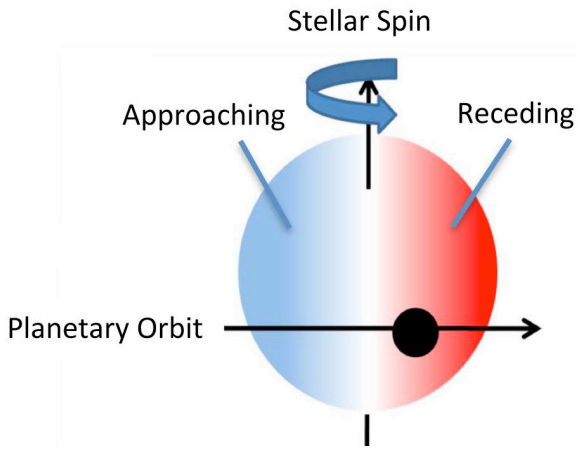

Figure 1.4: Schematic showing the Doppler shift in the star light caused by the stellar rotation. This figure has been adapted from figure 1 of Subaru Telescope Press Release (2011).

During transit the planet will block different amounts of this red/blue shifted light. Observing the transit spectroscopically allows us to see this as an anomaly in the RV curve. By measuring this anomaly it is possible to determine the sky-projected spin-orbit angle. For simplicity assume the inclination of the system is 90° and that the planet orbits the star in a prograde manner. Between ingress and mid transit the planet will block a portion of the blue shifted light of the star. So there will be an excess of red shifted light. This means the RV anomaly measured will be positive. At mid transit the planet is blocking equal amounts of red shifted and blue shifted light so there is no RV anomaly measured. From mid transit to egress the planet blocks some of the red shifted component of the light, so there is an excess of blue shifted light. This means the RV anomaly is negative. It is also possible to understand if the planet is in a prograde or retrograde orbit. If the planet is in a prograde orbit then the positive RV anomaly will precede the negative RV anomaly. If the planet is in a retrograde orbit then the opposite occurs. Figure 1.5 shows the RV anomaly for WASP-22b as measured by Anderson et al. (2011a).

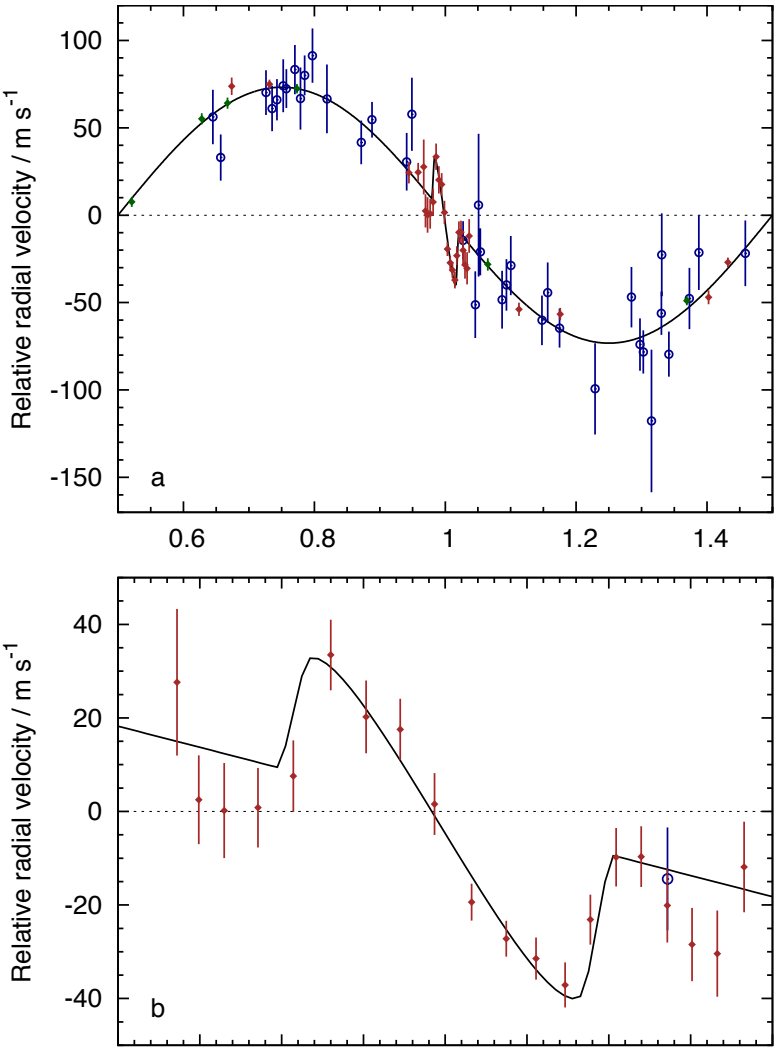

Figure 1.5: RV curve of WASP-22 (Anderson et al. 2011a). This shows that WASP-22b is in a prograde orbit (the positive RV anomaly precedes the negative RV anomaly). The shape and amplitude of the anomaly imply that the sky-projected spin-orbit angle is $22 \pm 16°$.

Depending on the sky-projected spin-orbit angle of the system, the amplitude of positive and negative RV anomaly detected will change. Equal amounts of RV anomaly means the sky-projected spin-orbit angle is approximately 0 or 180 degrees. Figure 1.6 shows how the RV anomaly changes depending on the sky-projected spin-orbit angle.

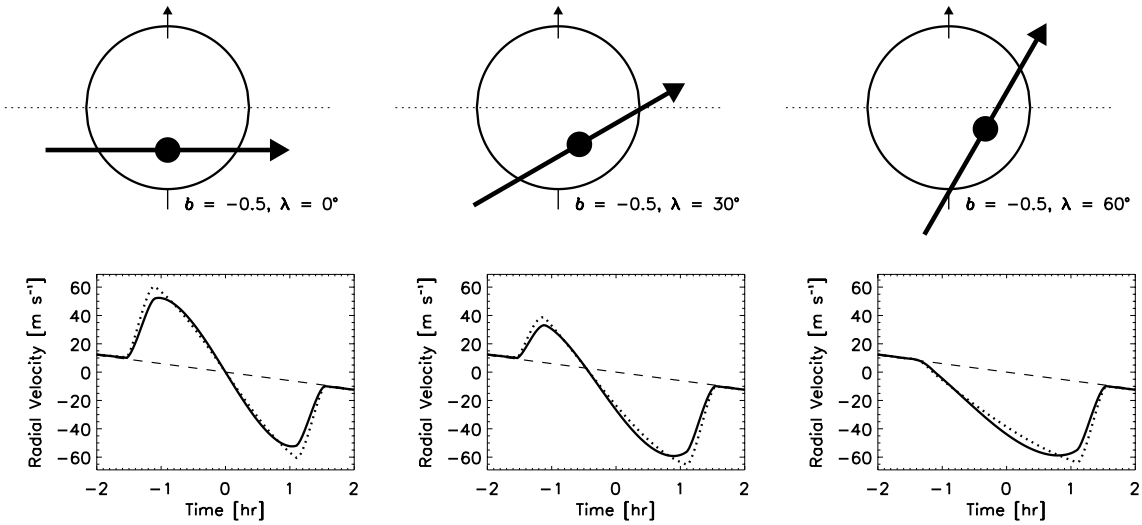

Figure 1.6: Examples of the different forms of the RM effect that can be observed (Gaudi & Winn 2007). b in the diagram is the impact parameter and λ is the sky-projected spin-orbit angle.

In total 82 planets have had their R-M effect observed and measured (Southworth 2011a). There are some that have very high sky-projected spin-orbit angles, and some even in retrograde orbits around their stars (e.g. WASP-17b Anderson et al. 2010). The cause of this is not well understood but there are several theories that have been proposed. These include gravitational instabilities caused by other planets in the system (planet-planet scattering) or by companion stars to the host stars (Kozai Mechanism, Kozai 1962; Rasio & Ford 1996.)

1.2.1.2 Radial Velocity Surveys

The two best-studied transiting extrasolar planets are HD 209458b and HD 189733b. Both of these planets were discovered using radial velocity surveys. HD 209458b was discovered by the Keck Doppler survey (Henry et al. 2000). HD 189733b was dis-

covered by the ELODIE metallicity-biased search for transiting Hot Jupiters (Bouchy et al. 2005). These two planets were subsequently found to transit, which has enabled extensive follow up observations to investigate their atmospheres. Radial velocity surveys are very successful at finding planets because even if a planet does not transit the radial velocity induced in the star may still be detectable. From these observations the minimum mass of the secondary is derived which is fundamental, as will be seen in the next section, to understanding the kind of planet being observed. Recent surveys such as HARPS in the Northern (Cosentino et al. 2012) and Southern Hemispheres (Mayor et al. 2003) have improved the precision of radial velocity measurements for bright solar-type stars to values as low as $0.3 \mathrm{ms}^{-1}$ (Cosentino et al. 2012). This incredible precision is allowing very low mass planets to be found. Also, follow up observations of very small planets to measure their masses have been conducted using these two spectrographs. For example, Kepler-78b was found to have a radius of $1.16 \mathrm{R}_{\oplus}$ (Sanchis-Ojeda et al. 2013). Using HARPS-N, Pepe et al. (2013) found the mass of the planet to be $1.86 \mathrm{M}_{\oplus}$. This leads to the conclusion that the planet may have an iron and rock composition due to its mean density being measured as $5.57 \mathrm{g/cm}^{-3}$. This is very similar to the mean density of the Earth ($5.514 \mathrm{g/cm}^{-3}$)[5].

1.2.2 Transits

If the plane of the planet's orbit lies along the observer's line of sight it may be possible to observe the planet passing in front of the disc of its host star. The concept is theoretically simple but detecting this event can be difficult in practice. For example, the dip in brightness from a Sun-like star caused by a Jupiter analogue is approximately 1%. Figure 1.7 is an example of a transit light curve.

[5]http://nssdc.gsfc.nasa.gov/planetary/factsheet/earthfact.html

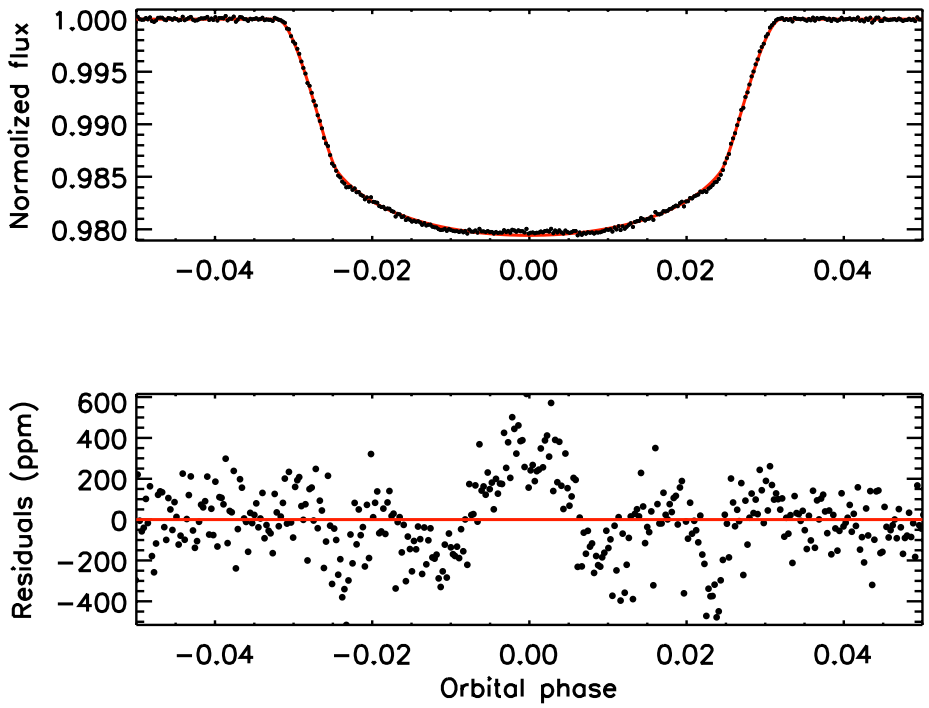

Figure 1.7: Light curve of Kepler-17 ,which hosts a $2.45 M_{Jupiter}$ mass planet in a 1.49 day orbit (Désert et al. 2011). The black points are the data and the red line is the model fit to the data. The bottom panel shows the residuals from the model fit. It can be seen that there is a clear trend in the residuals due to the planet occulting a spot on the photosphere of the host star.

The geometric probability of a planet transiting its host star is given by $R_\star/a$, where $R_\star$ is the radius of the star and a is the semi-major axis of the planet's orbit. This shows that the further out a planet is, the lower the probability of a transit being observable. If, for simplicity, we assume that limb-darkening is negligible, then depth of the eclipse (ΔF) relative to the out-of-transit flux (F) is the ratio of the areas, i.e.,

$$\frac{\Delta F}{F} = \left(\frac{R_P}{R_\star}\right)^2, \tag{1.2}$$

where $R_\star$ is the radius of the star and R_P is the radius of the planet. By analysing transit and radial velocity data in conjunction with some understanding of the mass-

radius relation for stars, it is possible to derive the mass and radius of the planet.

1.2.2.1 Transit Surveys

To estimate (very roughly) how many stars one needs to observe to find a transiting hot Jupiter, let us begin with the following assumptions:

- Let us look only at solar radius (6.955×10^8m) stars.
- A priori the distribution of the inclinations is unknown so assume that the inclination of planets relative to our line-of-sight is randomly distributed.
- Hot Jupiters have similar semi-major axis as 51 Peg b, approximately 0.052au (Mayor & Queloz 1995; Marcy et al. 1997).
- 1 in 100 stars has a hot Jupiter (Wang et al. 2015).

With these assumptions, the probability that a hot Jupiter with a similar orbit to 51 Peg b transits its host star is 0.09%. The size of the sample required to find one hot Jupiter is $\sim$ 11000 stars. This is a very simplistic view but it does illustrate the point that to find just a handful of hot Jupiters a large sample size is required. For this reason transit searches are normally conducted as large scale surveys. Most ground based planet hunting surveys do not target particular stellar spectral types, in general because by observing all visible stars (magnitude limited by the telescope) it increases the potential planet detections. Also, to be sure that the transit signal is not noise, three transits need to be observed. There are many systems that can cause a signal that can mimic a planetary transit e.g. eclipsing binary systems. So these surveys need to have a long baseline of observations to confirm the candidate systems they find and rule out astrophysical mimics. There are advantages to targeting particular stellar types though. For example, the MEarth project (Charbonneau et al. 2009; Berta et al. 2012), is a project looking at 2000 M-dwarfs for planets, specifically Earth-sized planets. When Earth-like planets transit Sun-like stars the lightcurve transit depth is

very small. For an M-dwarf the relative size of the planet to the star is larger and hence the lightcurve transit depth will be larger. This survey has only found one planet, GJ1214b (Charbonneau et al. 2009) but recent work has shown that $\sim 50\%$ of M-dwarfs have an Earth-sized planet in the region where liquid water could exist on the planet's surface (Habitable zone). Surveys also allow for the study of the stars themselves. To fully understand the planets we need to understand the stars which they orbit. Observing the star over a long period of time can help in understanding factors, such as granulation, that can cause systematic effects in observations of transit light curves.

1.2.2.2 WASP, Kepler and CoRoT

The Wide Angle Search for Planets (SuperWASP, Pollacco et al. 2006), is a project to find bright transiting planets. It uses two instruments, SuperWASP-North on the island of La Palma in Spain and WASP-South in Sutherland, South Africa. The instruments use an array of eight, 200mm Canon lenses each attached to a CCD camera with a limiting magnitude of $V \sim 12.5$ (Pollacco et al. 2006). Over each observing season, the cameras image the night sky, excluding the galactic plane due to overcrowding and not above 80°, looking for the signature dips caused by transiting planets. After follow-up spectroscopic and photometric observations of possible candidates to rule out these mimics, WASP is, by number of planets found, the most successful ground based transiting exoplanet survey. Spectroscopic follow-up observations are used to rule out the possibility that the unseen companion is another star and photometric observations taken with CCDs with higher spatial resolution are used to make sure the signal is not from a blended eclipsing binary. Currently 105 planets have been published[6] which is almost twice the number of the next-most successful survey, HATnet (Bakos et al. 2002). The WASP archive contains 2000 nights of data for over 30 million stars (Micela et al. 2014). Characterisation is one of the forefront areas of research for transiting

[6]http://www.astro.keele.ac.uk/jkt/tepcat/html-tepnumber.html

exoplanets, and the hot Jupiters that WASP has found orbit bright stars which has enabled follow up observation to probe their atmospheres to be conducted.

The dip caused by the transit of the Earth is;

$$\left(\frac{\mathrm{R}_\oplus}{\mathrm{R}_\odot}\right)^2 = \left(\frac{6.37 \times 10^6}{6.96 \times 10^8}\right)^2 = 84\text{ppm}$$

From the ground precision at the level of 1000ppm is the norm for telescopes between 1-4m (Jenkins 2002). Recently defocused photometry (Southworth et al. 2009c) has been used to gain very high precision when observing the transits of hot Jupiters, e.g., Tregloan-Reed & Southworth 2013, were able to obtain a precision of $\sim$ 200ppm per data point with an observational cadence of $\sim$ 150 seconds, for the transit of WASP-50. The duration of the transit is another factor that needs to be accounted for because to get the most reliable depth one must observe the full duration of the transit, including pre-ingress and post-egress data. The transit duration is given by equation 1.3 (Seager & Mallén-Ornelas 2003)[7], where P is the period of the planet, $R_\star$ and R_P are the radii of the star and planet and a is the semi-major axis of the planet's orbit.

$$T_{dur} = \frac{P}{\pi} \sin^{-1}\left(\frac{(R_\star + R_P)^2}{a}\right) \tag{1.3}$$

Using equation 1.3 the transit duration for the Earth is about 13 hours. This is too long to be observed in one night, so multiple transit would need to be observed to detect an Earth-like planet and a long baseline of observation would be required to do these observations. These observations are possible with the Kepler space telescope. Kepler is a mission designed to be capable of finding transiting of Earth-like planets (Koch et al. 2010). In contrast to WASP, Kepler is staring at one particular region of the sky looking for transit signals. The field of view of the telescope is 12 degrees in diameter. One of the primary goals for Kepler is to estimate how many Earth-like planets exist

[7]This is assuming the impact parameter of the star is 0, i.e., the planet crosses the equator of the star

in the habitable zone around Sun-like stars. It is possible, in principle, to detect Earth analogues with Kepler because it has the capability of reaching the 20ppm precision level for a timescale of 6.5 hours when observing a G2 star (Batalha et al. 2011). This only accounts for white noise and so the true value is larger depending on the star and the systematic errors present in an individual data set. Combining Kepler photometry with ground spectroscopy Batalha et al. (2011) were able to detect the transit of Kepler 10b. This was Kepler's first rocky planet and has a transit depth of 152 ± 4 ppm with a period of 0.83days. In the first 6 quarters of Kepler data, when analysed by Batalha et al. (2013), there were 202 planet candidates in the range $R_P < 1.25R_\oplus$ (which are classified Earth sized) and 422 in the range $1.25R_\oplus \leq R_P < 2R_\oplus$ (which are classified as Super-Earth-sized). However, the stars in the field of view of the telescope are not very bright. Figure 1.8 (private communication: J. Southworth) compares the brightness of the planet host stars in the Kepler and SuperWASP sample. Figure 1.8 shows that most of the planet host stars are $13 \leq \mathrm{V} \leq 16$ for the Kepler sample. This faintness means these targets are very hard to follow up from the ground.

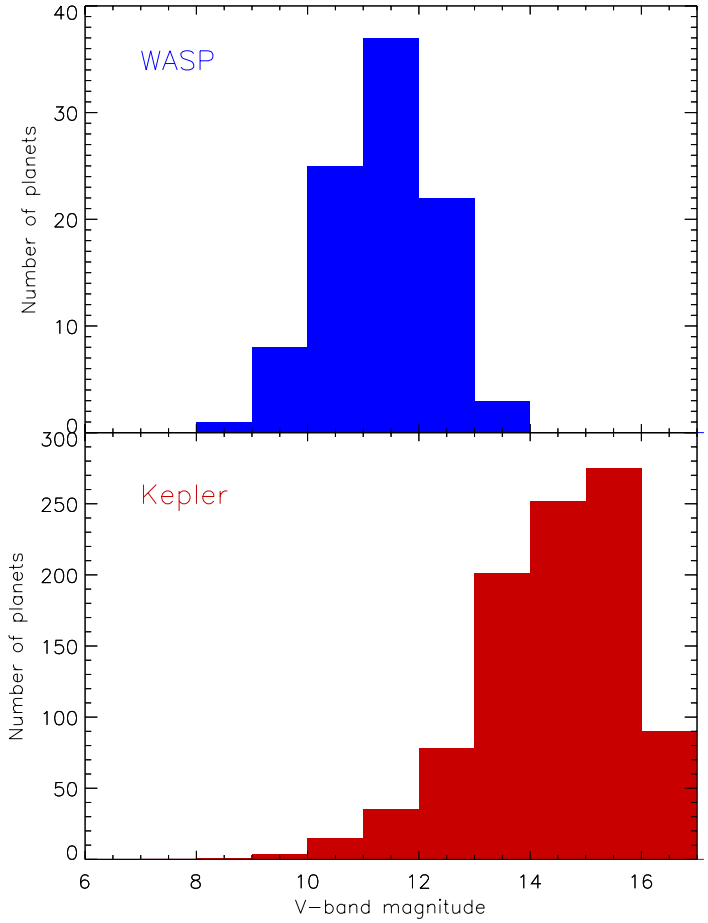

Figure 1.8: Comparison between the V-band magnitude of the planet host stars for the WASP and Kepler samples.

Kepler was able to detect transits of planets in multi-planet systems because it constantly observed the one patch of sky for nearly 4 years. By taking data from the NASA exoplanet archive[8] I generated Figure 1.9.

[8]http://exoplanetarchive.ipac.caltech.edu/

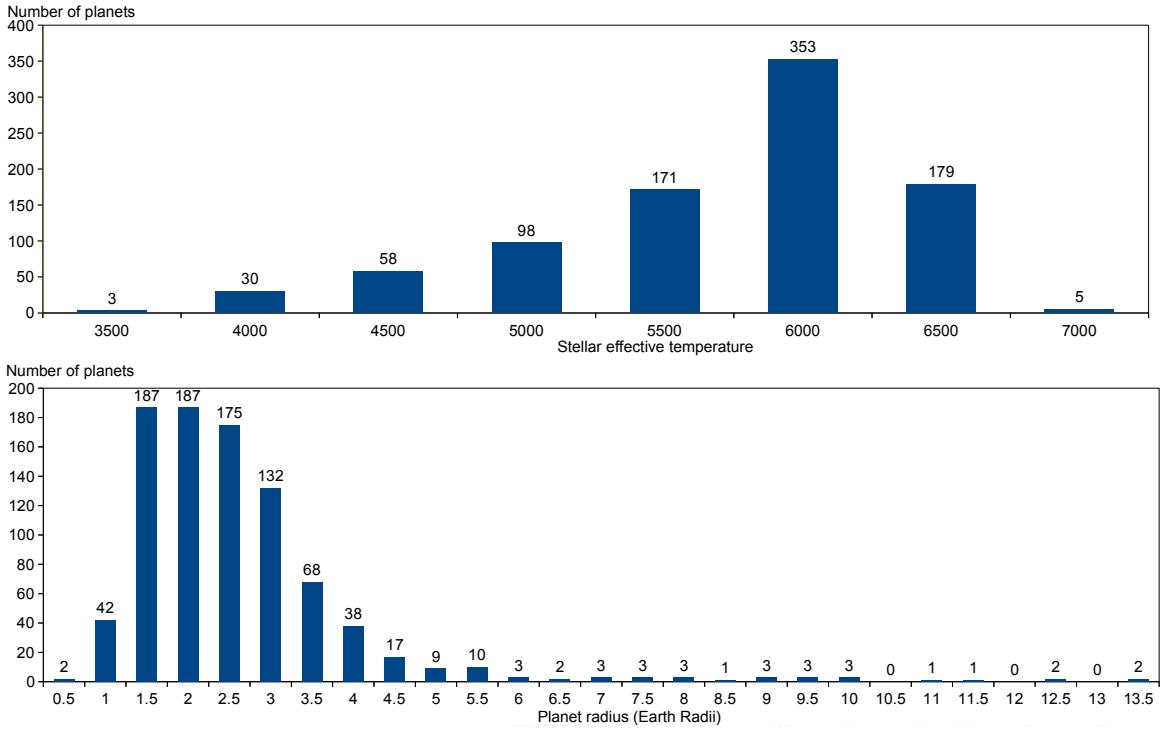

Figure 1.9: (top) Number of planets in multiple systems relative to the effective temperature of the host star. (bottom) Number of planets in multiple systems relative to the radius of the planet.

Figure 1.9 shows the number of planets found in multiple systems by Kepler relative to the stellar effective temperature and the distribution of the planet radii. It can be seen that most of the multi-planet systems that Kepler has found are around stars similar to the Sun ($T_{\rm eff} \approx 5800\,{\rm K}$) and the majority of them have a radius of $1 - 4R_{\oplus}$. The bottom panel in Figure 1.9 shows the lack of Jupiter sized planets ($\sim 11.3R_{\oplus}$) in these multi planet systems. The reason for this is still an ongoing area of research, but the drop off to larger planets is real for the close in orbits that Kepler is sensitive to based the 3.5 years worth of data. The reason for this is that big planets close to their host stars are relatively easy to find, so if they were there they should have been detected by Kepler. For big planets in large orbits the geometric probability

of a transit is very small. Given the short baseline of observations from Kepler the chances of detecting a planet on and Jupiter like orbit, for example, (12 years) is very small.

In multiple planet systems gravitational interactions between the planets can cause variations in the predicted transit times of the transiting planets in the system. Measuring the transit timing variations (TTVs) very precisely can be used to confirm the presence of non-transiting planets in the system and place constraints on their masses (Ford et al. 2011; Nesvorný et al. 2012; Steffen et al. 2012b; Ford et al. 2012b; Fabrycky et al. 2012; Steffen et al. 2012a; Ford et al. 2012a; Ming et al. 2013; Mazeh et al. 2013; Steffen et al. 2013). Kepler-19b (Ballard et al. 2011) is an example of a planet experiencing TTVs with amplitude of $\sim$ 5 minutes. Most hot Jupiters are found in single planet systems (Szabó et al. 2013) and so we would not expect them to show TTVs. However it has been reported that some hot Jupiters do experience TTVs (Ford et al. 2012b). Work conducted by Szabó et al. (2013) showed that some of these TTVs are spurious and have been caused by systematics or induced by stellar rotation/activity. They found three possible candidates which could possibly be due to real TTVs. One of the most exciting possibilities is that these could be induced by moons orbiting the planet (Szabó et al. 2013).

From the transit light curve R_*/a is directly determined, from RV data the eccentricity, e, of the planet's orbit can be determined, and with these two parameters and Kepler's third law the stellar density can be estimated (Maxted, Serenelli & Southworth 2015). With a relationship for the mass and radius of the star as a function of the stellar density, effective temperature and stellar metallicity, the stellar mass and radius can be estimated (Enoch et al. 2010). With an estimate of stellar mass and radius the planetary mass and radius can be estimated. Kepler's photometric precision also allows for the study of the planet host stars through asteroseismology. This technique observes the flux variations of the host star caused by oscillations of the star. Observing these oscillations allows the stellar radius to be determined to $\sim$ 3% (Handler 2013). Hence, the planet radius can be calculated to the same level of precision. This is very important because the dominant source of uncertainty on the planet radius is the stel-

lar radius. Also, even if two planets have very similar masses small differences in their radii can mean they may be very different. Plotting a mass vs radius diagram of some planets along with bulk composition models, Figure 1.10 (Zeng & Sasselov 2013), shows that for a given planetary mass, different planetary bulk compositions give different radii. With an accurate radius measurement this degeneracy can be broken.

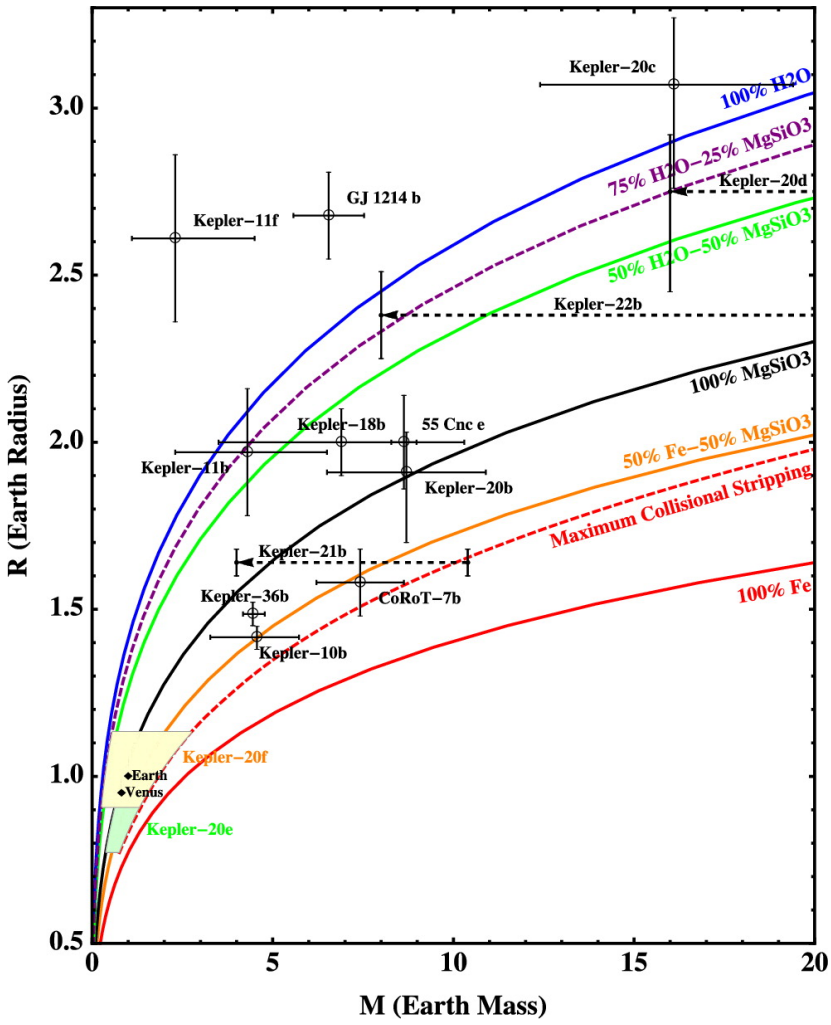

Figure 1.10: Plot from Zeng & Sasselov (2013) showing that planets of the same mass but different composition have different radii. The different coloured lines are for different bulk planet composition.

In the summer of 2013, Kepler's last reaction wheel failed. Without at least 3 reaction wheels the spacecraft is not able to track the stars in its field to the accuracy required to look for transits of Earth like exoplanets. However, there is a wealth of data in the archives which will reveal many more exciting systems. Science observations will still be conducted with Kepler in the K2 mission (Howell et al. 2014). Even though the precision that will be achieved will not be as good as the original Kepler mission, it will still be possible to get down to the 80ppm level over 6 hours for a $V = 12$ star. The mission will observe 8 fields over the ecliptic. This mission will help to build up more statistics of exoplanets in our Galaxy especially of super-Earths about which very little is known.

The Convection, Rotation and planetary Transits (CoRoT) mission, is looking at two regions in the sky which are $2.8^\circ \times 2.8^\circ$[9]. Similar to Kepler, CoRoT is looking for Earth-like planets and looking at the oscillations caused by sound waves in the star (asteroseismology). CoRoT also found the very first rocky exoplanet CoRoT-7b (Leger et al. 2009).

These surveys are just a few of many (HAT, TrES, etc.) that have uncovered fundamental properties of planets in the universe. The exquisite data quality possible due to Kepler being in space (Earth-trailing heliocentric orbit), has lead to the discoveries of Earth-sized (Sanchis-Ojeda et al. 2013) and even sub-Earth-sized planets (Barclay et al. 2013). Follow-up of bright transiting exoplanets, such as those discovered by the WASP project, has allowed the detailed study of hot Jupiters thorough observations of their atmospheres. These planets form in the protoplanetary disc surrounding newly formed stars. Understanding the chemical composition of hot Jupiter atmospheres can, for example, tell us about where in the protoplanetary disc they formed. Understanding formation location in the disc could help in understanding the migration process that has moved them to their current location. The Kepler mission has built up the statistics about the other classes of planets in the universe, such as super-Earths which do not exist in the solar system. It has also shown that multiple planet systems are

[9]http://sci.esa.int/science-e/www/object/index.cfm?fobjectid=31706

very common in the universe. The Kepler mission has also been able to characterise the planet host stars though asteroseismology which is a powerful technique used to determine to very high precision the stellar parameters. This is vital in determining fundamental planet parameters such as mass and radius. For stars with solar-like oscillations it is possible to get the stellar mass and radius to a precision of 3%. This synergy between space and ground based telescopes is set to continue into the coming decades with Next Generation Transit Survey (NGTS, Wheatley et al. 2013) which will find many ice-giant analogues and the James Webb space telescope (JWST, Gardner et al. 2006) which will be able to characterise some of the already found planets and the ones that are just waiting to be discovered.

1.2.2.3 Transit Mimics

One of the major issues that arises in ground based transit surveys is astrophysical mimics of exoplanets. Blended eclipsing binary systems are systems where a close by star and eclipsing binary system are along on the same line-of-sight. This was the case for WASP-9, a planet that was announced by the WASP project that was subsequently found to be a hierarchical triple system (Priv. Com. Andrew Collier Cameron).

Most ground based transit surveys have very large plate scales (the number of arc seconds covered by each pixel). For example, the WASP instruments have a plate scale of 13.7″/pixel (Pollacco et al. 2006). This leads to more than one star being observed in some pixels, particularly when observing regions of high stellar density, e.g., near the galactic plane. In this case transits that occur in a background eclipsing binary system can be diluted (made shallower) by a foreground star. This can mimic an exoplanet transit. Follow-up observations can determine if an exoplanet candidate is in fact a blended eclipsing binary system. This is usually done with a telescope which has a CCD camera with a finer plate scale. An example of a telescope used to conduct these observation is the TRAnsiting Planets and Planetesimals Small Telescope (TRAPPIST), which has a plate scale of 0.6″ (Jehin et al. 2011). With this very fine pixel scale, if the host star has any companion, foreground or background stars that

were not resolved in the initial photometry, they may be seen with this telescope. Photometry is then conducted on the star(s) in the region of the potential host to determine which host a planet (if any) or if there was a diluted eclipsing binary. This would be the case if the separation between the host and companion(s) is too small to be resolved by the initial observations. This method can also be used to determine if a transit candidate is real or noise. Spectroscopic follow up observations can also be conducted to look for blended stars. These observations look for multiple lines in the spectra of the target, which would be indicative of companion or non-associated foreground/background stars.

An eclipsing binary system where only the limbs of both stars transit each other is known as a grazing eclipsing binary system. This produces very shallow eclipses which can mimic exoplanet transits. There will, however, be two transits per obit. If this is the case and if the two stars are of different spectral types (i.e., one cooler than the other), then the transits will be of different depths. This is the tell-tale sign of a grazing eclipsing binary. However, if the two stars are of similar spectral types then the transits will be the same depths. To determine if this is the case for a possible exoplanet system, follow up spectroscopy will show two sets of spectral lines moving in opposite directions, which is indicative of this scenario.

If a binary system contains one solar like star and white dwarf, it can mimic a transiting exoplanet. It is possible to discern this scenario though follow up spectroscopy, again, because the white dwarf ($\sim 0.5\,M_{\odot}$) will induce a large radial velocity shift in the host star. Although the frequency of this kind of system is low, it will be important for large surveys looking for Earth-like planets.

1.2.3 Gravitational Microlensing

General relativity describes how masses warp the fabric of space-time and how light can be bent around objects due to this warping of space-time. Imagine that along the line of sight one is observing there are two galaxies, one in the background further away than a foreground galaxy and that they are aligned exactly. General relativity

predicts that the light from the background galaxy (which is occulted) is bent around the foreground galaxy due to its warping of space-time. The light of the background galaxy is seen as ring around the foreground galaxy and is known as an Einstein ring.

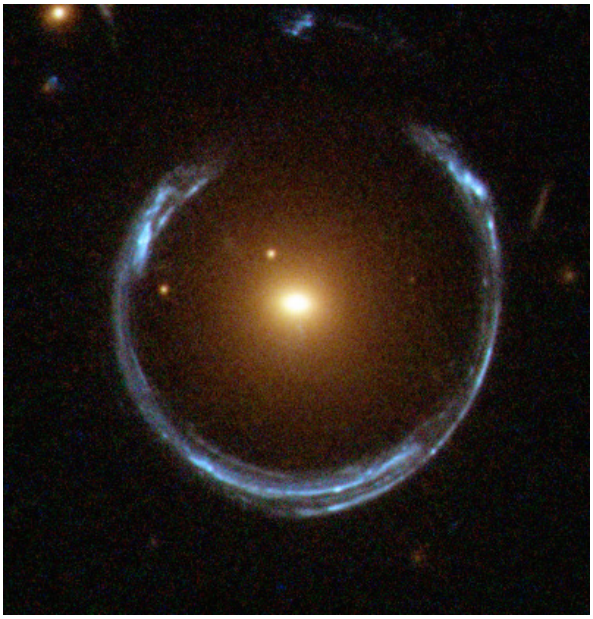

Figure 1.11: An example of a near perfect Einstein ring. In this scenario the background source is distant galaxy and the foreground source is a luminous red galaxy (http://apod.nasa.gov/apod/ap111221.html).

This is known as gravitational lensing (Figure 1.11). In the context of exoplanets both objects are stars and the (unseen) foreground star moves in front of a background star for a period of time. If the foreground star does not host a planet a single brightening (across all wavelengths) of the background star would be observed. If now the foreground star does host a planet, then a double brightening of the background star is observed. The first is caused by the passing foreground star and the second (smaller brightening) caused by the planet. This is called gravitational microlensing, Figure 1.12 (Queloz 2006) shows a schematic of this event and Figure 1.13 (Bennett et al. 2008) shows a real microlensing event.

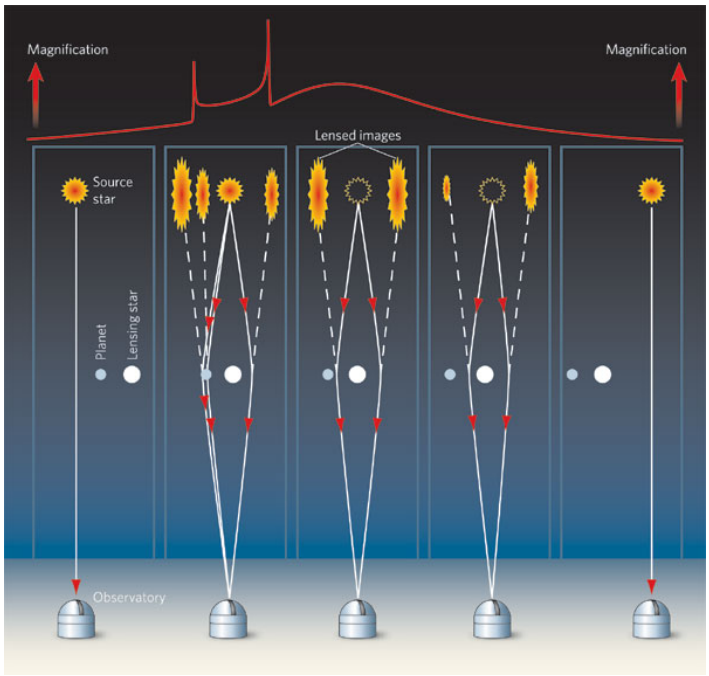

Figure 1.12: Schematic of a gravitational microlensing event where the foreground star hosts a planet.

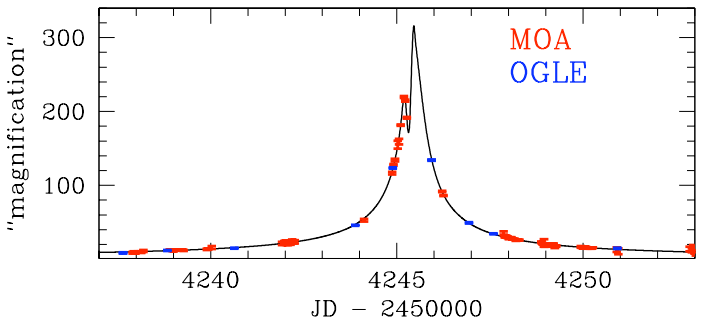

Figure 1.13: Detection of an exoplanet via the gravitational microlensing method. The Planet is MOA-2007-BLG-192Lb. The different coloured points are those obtained by different observations (Bennett et al. 2008). The smaller peak is that due to the passing star's planet and the second is due to the passing star itself.

The major problem with this method is that (unless there is a parallax detected) the data only allows the instantaneous distance of the planet from the star to be derived. It is important to note that this is not the semi-major axis. Another intrinsic problem with this method is that the observation is a one off, i.e., it cannot be repeated. The positive aspect to this method is that it does give statistics on the cold planets. These are hard to find via the transit method because the baseline required to confirm the planet is too long because they are in far out orbits (0.5-10AU Skowron et al. 2014). Also the probability of a transit occurring ($R_\star/a$) is very small for planets that orbit far from their stars. These are also hard to find via the radial velocity method because the radial velocity induced in the star by the planet is very small.

1.2.4 Direct Imaging

When the (flat) wavefronts from a star pass through the Earth's atmosphere they become distorted due to the turbulence. This distortion blurs the point spread function (PSF) of the star and hence the measured full width at half maximum of the PSF would be greater than in the diffraction limit. This makes it impossible to detect faint companions to stars without some form of correction for the atmospheric distortion (seeing). The problem is particularly acute for planets because they are so faint compared to their host star. For example, Jupiter is of order a billionth the brightness of the Sun (Haswell 2010). A technique that has been developed to account for this distortion is adaptive optics. By projecting a laser into the atmosphere, the sodium atoms are excited and fluoresce. This mimics the light of a star passing through the Earth's atmosphere. The telescope then observes this and the adaptive optics measures the wavefronts of the laser. A segmented mirror deforms to the opposite shape of the distorted wavefronts which produces a corrected wavefront and hence a cleaner image. This combined with using a coronagraph can be used to image planets. A coronagraph covers up the majority of the star so that the telescope's detectors are not blinded by the light from the star. Currently this method is sensitive to young planets far from their star. The typical distance at which planets can be detected is $\frac{1}{10}''$ (Guyon et al.

2014). It has been seen from work by (Marois et al. 2008) that planets with a contrast ratio of 10^{-5} (12 mags) relative to their host star are detectable. Giant planets will be very hot immediately after they form but will cool very quickly (Figure 1.14, Brandt et al. 2014). The temperature of the planet at a given age and its cooling rate is dependent on the mass of the planet (Baraffe et al. 2003). The heat is generated through the conversion of gravitational potential energy caused by the accretion of gas from the protoplanetary disk. Coronagraphs have also been used to image planets from space. An example of a planet seen using a space based telescope is Fomalhaut b. Figure 1.15 (Kalas et al. 2008) shows the direct detection of Fomalhaut b through the use of a coronagraph. Two images were taken of the system in 2004 and 2006, during which time the planet is seen to move (bottom right hand box).

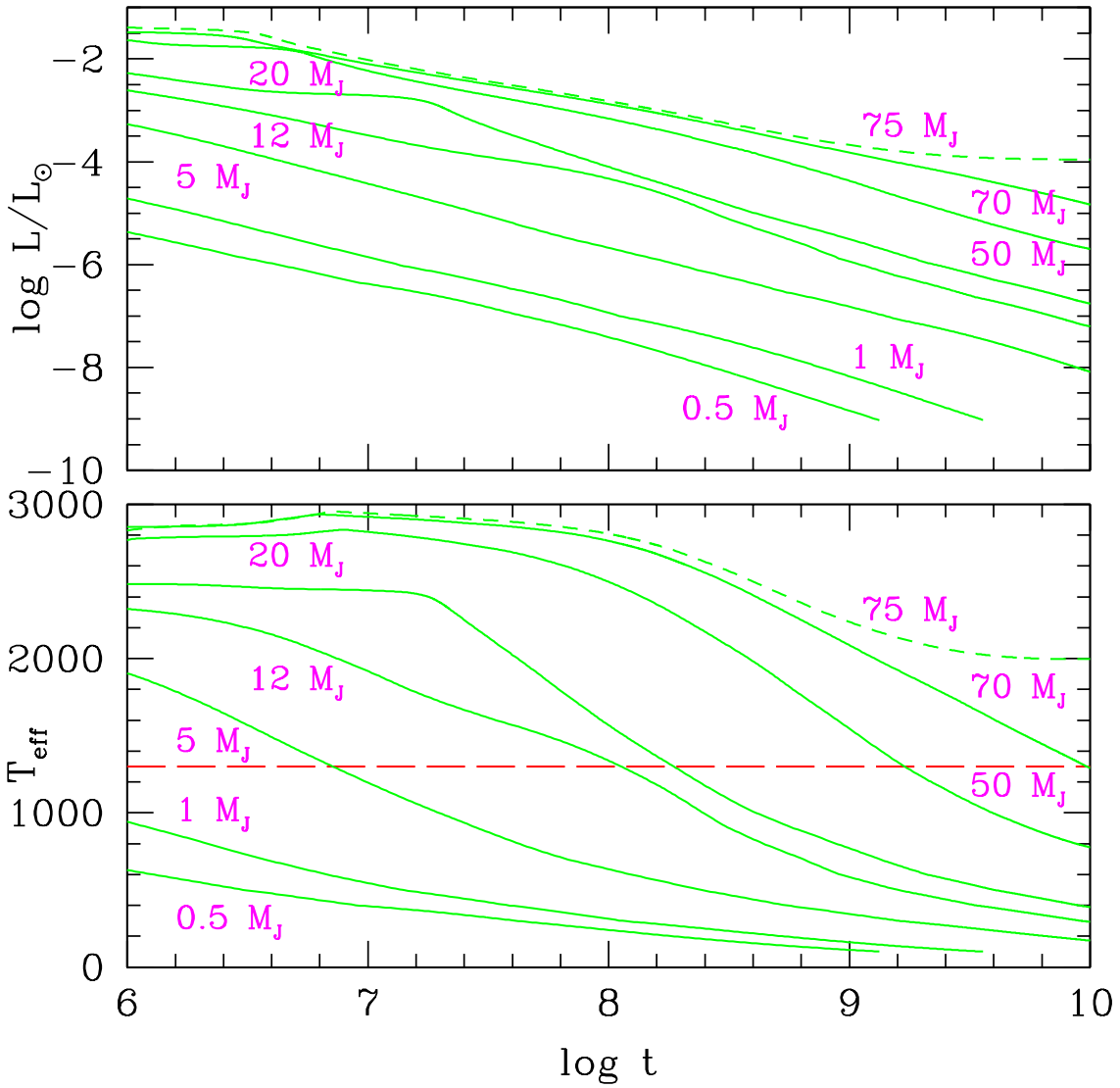

Figure 1.14: The change in luminosity and temperature of planets (solid lines) and brown dwarfs (dashed lines) of given masses with time (in years) (Baraffe et al. 2003). The red dashed line shows the 1300K limit where the model used to determine these cooling rates is valid for extrasolar giant planets. Usually a model that includes dust is generally used for planets with higher temperatures than this limit, however, it has been shown that the dusty model is negligibly different to the model plotted here and hence it is valid to use the non-dusty model shown here for exoplanets that have temperature greater than 1300K (Chabrier et al. 2000)

.

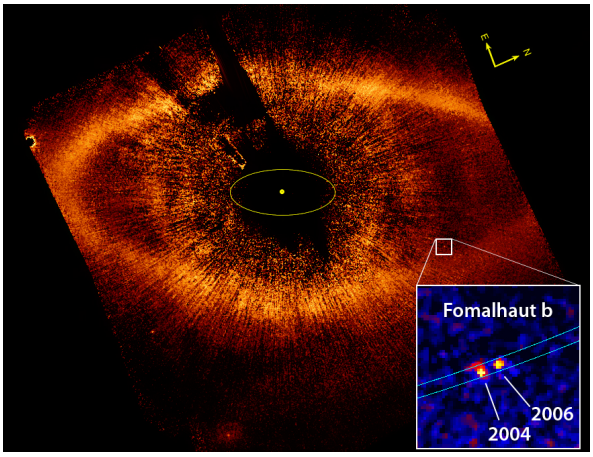

Figure 1.15: Image of the debris disk around Fomalhaut b taken using a coronagraph on the Hubble Space Telescope (Kalas et al. 2008). The box in the bottom right hand corner shows the movement of the planet from images taken in 2004 and 2006. This shows how a coronagraph can be used to find exoplanets.

Instruments that have a coronagraph that can be used simultaneously with a spectrograph will be able to do direct spectroscopy of these exoplanets. In conjunction with adaptive optics this will give very high quality spectra of their atmospheres. With real spectra over the $1 - 10\,\mu$m range much better fits to model SEDs will be possible (as there will be fewer free degrees of freedom).

Current instruments that are in operation looking for planets using direct imaging are the Gemini Planet Imager (GPI) (Graham et al. 2007; Macintosh et al. 2006) and Spectro-Polarmetric High-contrast Exoplanet REsearch (SPHERE) (Beuzit et al. 2008). GPI will use adaptive optics to correct for the distortion of star light caused by the Earth's atmosphere enabling it to produce high-resolution images of planets in orbit around nearby stars. GPI is sensitive to planets more massive than 6 Jupiter masses orbiting 10 or more AU away from their host star at an age of less than 2Gyr (Graham et al. 2007). It is during this time that the planets are bright because they are still hot from formation. GPI is also equipped with an integral field unit, which allows spectra to be taken of objects it is observing and hence it is able to get spectra of exoplanet

atmospheres. An example of a system that has the atmospheres planets analysed using this method is HR 8799 (Ingraham et al. 2014). SPHERE will be used to detect both reflected and thermal radiation of planets orbiting their host stars between 1 and 100 AU (Beuzit et al. 2008). The reflected light can be detected because when star light is reflected off a planets atmosphere it is polarised and the light detected directly from the star is not. The thermal radiation will be detected through IR photometry. Using both these techniques allows both young planets (bright in the IR) and older, cooler planets (visible in polarised light) to be detected.

EPICS: The Exoplanet Imaging Camera and Spectrograph for the European Extremely Large Telescope (E-ELT) will be able to image hot young giant planets and possibly smaller terrestrial worlds in the habitable zone. It will have sensitivity to planets > a few AU from their host star (Kasper et al. 2010). Currently atmospheres of exoplanets can only be studied through transmission spectroscopy and secondary eclipse photometry (see later sections), EPICS will be able to do direct spectroscopy of these bodies which will lead to unprecedented characterisation of their atmospheres. It may even be possible to look for biosignatures in the atmospheres of the terrestrial bodies it could image.

1.3 Bulk densities

Combining RV and transit observations of hot Jupiters allows the system to be characterised in detail. From the transit light curve the parameters that are directly derivable are the transit depth (ΔF), the time in transit ($T_{\text{in trans}}$) (from second to third contact), the transit duration (from first to fourth contact) (T_T) and, if two or more transits are observed, the orbital period (P) (Seager & Mallén-Ornelas 2003). Combining these parameters with Kepler's third law it is possible to derive the planet to star radius ratio ($\frac{R_p}{R_*}$), the impact parameter (b), the scaled semi-major axis ($\frac{a}{R_*}$) and the stellar density (ρ_*). Due to the stellar density being directly derivable the mass-radius relation I use in my analysis is that of Enoch et al. (2010). This method uses the stellar effective

temperature, metallically (derivable from stellar spectral analysis) and density to derive the mass and radius of the star using equations 1.4 and 1.5 ($X = \log(T_{\rm eff}) - 4.1$) from Enoch et al. (2010). The calibration works well for $M_* \geq 0.8\,\mathrm{M}_\odot$ but for lower mass stars there are discrepancies between the predicted and observed stellar radii. This is an ongoing area of research but is thought to be connected with the magnetic fields of these stars.

$$\log M_* = a_1 + a_2 X + a_3 X^2 + a_4 \log\rho_* + a_5 \log\rho_*^2 + a_6 \log\rho_*^3 + a_7 [Fe/H] \tag{1.4}$$

$$\log R_* = b_1 + b_2 X + b_3 \log\rho_* + b_4 [Fe/H] \tag{1.5}$$

	Mass, a_i	Radius, b_i
const	0.458 ± 0.017	0.150 ± 0.002
X	1.430 ± 0.019	0.434 ± 0.005
X^2	0.329 ± 0.128	-
log ρ	-0.042 ± 0.021	-0.381 ± 0.002
log ρ^2	0.067 ± 0.019	-
log ρ^3	0.010 ± 0.004	-
$[Fe/H]$	0.044 ± 0.019	0.012 ± 0.004

Table 1.1: Coefficients for Mass and Radius fits.

The radial velocity data give the minimum mass of the planet $M_p \sin i$ and from the impact parameter the inclination is derivable so it is possible to derive M_*, R_*, M_p and R_p. This allows the derivation of the bulk density of the planet. However as was seen from figure 1.10 planets of the same mass/radius can correspond to different bulk compositions so the bulk density is used more as a guideline and major conclusions should not be drawn from this quantity alone.

1.4 Inflated Radii and Eccentricity

There are many planets whose radii are larger than expected (Figure 1.16), for example WASP-17b, which has a mass and radius of 0.486 M_J and 1.991 R_J, respectively (Anderson et al. 2011b).

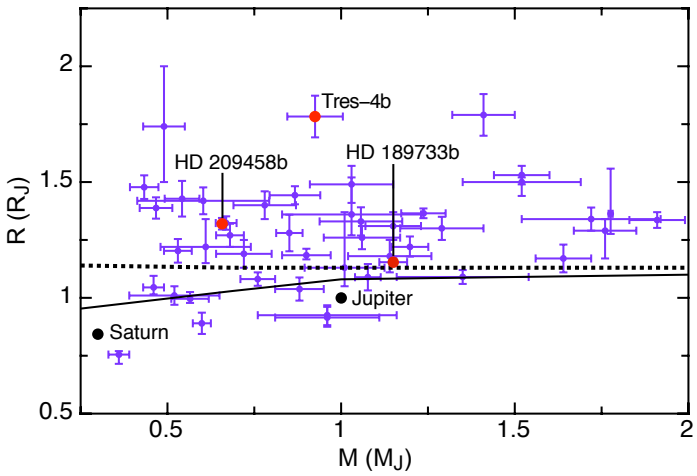

Figure 1.16: Mass-Radius plot showing the Hot Jupiters that require some source of energy to increase their radii. Those planets which lie above the lines require this energy source. The difference between the lines is that one assumes the planet has no core, the dashed line, and the other assumes a 40 Earth mass core, the solid line (Batygin & Stevenson 2010). The red circles are those planets which are investigated by Batygin & Stevenson (2010).

After their formation, gas giants are expected to be very hot ($\sim$ 2000K, see Figure 1.14). As they age they are expected to cool and contract. This means there must be some source of energy that is resisting the contraction for those planets whose radii are found to be larger than expected, or that re-inflates/re-heats the planet after it has cooled. Fortney, Marley & Barnes (2007), presented an investigation where they determine the expected radius of a planet based on the composition of the planet (gas giant, rocky planet, water world or iron planet). Their models for gas giants are based

on the standard cooling theory of irradiated gas giants (Fortney & Hubbard 2003; Fortney 2004). From the models of Fortney, Marley & Barnes (2007), WASP-17b is expected to have a radius of $1.3R_J$, however Anderson et al. (2011b) find the radius to be $1.991 \pm 0.081 \mathrm{R_J}$. One explanation that has been proposed for this is that of tidal heating (Bodenheimer, Laughlin & Lin 2003; Jackson, Greenberg & Barnes 2008a,b; Ibgui & Burrows 2009). This theory says that if a planet is on an eccentric orbit then it will experience a difference in the magnitude of the gravitational pull of its star at different points in its orbit. This causes the interior of the planet to heat up, which act against the contraction. However, standard theories of hot Jupiter exoplanets predict that these planets should be in circular orbits, because if they were to form in eccentric orbits then, due to the proximity of their stars, the time in which their orbits would be circularised (circularisation time scale) is smaller than the predicted age of the systems (Haswell 2010, Smith et al. 2011).

If a planet is in a circular orbit then (if it is a transiting planet) the secondary eclipse should be observed half a phase after transit. If it is in an eccentric orbit then the secondary eclipse will occur either later or earlier than expected. By measuring this timing offset we are able to constrain the eccentricity of the planet. The eccentricity is constrained to (Charbonneau et al. 2005; Machalek et al. 2008),

$$e\cos(\omega) = \frac{\pi \Delta t}{2P} \tag{1.6}$$

where ω is the argument of pericentre (the angle from the ascending node of the planets orbit to the point of closest approach, Figure 1.17), Δt is the difference in time between predicted secondary eclipse time (circular orbit) and the observed secondary eclipse time, P is the period of the planet. For this to be the cause of inflated radii of giant planets there must be something keeping them on eccentric orbits, e.g., a third body in the system. However, the majority of the giant planets that are being found seem to have circular orbits. Figure 1.18[10] shows the distribution of eccentricities of the known

[10]Data from http://exoplanets.org/plots

transiting exoplanets with periods less than 4 days[11].

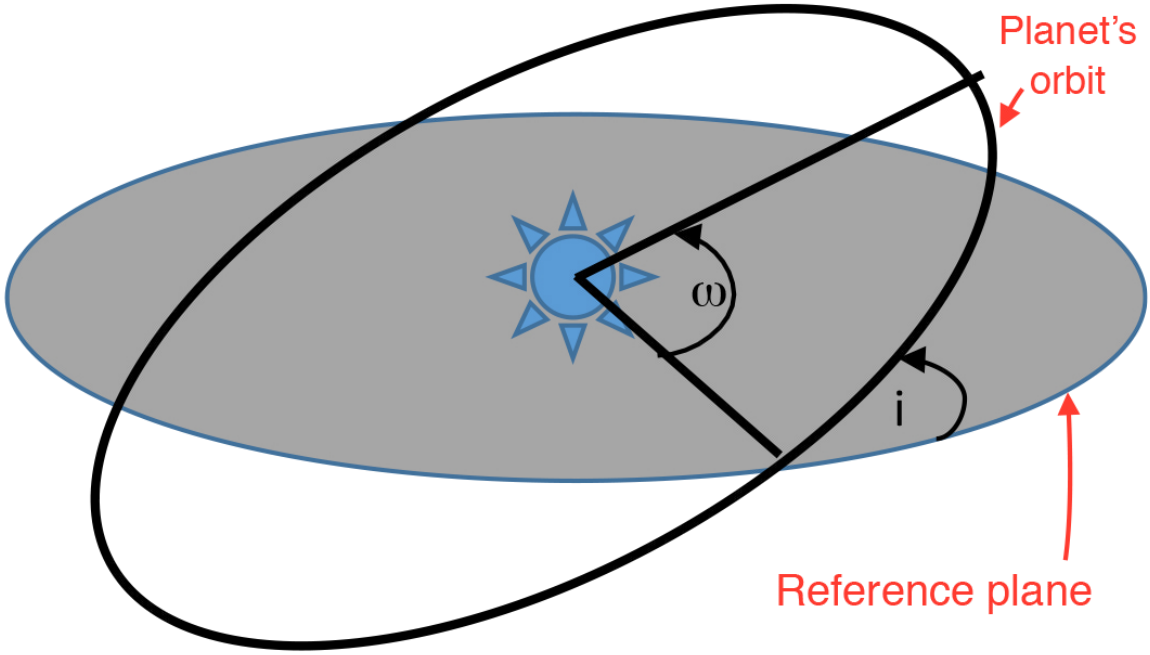

Figure 1.17: Schematic showing the argument of pericentre and inclination of the planets orbit.

[11]For clarity I have excluded the Kepler systems as the majority of them are in circular orbits and hence it is not possible to see clearly the eccentric systems on this plot

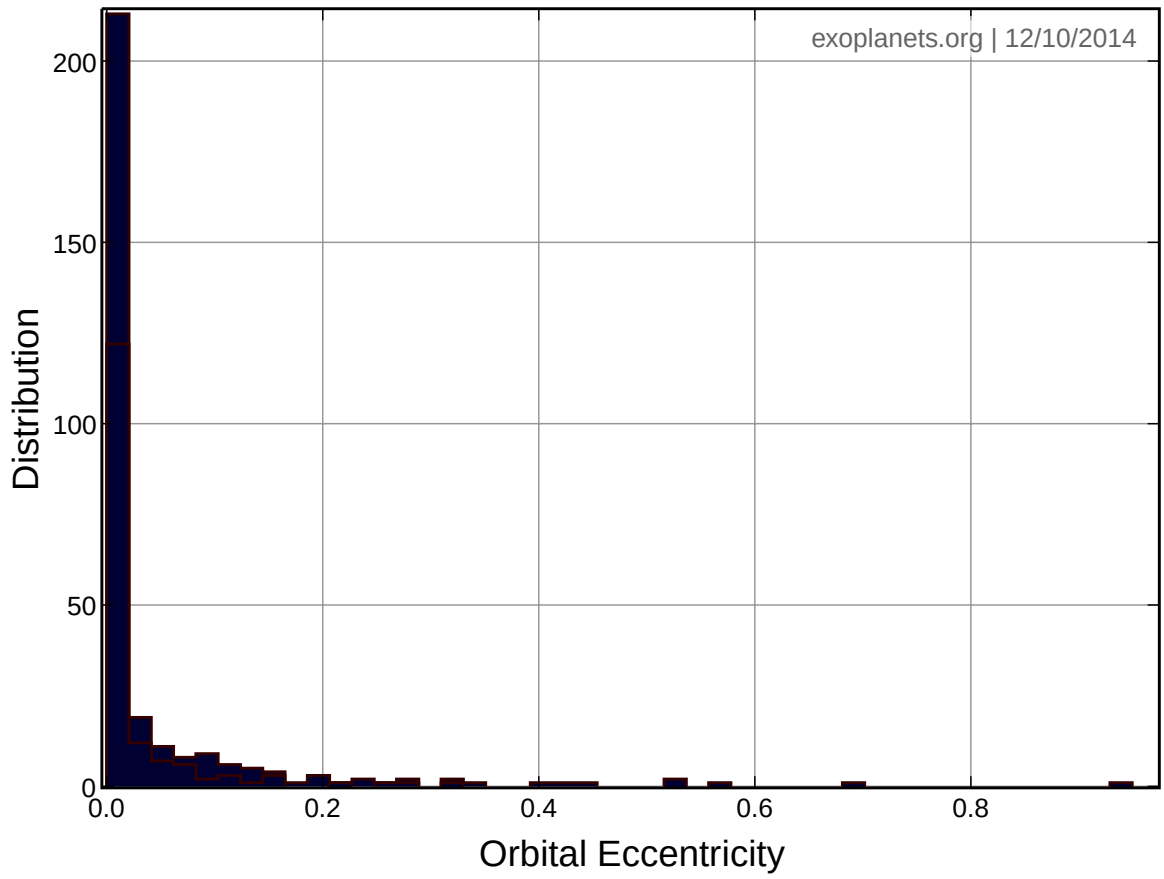

Figure 1.18: Eccentricity distribution for transiting planets (excluding Kepler systems) for planets with period less than 4 days.

Another theory that has been suggested is Ohmic dissipation (Batygin & Stevenson 2010). The irradiation of the planet's atmosphere by the star will induce winds in the atmosphere. If the atmosphere is hot enough then some alkali metals will be partially ionised. The interaction between the ions and the magnetic field of the planet will induce a current into the planet, this current will pump energy into the interior of the planet which will heat up the interior and resist the contraction. Batygin & Stevenson (2010) tested their models on three planets that are found to have inflated radii, HD189733b, HD209458b and Tres-4b. They find that their model can reproduce

the anomalous radii for HD189733b, HD209458b but not for Tres-4b. This is a very new theory and requires further study.

1.5 Atmospheres of Exoplanets: Planet Characterisation

1.5.1 Transmission Spectroscopy

Transmission spectroscopy is a method of looking at the atmospheres of hot Jupiters as they transit their host stars. It involves taking the spectrum of the system before/after and during transit. The out-of-transit spectrum is that of the host star, with a negligible amount of light from the planet. During transit, the light from the star passes through a portion of the atmosphere of the planet. Some of this light is absorbed by gases/hazes in the atmosphere of the planet and re-emitted away from the line of sight. This process superimposes the spectrum of the planetary atmosphere on top of that of the star. By removing the out-of-transit spectrum from the in-transit spectrum, the spectrum of the planet's atmosphere can be extracted. A low-resolution version of the planet's atmospheric transmission spectrum can be obtained using photometry by observing the transit at multiple wavelengths and looking for a change in the transit depth. This corresponds to a change in the ratio of the radii of planet and star. The change in the transit depth is due to gases at different heights of the planetary atmosphere absorbing the light from the star. Madhusudhan et al. (2014) use HD189733 as an example and given the following assumptions

- $T_P = 1100$K,
- $g = 2140\,\mathrm{cm\,s^{-1}}$ (acceleration due to gravity),
- H_2 dominated atmosphere,
- a haze in the atmosphere at 10 scale heights,

the change in the transit depth relative to the transit depth when the haze layer is not probed is calculated using equation 1.7 (assuming hydrostatic equilibrium).

$$\delta_{depth} \simeq \left(\frac{R_p + 10H}{R_*}\right) - \left(\frac{R_p}{R_*}\right), H = \frac{kT}{\mu g} \tag{1.7}$$

In Equation 1.7 H is the scale height of the planet's atmosphere, k is Boltzmann's constant, μ is the mean molecular weight of the atmosphere and g is the acceleration due to gravity. Using Equation 1.7 and the assumptions above, the transit depth would increase by 0.1% compared to 2.5% which is the transit depth when the haze is not probed (Madhusudhan et al. 2014). Transmission spectroscopy for exoplanets was first conducted by Charbonneau et al. (2002). Figure 1.19 shows the transmission spectrum of HD 209458 that was presented by Sing et al. (2008). The Y-axis shows the change in absorption, which corresponds to a change in radius. This shows how small the detected signal is, and hence the difficulty of the technique.

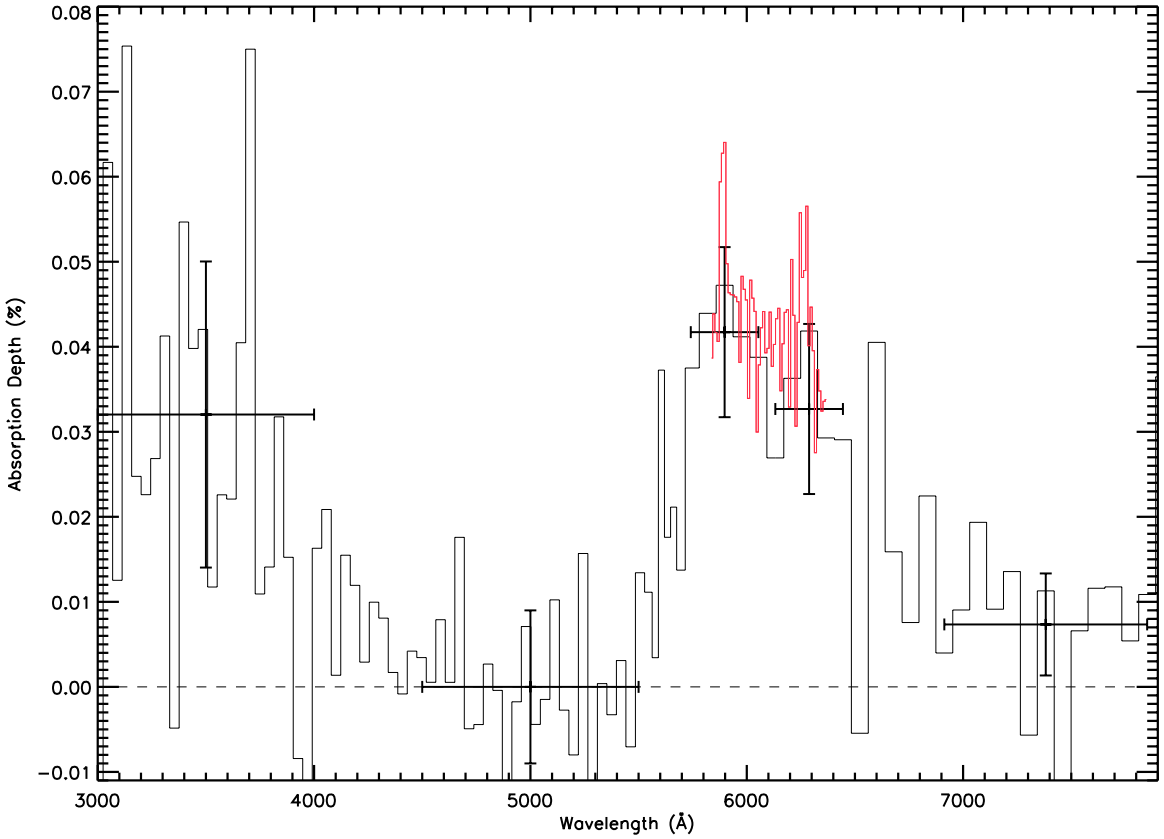

Figure 1.19: Atmospheric transmission spectrum of HD209458 obtained with the STIS instrument on HST (Sing et al. 2008). The Y-axis shows the percentage change in radius relative to the radius measured at 5000Å (to which the spectrum is normalised). The thin red line shows the binned (16 pixels) low resolution spectrum, the grey line represents the binned (18 pixels) medium resolution spectrum. The three features that are found by the investigators are, the Rayleigh scattering shortward 4000Å, the sodium feature shortward of 6000Å and the TiO and VO feature at 6200Å.

1.5.2 Secondary eclipse photometry

In a similar way to observing the dip cause by a transiting planet, there should be a dip in the light caused by the day-side of the planet being occulted by the host star. By observing the secondary eclipse in multiple wavelengths, the emission spectrum of the day side of the planet can be built up (Charbonneau et al. 2005; Deming et al.

2005; Spiegel, Silverio & Burrows 2009; O'Donovan et al. 2010; Todorov et al. 2012; Mahtani et al. 2013). In 2003 NASA launched the Spitzer Space Telescope. It objective was to observe those places in the universe which were hidden from us in optical light (by dust) by observing them in the infrared. Initially there were four channels on the Infrared Array Camera (IRAC) at 3.6, 4.5, 5.8, 8.0μm (channels 1, 2, 3, 4)[12], and three channels on the Multi-band Imaging Photometer (MIPS) at 24, 70 and 160μm[13]. This telescope was not built to observe planets, but then Charbonneau et al. (2005) used Spitzer and (for the very first time) detected the secondary eclipse of an exoplanet. As with transits, during this event there is a loss of light, but instead of a loss of light from the star it is a loss of light from the planet. Figure 1.20 is an example of a secondary eclipse light curve, observed in the four IRAC channels on Spitzer.

[12]http://irsa.ipac.caltech.edu/data/SPITZER/docs/irac/iracinstrumenthandbook/
[13]http://irsa.ipac.caltech.edu/data/SPITZER/docs/mips/mipsinstrumenthandbook

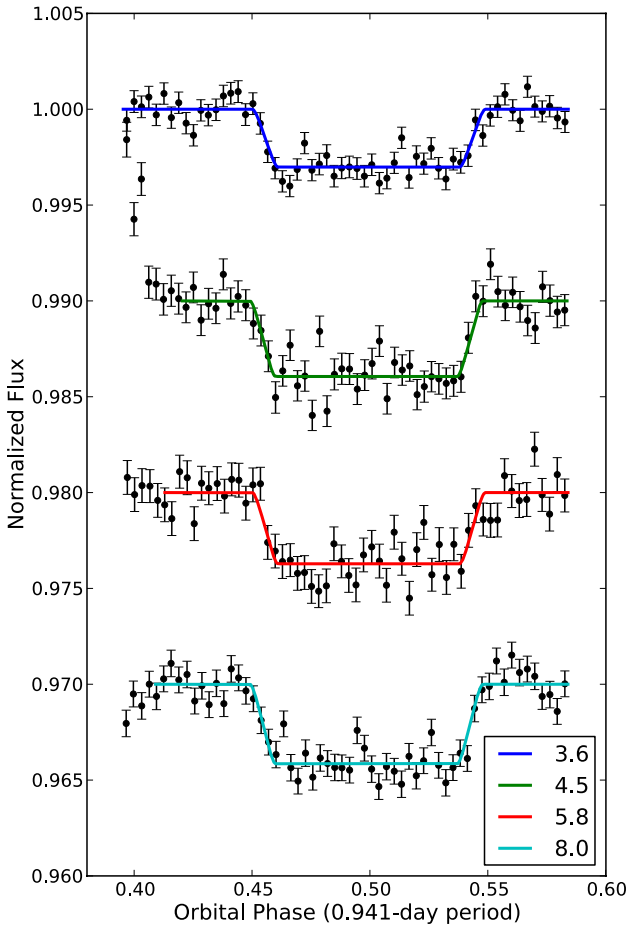

Figure 1.20: An example of the occultation of WASP-18b observed in the four IRAC channels on Spitzer (Nymeyer et al. 2011).

The depth of the secondary eclipse gives the ratio of the day-side flux of the planet to the flux of the star at the wavelength the observation was conducted (Equation 1.8).

$$\frac{F_{\rm day}}{F_\star} = A_{\rm g}\left(\frac{R_{\rm P}}{a}\right)^2 + \frac{B_\lambda(T_{\rm day})}{B_\lambda(T_\star)}\left(\frac{R_{\rm P}}{R_\star}\right)^2$$

In the Rayleigh-Jeans limit

$$\simeq \frac{F_{\rm day}}{F_\star} = A_{\rm g}\left(\frac{R_{\rm P}}{a}\right)^2 + \frac{T_{\rm day}}{T_\star}\left(\frac{R_{\rm P}}{R_\star}\right)^2 \tag{1.8}$$

In Equation 1.8 $F_{\rm day}$ is the flux from the day side of the planet, $F_\star$ is the flux from the star, $\frac{F_{\rm day}}{F_\star}$ is the measured eclipse depth, $A_{\rm g}$ is the geometric albedo, $R_{\rm P}$ and $R_\star$ are the radii of the planet and the star respectively, a is the semi-major axis of the planet's orbit, $B_\lambda(T_{\rm day})$ and $B_\lambda(T_{\rm bright})$ are Planck blackbody functions of the planet and star respectively and $T_{\rm day}$ and $T_\star$ are the brightness temperatures of the dayside of the planet's atmosphere and the star. The whole of the first term on the right hand side of Equation 1.8 is the contribution to the secondary eclipse flux loss from reflected star light off the planet. Cowan, Agol & Charbonneau (2007) and Cowan & Agol (2011) have shown that this term is negligible because the albedos of hot Jupiter exoplanets in the infrared are very low, which means that the amount of light that is reflected by the planet is very small. The second term on the right hand side of equation 1.8 is the contribution to secondary eclipse flux loss from the thermal emission from the planet. Hot Jupiters have atmospheric temperatures of 1000-3000K, which means that (using Wien's law) they have their peak emission at a few microns. The spectral energy distribution of stars like the Sun peak at about $0.5\,\mu$m. Observing secondary eclipses near the peak of the planet's emission will mean the planet will have a favourable contrast ratio to the star. The typical eclipse depth for a hot Jupiter is about 0.01% (Mahtani et al. 2013). Even though Spitzer was not designed to reach this level of accuracy, and despite the fact that it suffers from the IPSVs it is still possible to detect this signal. From the eclipse depth, the temperature of layer of the atmosphere probed can be estimated.

To be able to fully understand these atmospheres more than just Spitzer observations are required. From the ground there are a few infrared windows available that allow secondary eclipses to be observed. These are at $0.9097\,\mu$m (z band) $1.25\,\mu$m (J band), $1.65\,\mu$m (H band) and $2.2\,\mu$m (K band). Many secondary eclipses have been observed at these wavelengths (Föhring et al. 2013; Chen et al. 2014a,b; Zhou et al. 2014) and it has been shown that with the addition of some of these data it is possible to break degeneracies in atmospheric models and hence distinguish between different atmospheric models. For example, in my analysis of WASP-26b, Mahtani et al. (2013), it was possible to see that additional data at J, H and K bands from the ground could

help to determine if the atmosphere of WASP-26b hosted a thermal inversion. However, seeing, thermal emission of the Earth's atmosphere and temperature variations in the surroundings of the telescope mean the precision of measured brightness of the system and hence the eclipse depth will have very large error bars. Hence, the data may not help to break the degeneracies between the models. Instrumental systematic errors can also propagate into the data. Defocusing the telescope spreads out the PSF of the target over many pixels which can reduce pixel sensitivity variations and by using differential photometry sky variations can be reduced. These help but do not alleviate some of the problems but even though the precision is low having some data can still provide a constraint as to which models do not fit the data.

Combining all these data give us the possibility of placing constraints on the chemical composition which in at least one case has allowed the possible detection of a super-solar, C/O ratio[14] (Madhusudhan et al. 2011). A C/O ratio that is less than 0.8 leads to a silicate dominated interior and greater than this value leads to a carbon dominated interior. If this is really the case it would mean that the planet, WASP-12b which they find to have a C/O$>$ 1 has a carbon dominated interior rather than an Earth-like silicate dominated. This conclusion was reached because the atmosphere was found to be two orders of magnitude over abundant in CH_4 and depleted by the same amount in H_2O compared to a solar composition model. This was a very interesting finding because it shows there may be chemical diversity in the composition of exoplanets and also shows why restricting models to solar chemistry may (although a priori not a bad constraint) mean that some atmospheric data cannot be fitted.

1.5.2.1 Modelling exoplanet atmospheres

Much of this subsection is based on the explanations of Madhusudhan et al. (2014). The current state of the field is such that there are two main approaches to the modelling of exoplanet atmospheres. The first approach has been used by Fortney et al. (2006) and

[14]The solar C/O ratio is 0.54

Burrows et al. (2007) and is based on equilibrium constraints. These models begin with the planetary radius, incident stellar radiation at the top of the planet's atmosphere and some abundance for the chemical composition for the planetary atmosphere, e.g., solar composition, and then generate (using stellar models) the stellar spectrum that impacts the top of the planetary atmosphere (Madhusudhan et al. 2014). Further to these the following assumptions are used:

- Radiative-convective equilibrium: The resulting temperature-pressure (T-P) profile of the planet's atmosphere will be consistent with the incident stellar irradiation.
- Chemical equilibrium: This allows the abundances of opacity sources to be calculated.
- hydrostatic equilibrium: This gives the pressure as a function of radius.

The parameter space of T-P profiles can be explored starting with an initial profile. This process results in a T-P profile and the transmission/emission spectrum for the planet's atmosphere. The transmission/emission spectrum is then fitted to the relevant data. This process is repeated until a good fit to the data is found. The goodness of fit statistic that is used for this is usually χ^2.

This, however, is not a good method to be used when modelling hot Jupiters because they experience significant non-equilibrium effects, such as strong recirculation of incident stellar radiation though zonal jets and wind which means that radiative equilibrium does not hold (Madhusudhan et al. 2014). This leads to the second approach developed by Madhusudhan & Seager (2009) and Madhusudhan (2012) in which parametric models are used to determine the thermal structure and spectra of exoplanets, under the same assumptions but without radiative-convective and chemical equilibrium. Instead these models use 10 free parameters to model the T-P profile and the abundances of water, carbon monoxide, methane and carbon dioxide. The parameter space is then explored using a Markov Chain Monte Carlo techniques (see chapter 2)

and the best fitting parameters are found. The atmospheric models that are produced are then fit to the transmission/emission spectrum data.

There are, of course, caveats to this method of atmospheric analysis. The main one being that the models have more degrees of freedom than data points (typically 10 free parameters, Madhusudhan et al. 2014). Typical exoplanet emission spectra (e.g. Mahtani et al. 2013) have only two warm Spitzer points (at 3.6 and 4.5 μm) to fit these models. It is possible to improve the result by observing the secondary eclipse at more wavelengths even just once. Initially it was possible to get data at 0.9097 μm (z band) 1.25 μm (J band), 1.65 μm(H band) and 2.2 μm (K band), Wide Field Camera 3 spectra from Hubble (0.38-0.78 μm) and 4 Spitzer IRAC points (3.6, 4.5, 5.8 and 8 μm) but now the 5.8 and 8 μm are no longer available on Spitzer because those channels required cryogenic cooling which has now been exhausted. Each extra data point (even with large error bars) will give some constraint to the model. Ideally multiple measurements at each possible wavelengths are required because this will allow spurious measurements to be removed and hence not affect the results. Also the results of these parametric models must be checked to ensure that the pressure-temperature profile and the chemical abundances are consistent with each other.

1.5.2.2 Thermal Inversions

Figure 1.21 shows two types of Temperature-Pressure profiles that are used in exoplanet atmosphere analysis. The blue line is a non-thermally inverted atmosphere, where the temperature in the deep interior is constant and hot. In the mid atmosphere there is a temperature gradient caused by the atmosphere radiating away the heat from its interior. The upper most atmosphere the temperature is isothermal. In contrast, if the atmosphere has an opacity source (of unknown composition) in the mid atmosphere ($\sim$ 1 bar) and this source is very efficient at absorbing incident optical and UV radiation then this increases the temperature of that region of the atmosphere and produces a thermal inversion (or stratosphere). This is illustrated as the red line in Figure 1.21. A very interesting finding of the newer secondary eclipses observations for the

understanding of exoplanet atmospheres is that hot Jupiters can be classified into those with and without thermal inversions (Fortney et al. 2008; Spiegel, Silverio & Burrows 2009; O'Donovan et al. 2010; Madhusudhan & Seager 2010; Todorov et al. 2012).

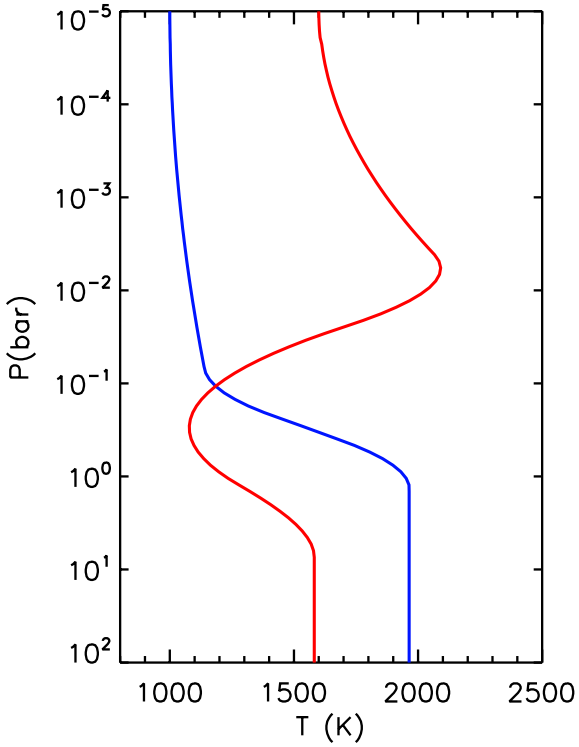

Figure 1.21: This graph illustrated a thermal inversion. The red line (thermally inverted atmosphere) shows that as pressure drops (increasing altitude) the temperature initially stays constant and then decreases (as expected). Then the temperature begins to increase with decreasing pressure (increasing altitude). The blue line shows the expected constant-decrease trend expected with no temperature inversion (Madhusudhan & Seager 2010).

Two possible mechanisms have been proposed to explain whether or not the formation of a thermal inversion will occur. The first uses the magnetic activity of the star as an explanation. The Sun is seen to have a magnetic activity cycle of 11 years. Over this period of time there is a variation in the number of sunspots and other indicators of magnetic activity such as X-ray and radio emission. Of particular relevance to planetary atmospheres is the increase in ultraviolet radiation when the sun is active. A proxy that was used to measure the magnetic activity was the excess in

emission of the Ca II H and K lines from the star. The excess comes from radiation that is emitted from the chromosphere of the star. This was measured by Wilson (1978), in which they measured the amount of excess emission in a 1Å region centred on the Ca II H and K lines. It was seen, over time-scales of the order decades, that some stars emission at these wavelengths varied. These cycles were thought to be analogous to the solar cycle. Those which did not vary were used as standard stars. It became apparent that not all the flux that was being measured originated in the chromosphere. Some leakage of light from the photospheric emission was being detected. So the standard stars were used to measure the photospheric emission and for stars of similar spectral type this photospheric Ca II H and K flux was removed only leaving the chromospheric emission. More work was conducted over the coming years (Noyes et al. 1984; Noyes, Weiss & Vaughan 1984; Baliunas et al. 1995) (for a full review see Hall 2008), during which time much was learned, including a possible relation between the activity cycles and the rotation periods of the stars. In particular Middelkoop (1982); Noyes et al. (1984); Hartmann et al. (1984), showed that the previous way of measuring the activity of the star, S_{HK}[15], needed to be colour corrected. Noyes et al. (1984) describe this correction and called the colour corrected value $\log(R'_{HK})$, where the $'$ shows that the photospheric correction has been accounted for. More recent work has begun to investigate a possible relation between how chromospherically active a star is (proxy for stellar activity) and thermal inversions in the atmospheres of hot Jupiters (Knutson, Howard & Isaacson 2010). In this paper, Knutson, Howard & Isaacson (2010) present the graph in Figure 1.23, which is an empirical relation between stellar activity and thermal inversions. The Y-axis is the measure of chromospheric activity. The X-axis is the difference between, the measured slope between the 3.6μm and 4.5μm eclipse depth points, and the slope measured between these two point from the best fitting blackbody. The blue stars are those stars whose planets are shown not to have thermal inversions and the red circles are those planets that are shown to harbour thermal inversions.

[15]which was a ratio of the measured emission of the Ca II H and K to the flux in 2, 1Å regions either side of the Ca II H and K

The grey square at the top is CoRoT-2b whose spectrum does not fit either of these two classifications. The 4.5μm eclipse depth probes a higher region in the atmosphere than the 3.6μm eclipse depth and so if the brightness temperature of the 4.5μm eclipse depth is higher than that of the 3.6μm then the planet may host a thermal inversion. This is because water and carbon monoxide are opacity sources at 4.5μm and not at 3.6μm (Knutson, Howard & Isaacson 2010). For the planets with thermal inversions the radiation absorbed by these opacity sources causes them to go from absorption to emission. The explanation that is put forward for the divide in Figure 1.23 is that the more active host stars (blue stars in figure 1.23) emit significant UV/X-Ray flux which photodissociates the gas causing the thermal inversion to be present in planets around inactive stars (Knutson, Howard & Isaacson 2010).

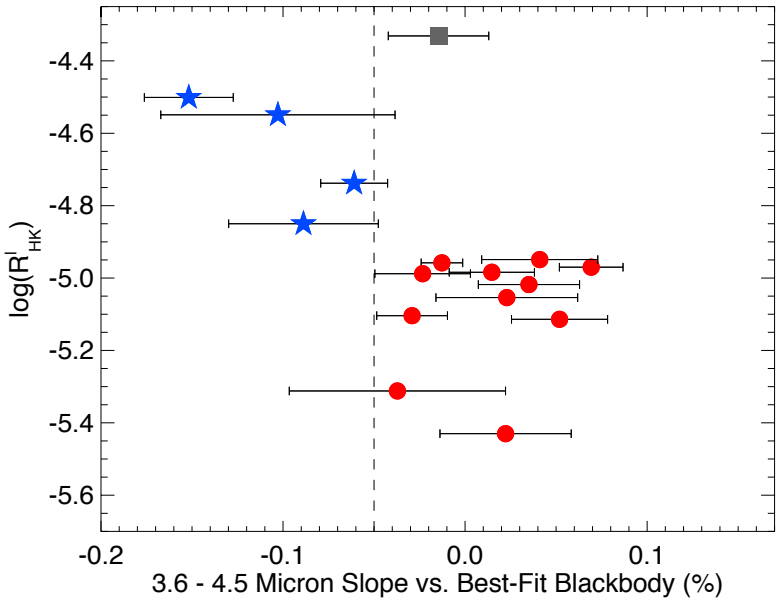

Figure 1.22: The empirical relation between stellar activity and thermal inversions (Knutson, Howard & Isaacson 2010). The blue stars are those planets which do not host thermal inversion and the red circles are those planets which do host thermal inversions.

A second explanation was presented by Fortney et al. (2008) where they suggest that the thermal inversion is dependent on the incident stellar flux, those with (pM class) and without (pL class) thermal inversions. The pM class planets are close enough to their host stars ($\sim 0.04 - 0.05$ AU assuming a solar chemical composition) to have TiO/VO in a gaseous phase in the region of the atmosphere where it can absorb incident stellar radiation. This heats up the gas causing that region of the atmosphere to have a positive temperature gradient with decreasing pressure. Modelling these planets showed that they will have large day-night temperature differences and no shift in the hotspot away from the sub stellar point. The opposite is true for the pL class planets. This has been shown to work for HD209458 and (Knutson et al. 2008) and HD189733 (Fortney & Marley 2007).

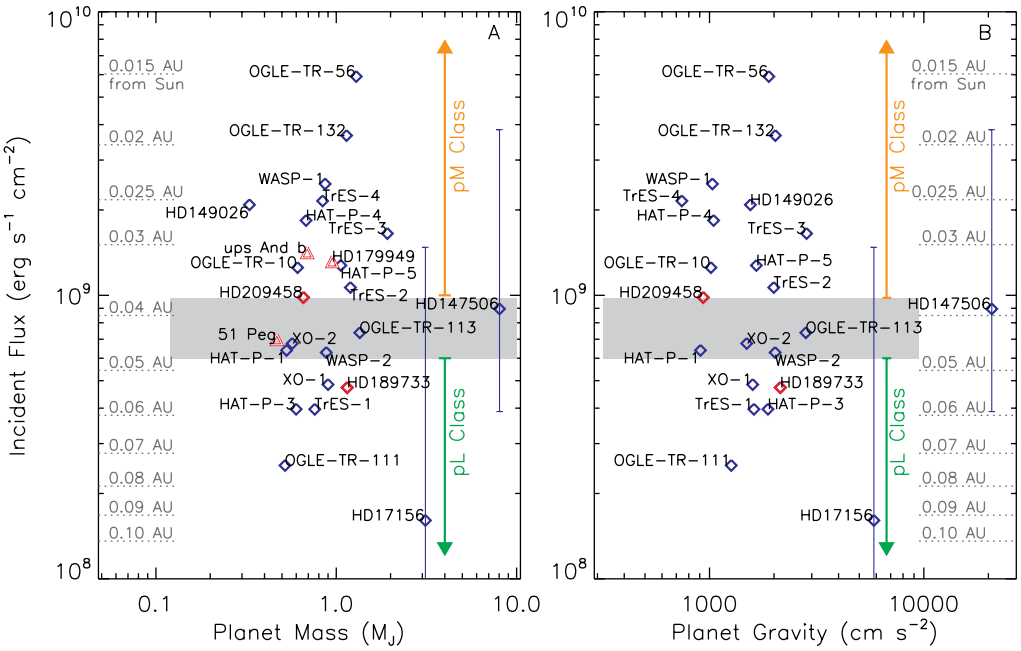

Figure 1.23: Relationship between the presence of a thermal inversion and the incident stellar irradiation from the host star. The left graph shows this as a function of planetary mass and the right graph shows this as a function of planetary gravity

The Earth's atmosphere hosts a temperature inversion (the stratosphere) due to the ozone in the upper atmosphere (O_3) (Chamberlain 1978). It has been found that there is a temperature inversion on Jupiter (the closest analogue we have in our solar system to these giant planets we are investigating) that is formed by methane (CH_4; Madhusudhan & Seager 2010). However, it is not possible for methane to be the cause of the temperature inversion in hot Jupiters because it would be quickly photodisassociated by the high incident UV flux that these planets receive from their host stars. Substantial work has been conducted on the thermal inversions in hot Jupiters (Hubeny, Burrows & Sudarsky 2003; Burrows et al. 2007; Fortney et al. 2008; Spiegel, Silverio & Burrows 2009; Zahnle et al. 2009; Sing & Lopez-Morales 2009; Todorov et al. 2012; O'Donovan et al. 2010; Machalek et al. 2008, 2009; Madhusudhan & Seager 2010). One of the possibilities is that the cause of the observed thermal inversions could be titanium oxide (TiO) and vanadium oxide (VO)(Hubeny, Burrows & Sudarsky 2003; Burrows et al. 2007; Fortney et al. 2008). This possibility was investigated by Spiegel, Silverio & Burrows (2009) and several conclusions were drawn. Firstly, (assuming a solar composition in the atmosphere) the abundance of vanadium oxide is not high enough for the formation of a thermal inversion. Next, given the molecular weight of the two compounds, the heavier a compound is the more likely it is to settle further down (lower altitudes/higher pressures) in the atmospheres of hot Jupiters. This is called gravitational settling. Due to this phenomenon, for TiO/VO to exist in the upper atmosphere of hot Jupiters such that they can absorb incoming radiation there must be mixing on a large scale (macroscopic mixing). This is normally parametrised by the eddy diffusion coefficient (K_{zz}). It was found that the value of this quantity needed to be large, but not unphysical. It should be noted that the eddy diffusion coefficient is a quantity that is added to the model to try and produce observed thermal inversions. Its implications should therefore be treated cautiously. Finally, there could exist a region where the temperature decreases to such a point that these compounds are able to condense out (cold traps). If this were to occur it would mean that the compounds would rain out. Hence it would not be possible to have sufficient quantities of these compounds in the atmosphere to cause a thermal

inversion. To understand where the cold traps exist, the temperature-pressure profile is compared to the condensation curve of the compound in question (figure 1.24). From this, the regions in the atmosphere where a particular compound will be gaseous and where it will condense out can be seen.

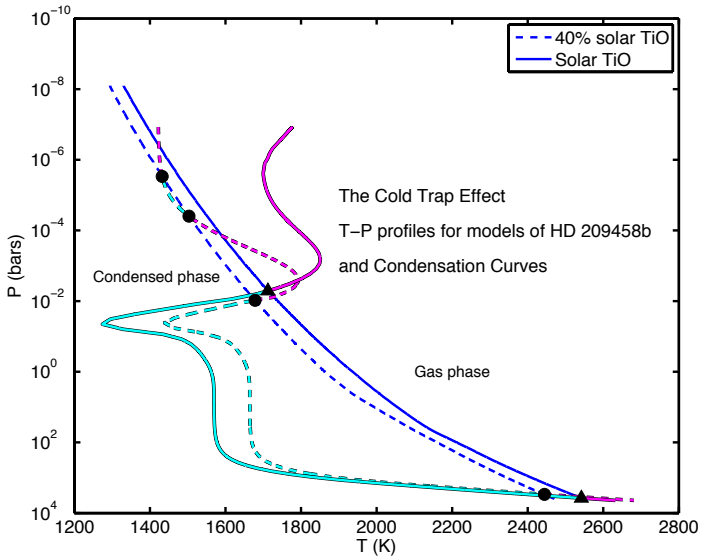

Figure 1.24: Condensation curves for two different abundances of TiO for two different temperature profiles of HD209458. The blue lines are the condensation curve for TiO. The light blue sections of the temperature pressure profiles (i.e. to the left of the condensation curves) are where the temperature is such that TiO condenses out, the purple sections are where the temperature is sufficient for TiO to be in the gaseous phase(Spiegel, Silverio & Burrows 2009).

Another suggestion for the cause of the thermal inversion is sulphur compounds as described by Zahnle et al. (2009). Zahnle et al. (2009) created a model, which was based on the early Earth (Archean period), which was then modified to try and describe the atmospheres of hot Jupiters in the temperature range $1200 \leq T \leq 2000$ K. They find that HS and H_2S can produce thermal inversions in Hot Jupiter atmospheres in this temperature range. This can occur because these two substances efficiently absorb

UV radiation from the host star. It is also suggested that it could be possible to detect the presence of these and other sulphur compounds through radius differences when comparing the transit depths in the UV and optical.

1.5.2.3 Thermal Phase Variations

Due to their proximity to their host stars, hot Jupiters are thought to be tidally locked. This means they have permanent day and night sides. As the planet goes from transit to secondary eclipse, more of the day side is visible to the observer. From secondary eclipse to transit less of the light from the day side is visible to the observer. The functional form of this effect can be approximated using a sine curve. This is known as the thermal phase effect. Thermal phase variations have been observed for several exoplanets (e.g. Cowan et al. 2012; Knutson et al. 2012; Lewis et al. 2013; Quintana et al. 2013; Maxted et al. 2013) and have amplitude of order 1000ppm (e.g. Maxted et al. 2013). Observing thermal phase curves of exoplanets is a good method of probing the day-night side temperature differences and hence heat redistribution efficiencies of the planets. There are two extremes of redistribution, full redistribution and no redistribution. If there is no redistribution from the day-side to the night side then the day side will be permanently hot and the night side permanently cold. Studies have shown that the temperatures of the dayside of hot Jupiters can typically be between 1000 and 3000K. This temperature difference will be seen in the light curve as a sinusoidal variation in light from the system. The amplitude of this variation cannot be greater than the occultation depth. If there is full redistribution from the day side to the night side then the temperature difference will be small. This means there will be very little/no thermal phase variation observable. If a planet is on an eccentric orbit, it will only be in synchronous rotation in the region of periapsis. From these data it is possible to investigate winds on exoplanets by looking for a shift in the hotpot (substellar point). This shift from phase of 0.5 will be seen as an offset in the phase of maximum light from the system. An example is HAT-P-2b (Lewis et al. 2013). In this scenario the thermal phase variations are probing the heating and cooling rates

of the planet's atmosphere. This is very useful because it gives information about the radiative and advective timescales. Another interesting scenario is for the very large giant planets that may be undergoing distortion due to the planet filling its Roche lobe. An example of this class of planet is WASP-12b (Cowan et al. 2012). These planets, as well as showing the thermal phase variations, are also predicted to show ellipsoidal variations due to this distortion. This phenomenon was originally seen in binary systems. As material fills the Roche-lobe, the object becomes tear-drop shaped. This distortion (if the planet is on an edge-on circular orbit as we observe it) means that there will be an excess in light from the system at phases of 0.25 and 0.75 (half way between transit and secondary eclipse). However, the level of this effect is very small, (10^{-4} for WASP-12b for example, Cowan et al. 2012). To detect this level of variation one must fully understand the systematic trends that are present in the data. This is one of the motivations for this work. If it is possible to probe exoplanet atmospheres at this level of detail, a greater understanding of their dynamics and evolution will be gained.

2 Statistical Methods and The Spitzer Space Telescope

2.1 Introduction

The ultimate goal of exoplanet light curve analysis, which is the focus of the work presented in this thesis, is to understand the properties of the planets and their atmospheres. To do this we try to fit theoretical models to the data by determining the values of the parameters that best fit the data. This chapter outlines the statistical methods that are used in this thesis. The second half of this chapter deals with the Spitzer Infrared Space Telescope used to gather most of the data that is presented herein. I will also discuss the (significant) instrumental noise that is seen in Spitzer data of exoplanets. It is this instrumental noise that limits how accurately the parameters can be estimated. Some of these systematics are of known origin and can be compensated for and then removed from the data. Others are of unknown origin and will be the focus of the later chapters. Much of this section is based on notes from the The Imperial Centre for Inference and Cosmology (ICIC) Workshop on data analysis written by Alan Heavens, Andrew Jaffe, Daniel Mortlock and Roberto Trotta[1], and Ford (2005).

2.2 Bayesian Statistics and Markov Chain Monte Carlo

The statistical framework that has been adopted by the exoplanet community is that of Bayesian statistics. If one has some lightcurve data, $\mathbf{d}=[d_i]$, which are taken at some part of an exoplanet's orbit and a model, M that describes the lightcurve, which has parameters $\mathbf{x}=[x_i]$, Bayes' theorem states (Bayes & Price 1763),

[1] http://astro.ic.ac.uk/content/icic-data-analysis-workshop

$$\mathrm{P}(\mathbf{x} \mid \mathbf{d}) = \frac{\mathrm{P}(\mathbf{d} \mid \mathbf{x})\mathrm{P}(\mathbf{x})}{\int_{-\infty}^{\infty} \mathrm{P}(\mathbf{d} \mid \mathbf{x})\mathrm{P}(\mathbf{x})\mathbf{dx}} \tag{2.1}$$

where $P(\mathbf{x} \mid \mathbf{d})$ is called the posterior distribution, $P(\mathbf{d} \mid \mathbf{x})$ is the likelihood, $P(\mathbf{x})$ is the prior and $\int_{-\infty}^{\infty} P(\mathbf{d} \mid \mathbf{x})\mathbf{P}(\mathbf{x})\mathbf{dx}$ is the evidence. The prior allows one to put a constraint on the parameters based on any previous work or analysis. For example, with my analysis of WASP-26 (Mahtani et al. 2013), from work done by Smalley et al. (2010), I was able to use their values of the temperature and metallicity of the host star as a prior in the analysis as well as using the transit lightcurves of their analysis for orbital parameter constraints. In the software that I use for my analysis the prior is constructed in the following way, a Gaussian distribution is created with mean as the value of the parameter and standard deviation the error on the value from which trial values for the parameters are chosen. This allows the software to be more targeted in its exploration of the parameter space and hence converges faster. Another way to construct a prior is to give all possible values equal probability within certain limits. This is called a uniform prior. The denominator of Equation 2.1 is just a normalising constant in this work so can be ignored because one is integrating over all possible values of each parameter. However, this value is very important for model comparison. What is required is to explore the parameter space for each of the parameters. However for exoplanet lightcurve models there may be a large number of parameters. This would be computationally inefficient to do using methods such as grid based methods which evaluates the model at each point of the grid for each parameter. What is required is to maximise the likelihood function and to find the confidence interval on the parameters. To measure the goodness of fit of the model to the data we can use the χ^2 statistic which is defined as (Wall & Jenkins 2003),

$$\chi^2 = \sum_{i=1}^{k} \frac{(O_i - E_i)^2}{\sigma_i^2} \tag{2.2}$$

where O_i is the value of the i^{th} data point, E_i is the predicted value of the i^{th} data point from the model, σ_i is the standard error on the i^{th} data point and k is the number of data points. The lower the value of χ^2 the better fit to the data. A good fit to the

data is one whose χ^2 is approximately the same as the number of degrees of freedom ($\mathrm{N_{df}}$), which is $k - \mathrm{N_{par}}$, where $\mathrm{N_{par}}$ is the number of free parameters. For this reason, one may find it easier to find a good fit to the data by looking at reduced χ^2 which is $\frac{\chi^2}{\mathrm{N_{df}}}$. From this, a good fit to the data is a reduced χ^2 of about 1. If reduced χ^2 is less than 1 then the model being used is overcomplicated and one is over-fitting the data (or the error bars are over estimated).

Using the above theory it is possible to explore the parameter space for a given model using a procedure called Markov Chain Monte Carlo (MCMC). The Markov Chain is a series of N values, where the i^{th} value only depends on the $(i-1)^{\mathrm{th}}$ value. If the error bars on the data collected are (close to) Gaussian and the prior has a uniform distribution then the following relation holds (equation 9 from Ford 2005),

$$\mathrm{P}(\mathbf{x} \mid \mathbf{d}) = \mathrm{P}(\mathbf{d} \mid \mathbf{x})\mathrm{P}(\mathbf{x}) \sim \exp\left(\frac{-\chi^{\mathbf{2}}(\mathbf{x})}{2}\right). \tag{2.3}$$

With this and a set of values of x_i the posterior probability distribution can now be calculated. The algorithm that will be used herein to generate the set of values of x_i will be the Metropolis-Hastings algorithm. One of the main issues with the Metropolis-Hastings algorithm is how to jump from one set of x_i values to the next i.e. what is the probability of the new set of parameters given the old set of parameters, $P(\mathbf{x_{new}} \mid \mathbf{x_{old}})$. This can be split into a product of 2 functions (equation 10 of Ford 2005),

$$P(\mathbf{x_{new}} \mid \mathbf{x_{old}}) = \mathrm{q}(\mathbf{x_{new}} \mid \mathbf{x_{old}})\alpha(\mathbf{x_{new}} \mid \mathbf{x_{old}}) \tag{2.4}$$

$\mathrm{q}(\mathbf{x_{new}} \mid \mathbf{x_{old}})$ is known as the candidate transition probability function and $\alpha(\mathbf{x_{new}} \mid \mathbf{x_{old}})$ is the acceptance probability. The candidate transition probability function is the probability of randomly choosing $\mathbf{x_{new}}$ given that the current point of the chain is $\mathbf{x_{old}}$. q is chosen to be a Gaussian with mean 0 and standard deviation 1. At each step the old parameter value is use to calculate the the trial parameter using:

$$X_i = X_{(i-1)} + \sigma_X * q * f$$

where σ_x is the standard deviation of the parameter from the chain so far and f is the

step size controller. The value of f is adjusted every 100 steps so that the acceptance rate is close to the optimal value of 0.25 (Tegmark et al. 2004). The value of 0.25 is such that the parameter space is explored thoroughly and the region around the best fitting value is explored such that any structure is mapped. In practice this acceptance rate is usually lower due to correlations between parameters.

The acceptance probability $\alpha(\mathbf{x_{new}} \mid \mathbf{x_{old}})$ is the probability of accepting the new point given the probability of the current point. $\alpha(\mathbf{x_{new}} \mid \mathbf{x_{old}})$ is calculated in the following way (equation 11 of Ford 2005),

$$\alpha(\mathbf{x_{new}} \mid \mathbf{x_{old}}) = \min\left[\frac{\exp\left(\frac{-\chi^2(\mathbf{x_{new}})}{2}\right)}{\exp\left(\frac{-\chi^2(\mathbf{x_{old}})}{2}\right)} \times \frac{\mathrm{q}(\mathbf{x_{old}} \mid \mathbf{x_{new}})}{\mathrm{q}(\mathbf{x_{new}} \mid \mathbf{x_{old}})}, 1\right] \tag{2.5}$$

The issue that comes with inaccurate choices of q is that the MCMC will take a large number of iterations to converge. In an ideal world we would choose q to be the probability of the the new $\mathbf{x}$ value given the data ($\mathrm{P}(\mathbf{x}, \mathbf{d})$). However, this defeats the point of the MCMC as this is the distribution that is being evaluated. In practice, the q is chosen to be a Gaussian distribution with mean of $\mathbf{x_{old}}$. This choice of q simplifies the calculation of α to (equation 13 of Ford 2005),

$$\alpha(\mathbf{x_{new}} \mid \mathbf{x_{old}}) = \min\left[\frac{\exp\left(\frac{-\chi^2(\mathbf{x_{new}})}{2}\right)}{\exp\left(\frac{-\chi^2(\mathbf{x_{old}})}{2}\right)}, 1\right] = \min\left[\exp\left(\frac{\chi^2(\mathbf{x_{old}}) - \chi^{\mathbf{2}}(\mathbf{x_{new}})}{2}\right), 1\right] \tag{2.6}$$

With the above in mind, the Metropolis-Hastings algorithm is as follows,

1. Choose the initial values of the parameters.

2. Choose new parameter values using a candidate transition probability function.

3. Calculate the acceptance probability function given by equation 2.6.

4. Choose a random number, between 0 and 1, from a uniform distribution.

5. If the random number is greater than the acceptance probability then the new value is not accepted. If the random number is less than the acceptance probability then the new point is accepted.

6. If the new set of parameters chosen give a better (lower) χ^2 then these are accepted.

7. If the new set of parameters are not accepted then the old set are used as the new step i.e. $x_i = x_{i-1}$.

8. Repeat until number of desired iterations complete.

2.2.1 MCMC Discussion

MCMC can be used to find the minimum χ^2, i.e. finding the parameters of the model that best fit the data using the M-H algorithm. There are other algorithms that can be used to conduct this minimisation, for example the Levenberg-Marquardt algorithm, but these are prone to only finding local minima, although this not necessarily the most efficient way to find the best solution. The Metropolis-Hastings algorithm has the ability to escape local minima as it is possible to accept some points which have worse fits to the data and to give a very thorough exploration of the parameter space. Another advantage is that MCMC works much better than other methods for models that have large numbers of parameters, like those needed to fit models of exoplanet lights curves (Ford 2005). It is also possible to find correlations between parameters easily by plotting the chain iterations of two parameters against each other. If there is no correlation then a plot scaled to the standard-deviations of the two parameters will look like a circular cloud of points. If, however, there is a linear correlation between parameters then the cloud of points will be a tilted ellipse. If this were the case then one could still use the L-M algorithm. However, if one had more severe correlations like those in Triaud et al. (2010) (Figure 2.1) then a more advanced algorithm, such as M-H is required. This example of severe correlation is that of the rotational velocity

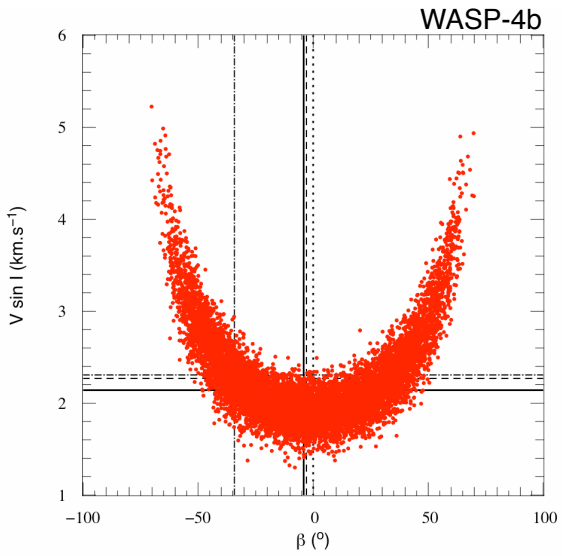

Figure 2.1: Another example of severe correlations that can result from fitting exoplanet data. This result comes from Triaud et al. (2010) and shows the correlation of the rotational velocity of the host star and the spin orbit angle of WASP-4.

(V sin(i)) of the host star with the angle between the normal to the orbit and the rotational axis of the star (spin-orbit angle, β).

There are however disadvantages of MCMC, the main one of which is the large number of iterations required to explore the parameter space. This only makes MCMC suitable for problems where the evaluation of a single model takes little time. If one requires a 3σ limit on certain parameters (for example eccentricity), to have enough points in the wings of the posterior distribution may take longer than is computationally efficient. However, with a good amount of prior information and good algorithm it is possible to calculate these values. For example, in my analysis of WASP-26b, I was able to calculate a 3σ limit on eccentricity with the MCMC method and the M-H algorithm (Mahtani et al. 2013).

When one has run an MCMC analysis, the results are not a single number, they are distributions. In a Bayesian framework, there is no formal definition for how to

choose the best fit parameters. By judicious choices of model parameters one can have nearly Gaussian posteriors. Then the method of parameter estimation used most commonly in the exoplanet field is to take the median value of the distribution as the parameter values and to then choose the error bar to be the region of the distribution that encompasses 68.3% of the probability distribution. This corresponds 1σ in classical statistics.

Another issue that arises with MCMC is model selection because the evidence integral may take a long time depending on the model. The way that this is overcome is through the use of the Bayesian Information Criterion (BIC, equation 2.7) (Schwarz 1978),

$$\mathrm{BIC} = \chi^2 + N_{\mathrm{par}} \ln(N) \tag{2.7}$$

where χ^2 is the goodness of fit for the best fit model parameters, N_{par} is the number of free parameters in the model and N is the number of data points that are being fitted. By running the same MCMC with different models this heuristic can be used to find the best model to use by looking for the lowest BIC value. In reality though, there will come a point where the difference between BIC values is negligible. At this point one would choose the model prior to where the change in BIC is less than $N_{\mathrm{par}} \ln(N)$ as the model to use. However, a word of caution, one must always check that the variation in parameters between models is not large i.e. less than $\sim 1\sigma$. If this not the case then it may not be possible to identify the most likely model on purely statistical grounds.

2.3 The Spitzer Space Telescope

2.3.1 Design and IRAC Instrument

The Spitzer Space Telescope was launched 25 August 2005. The spacecraft, which operates in the infrared, is in a Earth trailing, solar orbit primarily so that the telescope is moving away from the Earth. This allows the solar panels to be permanently pointed

at the Sun, which means the body of the telescope is always facing away from the Sun, avoiding any unwanted infrared radiation to be incident on the telescope (Werner et al. 2004).

Figure 2.2 shows the cross section of the telescope. The Infrared Array Camera (IRAC) (Fazio et al. 2004), is an imaging instrument which had four channels, 3.6 μm, 4.5 μm, 5.8 μm and 8 μm. The 5.8 μm and 8 μm channels, which required cryogenic cooling, were operational for the first part of the mission. However, the liquid helium which was used as coolant has now run out. The only remaining working channels on the detector are the 3.6 μm and 4.5 μm. The field of view of these detectors is $5.2' \times 5.2'$, and the detectors are of size 256×256 pixels. The 3.6 μm and 4.5 μm are Indium-Antimony (InSb) detectors and the 5.8 μm and 8 μm are Silicon-Arsenic (SiSb) detectors. At 5.8 μm and 8 μm *Spitzer* data exhibits ramps at the beginning of the data sets. The 5.8 μm ramp is normally delt with by simply removing the first 30 minutes of data and the 8 μm ramp is accounted for by a polynomial time function (Anderson et al. 2011b). This has been attributed to charge traps in the detectors (Agol et al. 2010).

2.3.2 Systematics of the IRAC detectors at 3.6 μm and 4.5 μm

The IRAC detectors suffer from intrapixel sensitivity variations (IPSVs, Charbonneau et al. 2008; Knutson et al. 2008). This means that different parts of the same pixel can be more or less sensitive than others. This results in the same amount of flux incident on a pixel being measured differently by different parts of the pixel. This would not be an issue if the PSF was stable on the detector. However, there is a battery heater which is periodically turned off and on, which causes periodic fluctuations in the count rate from the star. Initially this was done about every 60 minutes but in 2010 (Memo 2010) the heater cycling was halved so the period of the flux variations is now about 38 minutes. The frequency of the battery heater was doubled so that the amplitude of the variations it caused were halved. The PSF movement within the pixel is $\sim 0.05 - 0.1$ pixels in both the x and y directions which results in periodic flux variations of about

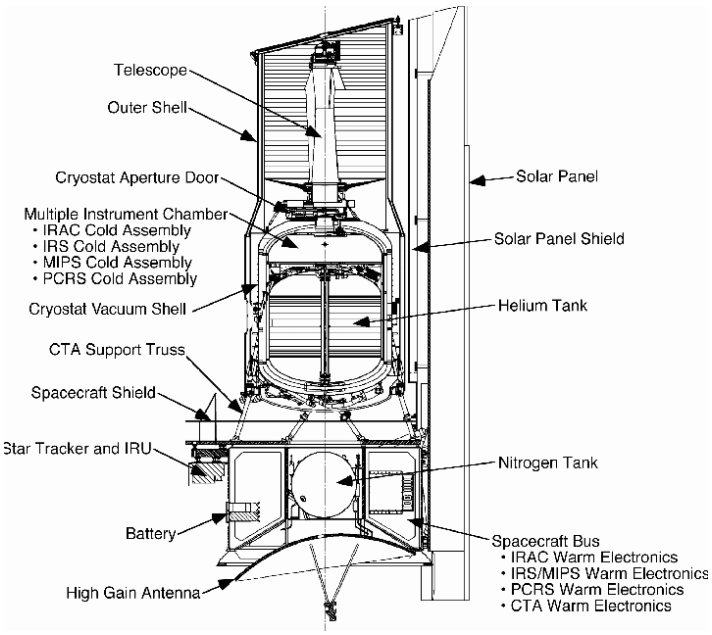

Figure 2.2: A cross section of the Spitzer Space Telescope (Werner et al. 2004)

1% (Cowan et al. 2012). For longer observations (such as thermal phase curves) there is also a long term trend, which is most severe in the y direction. This is typically ~ 0.5 pixels on the time scale of ~ 24 hours (Cowan et al. 2012). Figure 2.3 (Mahtani et al. 2013) shows an example of a secondary eclipse observed using Spitzer IRAC at $3.6\,\mu$m and $4.5\,\mu$m. The saw-tooth shaped trend clearly seen in the $3.6\,\mu$m data and to a lesser extent in the $4.5\,\mu$m data is the IPSVs. The final column is the lightcurve with these trends removed. The secondary eclipse can be clearly seen in both channels.

2.3.3 Accounting for Spitzer Systematics

2.3.3.1 Polynomial Fitting

It is possible to explain the saw-tooth pattern of the raw light curve as the motion of the PSF on the detectors. This means that we can model the change in flux as a

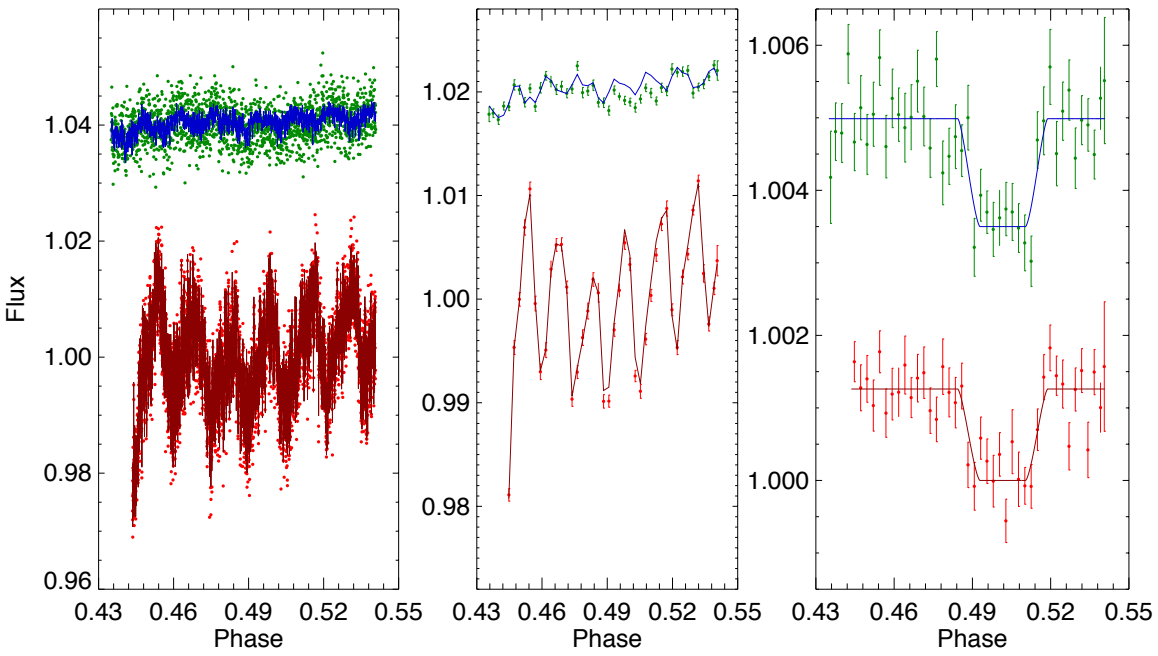

Figure 2.3: Raw and detrended secondary eclipse lightcurve of WASP-26b reported by Mahtani et al. (2013). The lower red points are the 3.6 μm data and the upper green points are the 4.5 μm data. The blue and red lines are the fit to the trends in the data. (Left): The raw light curves with the trend functions. (Middle) Binned light curves with trend models. (Right) The binned light curve with trend function removed and best fitting eclipse models (solid lines). The secondary eclipse can clearly be seen in both channels.

polynomial in the position on the detector. It is sometimes necessary to also include a linear function of time in the correction to the apparent flux, e.g., to account for intrinsic variations in the brightness of the host star. The general functional form is shown in equation 2.8.

$$\begin{aligned}\Delta f = \quad & a_0 + a_x\Delta x + a_y\Delta y + a_{xy}\Delta x\Delta y + a_{xx}\Delta x^2 \\ & + a_{yy}\Delta y^2 + a_t\Delta t,\end{aligned} \tag{2.8}$$

where $\Delta f = f - \hat{f}$ is the stellar flux relative to its weighted mean, $\Delta x = x - \hat{x}$ and $\Delta y = y - \hat{y}$ are the coordinates of the point spread function of the target centre relative to their weighted means, Δt is the time since the beginning of the observation and a_0, a_x, a_y, a_{xx}, a_{yy} and a_t are coefficients which are free parameters in the MCMC analysis. There are many methods of position measurement of the PSF that can be used. Normally the difference between these methods is very minor, however, there are certain cases where some methods break down. An example of this is when the PSF comes close to or crosses over a pixel boundary. This dependence on method was understood as part of the analysis of Mahtani et al. (2013) where we attempted to use both radial and polynomial decorrelation.

2.3.3.2 BiLinearly Interpolated Subpixel Sensitivity (BLISS) Mapping

Another method that has been used to remove the IPSVs in Spitzer data at 3.6 μm and 4.5 μm is BiLinearly Interpolated Subpixel Sensitivity (BLISS) Mapping (Stevenson et al. 2012). This method uses the residuals from the out-of-eclipse portion of the light curve to determine the sensitivity of the detector. Using bilinear splines to interpolate between the sampled regions on the detector, a map of the sensitivity of the detector can be built up by laying down a grid of knots and interpolating the sensitivity relative to the 4 nearest knots. The reason this is such a fast computation within an MCMC is that the interpolation weights can be computed prior to the MCMC. This map can be used in conjunction with a model for the measured flux to remove the IPSVs in the data. It is very important to bin the data such that the small fluctuations in

sensitivity (that are hard to pick up with polynomials) are detectable, for example the possible small scale corrugation seen by Ballard et al. (2010) who found sinusoidal like variations in sensitivity with a period of 0.05 pixels. However, this has not been seen for any other data set so the result should be treated with caution. However, the bin size must also large enough to sample the pixel space sufficiently. A disadvantage of this method is that one is self-calibrating the data so it is imperative to carefully check the results to make sure there are no correlations between the output results and the input model.

2.4 Wavelets

Fitting data that contains noise (i.e. real observations) can be computationally intensive if time-correlated noise is present in the data. A method that has been developed by Carter & Winn (2009) fits data and noise simultaneously with wavelet basis functions. These functions are very similar to the sine and cosine basis functions in Fourier analysis that are defined in frequency space but wavelets are defined in time space. The main motivation for using the wavelets is that it (nearly) diagonalises the covariance matrix. This matrix is used to calculate goodness of fit of a model to the data. However in general this matrix is non-diagonal, and the goodness of fit calculation involves an inversion of this matrix which is computationally intensive. If this is a diagonal matrix, or nearly so, the inversion that is required is not computationally intensive and fast compared to a non-diagonal covariance matrix. One of the major assumptions of this is that the noise has a power spectral density (PSD) given by

$$PSD = \frac{A}{f^{\gamma}}$$

where A is a constant, f is the frequency, and γ is an integer. As long as this holds, a constraint is imposed on the noise such that the model can distinguish signal and noise. This is a very fast method of analysis, $[O(N)]$, and has been shown by Carter & Winn (2009) to give more accurate results and realistic uncertainties for synthetic

transit lightcurve parameters in the case of $\gamma = 1$. In this work I use this method to determine if the secondary eclipse parameters' error bars are more conservative.

A wavelet approach can be thought of a two step process, first one starts with a set of basis functions that are obtained through translations and dilations of a so called father wavelet. Second, a set of nested detail functions that come from translations and dilations of a so called mother wavelet. This means that one starts with a floor resolution the signal and each successive higher resolution, the translation or dilation of the mother wavelet, contains all the information of the previous resolution and some extra detail. One of the important products of an analysis using a wavelet basis is that it diagonalises the covariance matrix and the value of these diagonal elements give an estimate of the red noise that is present in the data set.

3 Warm Spitzer Occultation Photometry of WASP-26b at $3.6\,\mu$m and $4.5\,\mu$m

3.1 Introduction

The first detections of thermal emission from exoplanets were reported by Deming et al. (2005) and Charbonneau et al. (2005). The teams observed the secondary eclipses of HD209458 and TrES-1 using the Spitzer Space Telescope. Secondary eclipses of about 30 other exoplanets have now been observed (e.g. Machalek et al. 2008; Anderson et al. 2011b; Todorov et al. 2012; Burrows 2014). Through the photometry of this event, observed using *Spitzer* and ground based telescopes, the spectral energy distribution (SED) of the irradiated hemisphere (day-side) of the planet can be built up. From the SED one can investigate the atmospheric properties of the day side of the planet. Secondary eclipse observations made with *Spitzer* have shown that some of these exoplanets have thermal inversions (Fortney et al. 2008; Knutson et al. 2009; Madhusudhan & Seager 2010). Thermal inversions are thought to form when gases exist in the upper atmosphere of these exoplanets that are efficient absorbers of optical and ultraviolet light (Fortney et al. 2008). This absorption of radiation causes the temperature of this region of the atmosphere to increase. Gases that have been hypothesised to cause thermal inversions to form are titanium oxide and vanadium oxide (Spiegel, Silverio & Burrows 2009) or sulphur compounds (Zahnle et al. 2009).

WASP-26b, discovered by Smalley et al. (2010) with SuperWASP (Pollacco et al. 2006), is a 1 Jupiter mass ($1M_{Jup}$) planet in a 2.8 day orbit around a G0 type star. WASP-26 also has a common proper motion companion 15" away (Smalley et al. 2010). Anderson et al. (2011a) conducted an investigation to measure the Rossiter-McLaughlin (R-M) effect to determine the sky-projected spin-orbit angle of the system. However, the noise in the data combined with the weak predicted signal ($15\,\mathrm{m\,s^{-1}}$) meant it was not possible to detect the R-M signal. Albrecht et al. (2012) constrained the spin-orbit angle of the system to $\lambda = -34^{+36}_{-26}\ ^{\circ}$. In this chapter I present new warm *Spitzer*

and ground based photometry of WASP-26. This work was presented in Mahtani et al. (2013), with section 3.3.1 mainly written by J. Southworth, section 3.4.1 mainly written by D. R. Anderson and J. Harrington and section 3.5.2 was mainly written by N. Madhusudhan .

3.2 Observations

I present *Spitzer* (Werner et al. 2004) InfraRed Array Camera (*IRAC*) (Fazio et al. 2004) channel 1 (3.6 μm) and channel 2 (4.5 μm) secondary eclipse (occultation) data taken on 2010 August 3 and 2010 September 7-8, respectively (PI: J H, Program ID 60003). The *Spitzer* data were acquired in full array mode (256 $\times$ 256 pixels). Also presented are new full transit data taken in the *g, r* and *i* bands (taken simultaneously) using the 2.2-m telescope at the Calar Alto Astronomical Observatory with the Bonn University Simultaneous CAmera (BUSCA) on 2010 August 20. BUSCA is a 4 channel CCD photometer with 4096 $\times$ 4096 pixels per CCD with a plate scale of 0.17 arc seconds per pixel. The BUSCA transit data were obtained using defocused photometry (Southworth et al. 2009c, 2012) and BUSCA was used with a 256 $\times$ 1400 pixel window and 2$\times$2 binning to reduce the read out time. Table 3.1 is a summary of the data that I have used in this analysis.

Observation	Dates	Publication
SuperWASP Lightcurves (400 - 700 nm filter)	2008 June 30 - 2008 November 17 2009 June 28 - 2009 November 17	Smalley et al. (2010)
16 RV spectra from CORALIE (1.2m Swiss Telescope,La Silla, Chile)	2009 June 19 - 2009 August 22	Smalley et al. (2010)
30 RV spectra from HARPS (HARPS Spectrograph, ESO 3.6m telescope, La Silla, Chile)	2010 September 12	Anderson et al. (2011a)
Full transit (Pan-STARRS-z filter) (2.0m Faulkes Telescope South, Siding Spring, Australia)	2009 November 18	Smalley et al. (2010)
Occultation (3.6μm) (*Spitzer* channel 1)	2010 August 3	This Paper
Occultation (4.5μm) (*Spitzer* channel 2)	2010 August 7 - 2010 August 8	This Paper
Full transit (*g*, *r* and *i* band) (Calar Alto Astronomical Observatory with BUSCA, Almería, Spain)	2010 August 20	This paper

Table 3.1: Summary of data used in this analysis.

3.3 Data Reduction

3.3.1 Transit Data Reduction

Jeremy Tregloan-Reed and John Southworth used the IDL implementation of DAOPHOT (Stetson 1987) to perform synthetic aperture photometry on the BUSCA images, as in Southworth et al. (2009c). In all three bands one comparison star was used with a target aperture radius of 24 pixels, a sky annulus of inner radius 70 pixels and an outer radius 100 pixels. The wings of the PSF of the companion star do contaminate the target aperture but the contribution to the observed flux is negligible. Iterative outlier removal was used on the image values in the sky annulus to remove the effect of the light from the wings of the companion's PSF in the sky annulus. The light curves are shown in Figure 3.1.

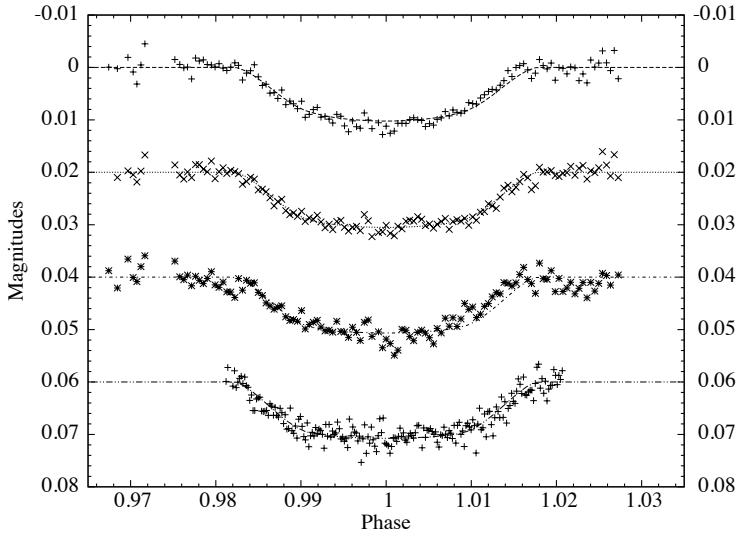

Figure 3.1: BUSCA and FTS data with best fitting models (from the top to bottom), g band data, r band data, i band data and the FTS (z filter) data.

3.3.2 *Spitzer* Data Reduction

I reduced the *IRAC* data with the Image Reduction and Analysis Facility (IRAF)[1] using the same method as Anderson et al. (2011b), described briefly here. Conversion from MJy/sr to electrons was done using equation (3.1), where the gain, exposure time and flux conversion factor were taken from the image headers.

$$\text{Factor} = \frac{\text{Gain} \times \text{Exposure Time}}{\text{Flux Conversion Factor}} \tag{3.1}$$

Aperture photometry was then conducted using the PHOT procedure in IRAF, using 21 aperture radii in the range 1.5-6 pixels and with a sky annulus of inner radius 8 pixels and outer radius 16 pixels. It was found that the stellar companion to WASP-26 and a bad column in channel 2 data were both inside the sky annulus. However, an iterative 3-sigma clipping was conducted which excludes those pixels. The error on the photometry was calculated from the photon statistics and the read out noise of the *IRAC* detectors. The readout noise values were taken from the IDL program SNIRAC_warm.pro,[2] the values for channel 1 and 2 are 9.87 and 9.4 electrons, respectively. The position of the target was measured by fitting a 1-dimensional Gaussian to the marginal distributions of flux on x and y image axes. For each data set the times of mid-exposure were converted to BJD_{TDB} (Eastman, Siverd & Gaudi 2010) and for the occultation data the light travel time across the system ($\sim$40s) was accounted for. The light travel time across the system was calculated using the semi-major axis from the output of our initial Markov Chain Monte Carlo (see below for details of this run) and this time was subtracted from all the *Spitzer* times.

[1] IRAF is distributed by the National Optical Astronomy Observatories, which are operated by the Association of Universities for Research in Astronomy, Inc., under cooperative agreement with the National Science Foundation.

[2] *ssc.spitzer.caltech.edu/warmmission/propkit/som/snirac_warm.pro*

3.4 Analysis

3.4.1 Markov Chain Monte Carlo

The parameter space was explored using a Markov chain Monte Carlo (MCMC) algorithm (Collier Cameron et al. 2007; Pollacco et al. 2008; Enoch et al. 2010). The input parameters for the star that were used in the MCMC analysis are $T_{\rm eff} = 5950 \pm 100$ and [Fe/H] $= -0.02 \pm 0.09$ (Anderson et al. 2011a) which are derived from spectral analysis. Stellar density is directly derived from the transit light curve (Seager & Mallén-Ornelas 2003). The radial velocity constrains the $e \sin \omega$ and the timing of the secondary eclipse constrains $e \cos \omega$. These two parameters are used as proposal parameters to constrain the eccentricity of the planet's orbit. The latest values of $T_{\rm eff}$ and [Fe/H] (which are controlled by Gaussian priors) are input into the empirical mass calibration of Enoch et al. (2010) to obtain an estimate of the stellar mass and radius, $M_\star$ and $R_\star$. These are then used to calculate the planet's mass and radius. At each step in the MCMC procedure, each proposal parameter is perturbed from its previous value by a small, random amount. From the proposal parameters (Table 3.3), model light and RV curves are generated and χ^2 is calculated from their comparison with the data. A step is accepted if χ^2 (the merit function) is lower than for the previous step, and a step with higher χ^2 is accepted with probability $\exp(-\Delta\chi^2)$. In this way, the parameter space around the optimum solution is thoroughly explored. The value and uncertainty for each parameter are taken as the median and central 68.3 per cent confidence interval of the parameter's marginalised posterior probability distribution, respectively (Ford 2006). The median closely approximates the χ^2 minimum for symmetric posteriors such as these, and is more robust to noise in the case of flat minima. Table 3.3 shows the proposal parameters of the MCMC. I conducted an initial run which included all the transit photometry, including WASP photometry, to get an estimate of the epoch of mid-transit. This value along with its uncertainty were used as a Bayesian prior in subsequent MCMC runs which used all the photometry, including *Spitzer*, but excluding the WASP photometry (to reduce computing time). The transit model used

in the analysis was the small planet approximation of Mandel & Agol (2002) with 4-parameter limb darkening coefficients taken from Claret (2004). The limb darkening coefficients were determined using an initial interpolation in $\log g_\star$ and [Fe/H] with an interpolation in $T_{\rm eff}$ at each MCMC step. The limb darkening parameters used for the best-fit lightcurves are given in Table 3.4. The secondary eclipses were analysed by approximating the planet as a uniform disc. The projected spin-orbit angle was fixed to the value $\lambda = 0$ in the fit since the HARPS data covering the transit are negligibly affected by the R-M effect. The fit to the optical lightcurves (Figure 3.1) shows that there is some correlated noise present in the g and i band lightcurves. The small additional uncertainty due to this noise has been accounted for in the quoted parameter standard errors rather than trying to find an arbitrary model that would improve the fit. This was done by inflating (multiplying by a factor) the error bars on the photometric data points in the MCMC code such that the reduced χ^2 fit to the data was 1. For the transit data inflation was conducted pre and post burn-in and only post burn-in for the secondary eclipse. For the transit data if the pre-burn-in inflation is adequate then the post-burn-in inflation should be very close to 1. The factors of inflation are shown in Table 3.2.

Observation	Inflation factor pre-burn-in	Inflation factor post-burn-in
Pan-STARRS z band	1.099	1.035
IRAC 3.6μm	-	1.006
IRAC 4.5μm	-	1.044
BUSCA g	4.622	0.905
BUSCA r	5.587	1.024
BUSCA i	5.283	0.950

Table 3.2: Summary of data used in this analysis.

The only correlations in the proposal parameters were those between transit depth, width and impact parameter often seen in ground based lightcurves (Figure 3.2).

These correlations are caused by the blurring of the second and third contact points due to limb darkening in the optical lightcurves. These correlations do not affect our secondary eclipse depth measurements as can be seen from the bottom two plots in Figure 3.2. Chain convergence was checked for both by visual inspection and using the Gelman-Rubin (G-R) statistic (Gelman et al. 2003; Ford 2006). This was done by first splitting the posterior distributions of the proposal parameters from our 200,000 iteration MCMC into 5 subsets, each containing 40,000 values. Then the G-R script from Eastman, Gaudi & Agol (2013) was used to calculate the G-R statistic for each proposal parameter posterior distribution. It was found that the G-R test showed the chains had converged as all the values of the G-R statistic were less than 1.01.

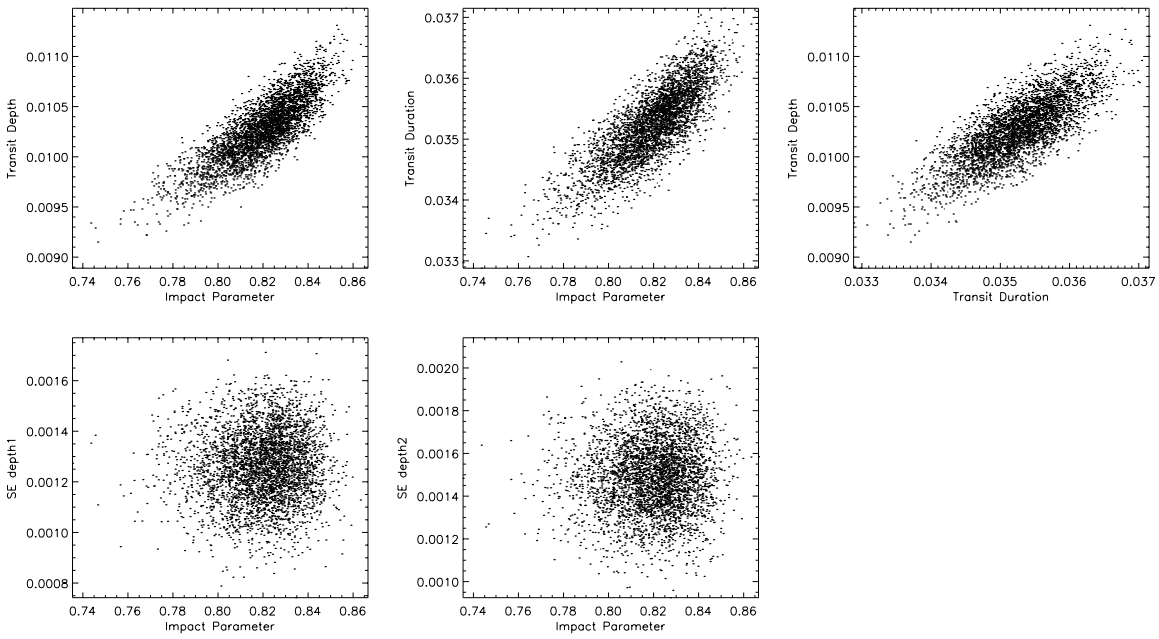

Figure 3.2: Correlation plots for selected proposal parameters from our MCMC analysis. For clarity I have only plotted a random 2% of the chain values. (SE depths are the secondary eclipse depths)

T_c	Time of mid transit
P	Period of planet
ΔF	Depth of transit
T_{14}	Transit duration
b	Impact parameter
K_1	Stellar radial reflex velocity
$T_{\rm eff}$	Effective temperature of the star
$[\frac{Fe}{H}]$	Metallicity of the star
$\sqrt{e}\cos\omega$ $\sqrt{e}\sin\omega$	e=eccentricity, ω = argument of periastron
$\Delta F_{3.6}$	Depth of secondary eclipse at 3.6μm
$\Delta F_{4.5}$	Depth of secondary eclipse at 4.5μm

Table 3.3: Proposal parameters of the model used in our MCMC analysis

Light Curve	a_1	a_2	a_3	a_4
FTS	0.655	−0.352	0.645	−0.329
BUSCA (g band)	0.433	0.208	0.496	−0.300
BUSCA (r band)	0.555	0.028	0.445	−0.278
BUSCA (i band)	0.641	−0.267	0.640	−0.338

Table 3.4: Limb darkening coefficients

3.4.2 Trend Functions and Aperture size

Figure 3.3a shows an example of the 3.6 μm light curve produced by the photometry in IRAF. There is a steep increase in the measured flux during the first part of the observation. This occurs because the telescope has slewed from its old position to its new position and is adjusting to a new equilibrium. I exclude the data that precedes HJD=2455447.37, to remove the major part of the initial ramp. No ramp was seen in the channel 2 data so this clipping was not conducted. It can be seen that there is a clear periodic trend in the data. This is due to the variation in the position of the target on

the detector caused by flexure of the instrument as an electric heater is turned off and on[3]. The *IRAC* detectors are known to exhibit inhomogeneous intrapixel sensitivity (e.g. Knutson et al. 2008), which means that individual pixels have inhomogeneous sensitivity gradient. This along with the PSF movement results in the measured flux varying depending on the position of the PSF on the detector. Also, when small apertures are used pixelation occurs due to the under-sampling of the PSF of the target (Anderson et al. 2011b). These systematics are accounted for in the trend functions as described in chapter 2.3.3.1. Figure 3.3b shows an example of the 4.5 μm data which is less affected by these systematics even though (as it can be seen from Figure 3.4) the radial motion of the PSF is greater at 4.5 μm than at 3.6 μm. The explanation for this is still unknown.

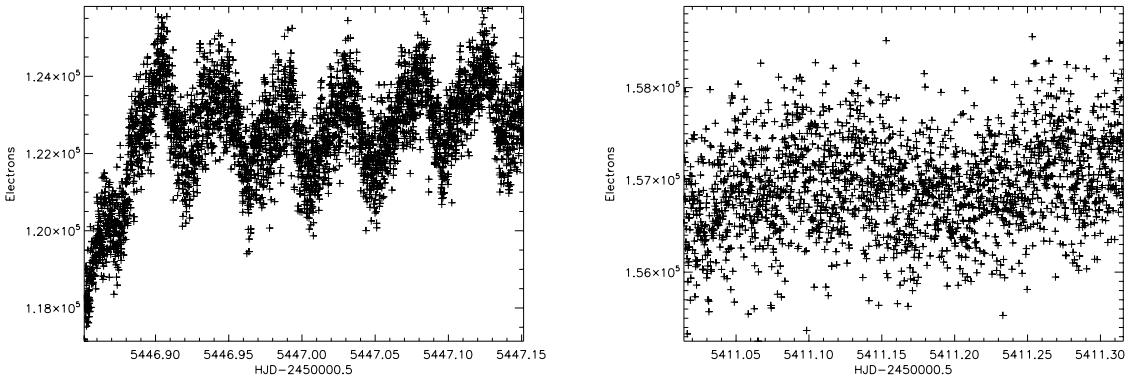

(a) (b)

Figure 3.3: (a) The raw light curve of the 3.6 μm *Spitzer* data extracted using and aperture of 2.4 pixels. (b) The raw light curve of the 4.5 μm *Spitzer* data extracted using an aperture of 2.4 pixels

For each set of trial lightcurve model parameters the residuals from the model are calculated and then the coefficients of the detrending model are calculated using

[3] *ssc.spitzer.caltech.edu/warmmission/news/21oct2010memo.pdf*

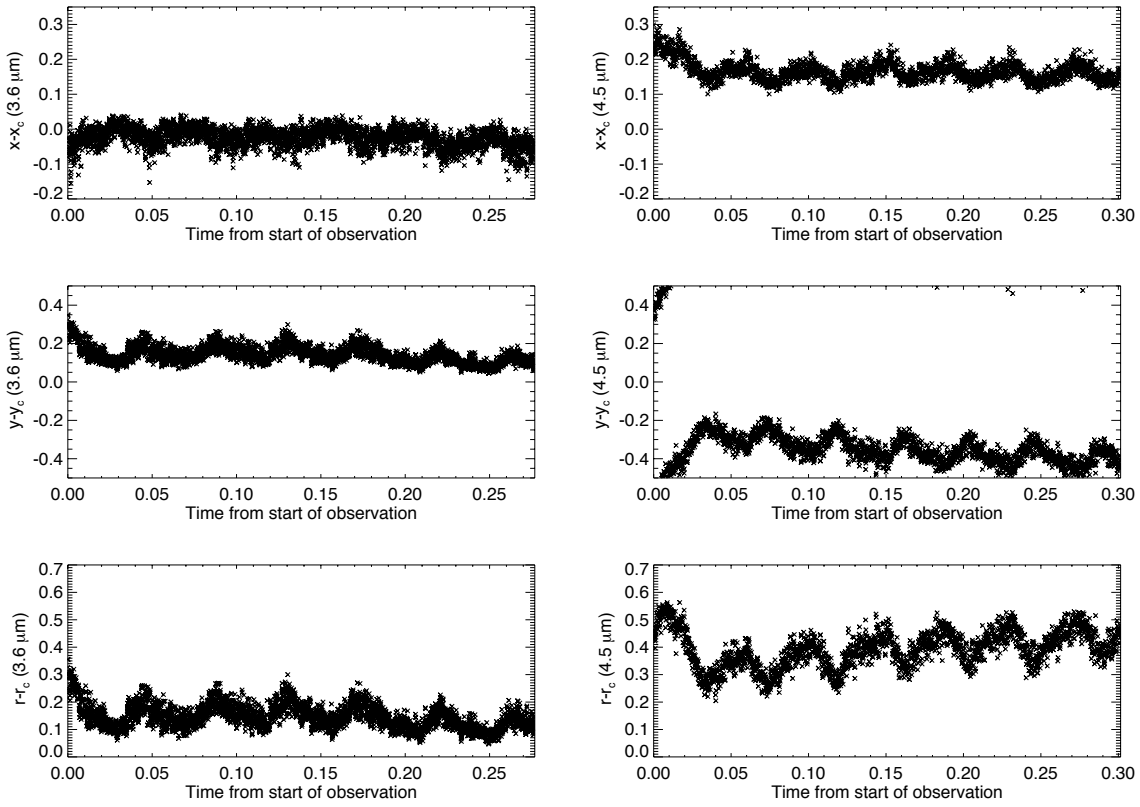

Figure 3.4: The top, middle and bottom plots of the each column show the distance of the PSF from the nearest pixel centre in x, y and radially in each of the measured wavelengths respectively.

singular value decomposition applied to the entire data set. Initially, a linear-in-time and quadratic-in-space trend function was used on all 21 apertures to fit the secondary eclipse data. The RMS of the residuals was used to determine the optimal aperture size. Once this was determined, combinations of no, linear and quadratic trend functions in time and space were used on the best aperture to determine the best fitting trend function.

Initially this decorrelation was conducted using the positions measured by the 1-dimensional Gaussian fit to the target. The pixel sensitivity functions for *IRAC* vary strongly as a function of the radial position of the PSF from the centre of the pixel

(Deming et al. 2011), therefore, I also attempted to remove the trends in the data by decorrelating against the radial position (radial distance from the centre of the nearest pixel) instead of the x and y positions independently. The general trend function for the radial decorrelation is,

$$\Delta f = b_0 + b_1 r + b_2 r^2 + b_t \Delta t, \tag{3.2}$$

where b_0, b_1, b_2, b_t are free parameters in the MCMC analysis and r is the radial distance from the centre of the nearest pixel centre. A third method that was attempted was to use target positions in the trend functions measured by fitting a two dimensional circular Gaussian of fixed full width half maximum (1.39 pixels in channel 1 and 1.41 pixels in channel 2) to a small region of the images containing the target.

To determine which trend function gave better results the Bayesian Information Criterion (BIC) was used (Schwarz 1978),

$$\mathrm{BIC} = \chi^2 + k \ln(n) \tag{3.3}$$

where k is the number of free parameters and n is the number of data points. This method of determining how complicated a model to use only accepts a higher order trend function if the fit improves χ^2 by $\ln(n)$ or better for each additional free parameter.[4]

Using the RMS of the residuals it was found that the best aperture to use was 2.4 pixels in both channels. It was also found that the RMS of the residuals to the channel 1 data were marginally lower when using the 2D circular Gaussian method to measure the PSF compared to the 1D Gaussian position measurements (0.002995 compared to 0.003054). The channel 2 data gave consistent RMS no matter the position measurement used. The system parameters were consistent no matter which position measurement system were used. The results shown in Figure 3.5 and Table 3.5 are those using the 2D circular Gaussian method, extracted from the 2.4 pixel aperture and trend functions as described below. It was found that the radial decorrelation gave

[4]This is assuming a large number of data points and that the errors are part of a normal distribution

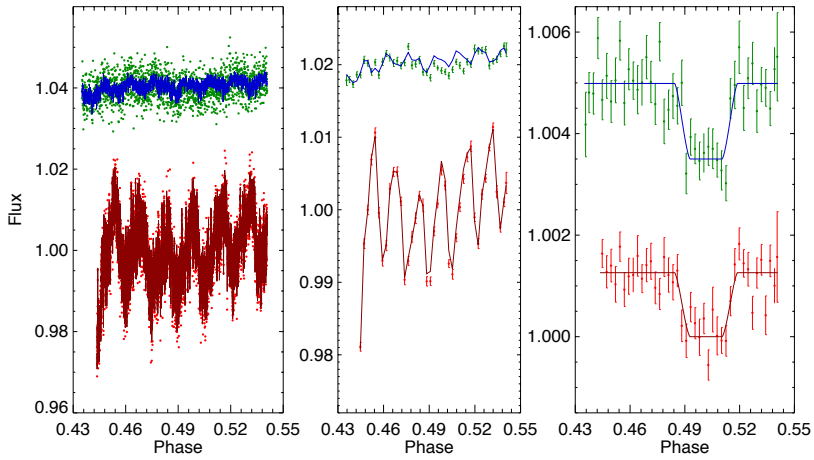

Figure 3.5: (Left): The raw light curves with the trend functions, the upper points are the channel 2 data and the lower points are the channel 1 data, the solid lines are the trend functions for each data set. (Middle) Binned light curves with trend models. (Right) The binned light curve with trend function removed and best fitting eclipse models (solid lines). The secondary eclipse can clearly be seen in both channels.

a worse fit to our data compared to that of x and y decorrelation (χ^2 worse by ~ 3000 at $3.6\,\mu$m and ~ 400 at $4.5\,\mu$m).

Using equation (3.3) it was found that the quadratic-in-space with no time trend function gave the best fit to the data in channel 1 and that the linear-in-space with no time trend function gave the best fit to the data in channel 2. It was found that the addition of the quadratic term for the spatial decorrelation improved our BIC by ~ 200 in channel 1. The improvement in BIC for the channel 2 data was less than ~ 10 for more complicated models than linear-in-space with no time trend. I also attempted detrending the data based only on the out-of-eclipse points. This was attempted to see if this affected the measured eclipse depths. It was found that the eclipse depths were consistent with the previous decorrelation. This shows that the eclipse is a real feature in the data and not just an artefact created by the removal of the IPSVs.

Table 3.5: System parameters from our MCMC analysis

Parameter	Symbol (unit)	Value
Orbital period	P (d)	2.756611 ±0.000008
Epoch of mid-transit (BJD, TDB)	$T_{\rm c}$	2455424.10899 ±0.00012
Transit duration (first to fourth contact)	T_{14} (d)	0.097 ±0.002
Duration of transit ingress ≈ duration of transit egress	$T_{12} \approx T_{34}$ (d)	0.024 ±0.002
Planet-to-star area ratio	$\Delta F = R_{\rm P}^2/{\rm R}_*^2$	0.0103 ±0.0003
Impact parameter	b	0.82 ±0.02
Orbital inclination	i (°)	82.9 ±0.4
Semi-amplitude of the stellar reflex velocity	K_1 (km s^{-1})	0.138±0.002
Centre-of-mass velocity	γ (km s^{-1})	8.4593 ±0.0001
Argument of periastron	ω (°)	-90^{+200}_{-20}
	$e\cos\omega$	−0.0004 ±0.0007
	$e\sin\omega$	$-0.0011\ ^{+0.0023}_{-0.0110}$
Orbital eccentricity	e	$0.00283\ ^{+0.00965}_{-0.00221}$
Phase of mid-occultation	$\phi_{\rm mid-occultation}$	0.4998 ±0.0005
Occultation duration	T_{58} (d)	0.097 ±0.002
Duration of occultation ingress ≈ duration of occultation egress	$T_{56} \approx T_{78}$ (d)	0.024±0.002
Star mass	M_* ($M_\odot$)	1.10±0.03
Star radius	R_* ($R_\odot$)	1.29±0.05
Star surface gravity	$\log g_*$ (cgs)	4.26 ±0.03
Star density	ρ_* ($\rho_\odot$)	0.52±0.06
Star effective temperature	$T_{\rm eff}$ (K)	6000±100
Star metallicity	[Fe/H]	−0.02±0.09
Planet mass	$M_{\rm P}$ ($M_{\rm Jup}$)	1.03±0.02
Planet radius	$R_{\rm P}$ ($R_{\rm Jup}$)	1.27 ±0.07
Planet surface gravity	$\log g_{\rm P}$ (cgs)	3.16 ±0.04
Planet density	$\rho_{\rm P}$ ($\rho_{\rm J}$)	0.50 ±0.08
Semi-major axis	a (AU)	0.0398 ±0.0003
Occultation depth at 3.6μm	$\Delta F_{3.6}$	0.00126 ± 0.00013
Occultation depth at 4.5μm	$\Delta F_{4.5}$	0.00149 ± 0.00016
Planet equilibrium temperature (full redistribution)*	$T_{\rm P,A=0,f=1}$ (K)	1623 ±43
Planet equilibrium temperature (day-side redistribution)*	$T_{\rm P,A=0,f=2}$ (K)	1930 ± 51
Planet equilibrium temperature (instant reradiation)*	$T_{\rm P,A=0,f=\frac{8}{3}}$ (K)	2074 ± 55

* where A is the albedo, f=1 is defined as full redistribution,
f=2 is day-side redistribution,
and f=$\frac{8}{3}$ is instant reradiation as in Smith et al. (2011)

3.5 Results and Discussion

3.5.1 Eclipse Depths and Brightness Temperatures

I find that the eclipse depths at 3.6 μm and 4.5 μm relative to an out-of-eclipse value of 1 are 0.00126 ± 0.00013 and 0.00149 ± 0.00016, respectively. These eclipse depths correspond to brightness temperatures of 1825 ± 80K and 1725 ± 89K. To find these blackbody temperatures the expected flux ratios were calculated using Planck functions at different temperatures for the planet and synthetic spectra from stellar models (Philip, Upgren & Janes 1991) for the star. These flux ratios were then integrated over the *Spitzer* band passes to calculate the expected measured flux ratio. The temperatures above correspond to the best fitting Planck function temperature to the individual eclipse depths. The errors were calculated using a simple Monte Carlo method.

The brightness temperatures suggest that, on average, the emission at mid-infrared wavelengths from the irradiated hemisphere of WASP-26b is consistent with the spectrum of an isothermal atmosphere, with the possibility of a weak thermal inversion within the uncertainties on the brightness temperatures. The brightness temperatures lie somewhere between the full and dayside-redistribution equilibrium temperatures as shown in Table 3.5 so the amplitude of the thermal phase curve of the planet will be non-zero. Full orbit observations of the system at the same wavelengths as these observations can be used to test this prediction.

3.5.2 Atmospheric Analysis

Nikku Madhusudhan compared my measurements of the eclipse depths of WASP-26b to hot Jupiter atmospheric models which use the spectral retrieval technique of Madhusudhan & Seager (2009); Madhusudhan & Seager (2010). The model computes line-by-line radiative transfer in a plane-parallel atmosphere in local thermodynamic equilibrium, and assumes hydrostatic equilibrium and global energy balance. The input parameters of the model are the temperature-pressure- (T-P) profile of the at-

mosphere and the chemical composition, i.e. the sources of molecular line opacity. The model atmosphere includes the major sources of opacity expected in hot, hydrogen-dominated atmospheres, namely, molecular absorption due to H_2O, CO, CH_4, and CO_2, and continuum opacity due to H_2-H_2 collision-induced absorption (CIA). The molecular line-lists used are discussed in Madhusudhan & Seager (2009) and Smith et al. (2012). Given a photometric or spectral dataset of thermal emission from the planet, the space of atmospheric chemical composition and temperature structure was explored to determine the regions in model space that explain, or are excluded by, the data (e.g. Madhusudhan et al. 2011). In the present case the number of available data points ($N = 2$) are far below the number of model parameters ($N = 10$), implying that a unique model fit to the data is not feasible. Consequently, the chemical composition of the models was nominally fixed to that obtained with solar elemental abundances in thermochemical equilibrium (e.g. Burrows & Sharp 1999; Madhusudhan 2012). For a given thermal profile the model then explored the space of thermal profiles, with and without thermal inversions, that might explain the data.

Figure 3.6 shows the 3.6 μm and 4.5 μm data along with model spectra of atmospheres with and without a thermal inversion, and a blackbody model. All three models shown allow for very efficient day-night redistribution. It can be seen that both the planet-star flux ratios can be explained by a planetary blackbody at around 1750 K. Consequently, the data are consistent with an isothermal atmosphere. However, an isothermal temperature profile may be unphysical in radiatively efficient atmospheres at low optical depth (e.g. Hansen 2008). A temperature profile with a non-zero thermal gradient, with or without a thermal inversion, may be more plausible. As shown in Fig. 3.6, the two data points are fit almost equally well by models with and without a thermal inversion, as shown by the red and green models, respectively. Further occultation depths measured at different wavelengths are required to break the degeneracies between the models and to determine the true nature of the atmosphere. It can be seen in Fig. 3.6 that there are some differences between the models with and without a thermal inversion at 1.25 μm (J band), 1.65 μm (H band) and 2.2 μm (K band). These wavelengths are accessible from the ground, so with measurements of the sec-

ondary eclipse depth at these wavelengths it may be possible to break the degeneracies between these models. Hubble Space Telescope WFC3 observations covering the wavelength range $1-1.7\,\mu$m can also be used to detect spectral features due to water either in emission or absorption, and so distinguish between models with and without a thermal inversion (Madhusudhan 2012; Swain et al. 2013). It should be emphasised here that only presented here are two possible models that represent the average properties of the irradiated hemisphere of WASP-26b. With additional data other parameters of the models such as composition can be explored.

3.5.3 Activity-Inversion Relation

Knutson, Howard & Isaacson (2010) (hereafter K10) presented results which suggest that planets without thermal inversions orbit active stars, and those with inversions orbit inactive stars. This may be due to photodissociation of the opacity source in the upper atmosphere of the planet by the UV flux from the active stars (K10). However, the time between a measurement of the activity of a star being measured and eclipse being observed can be on the timescale of months/years. It is known that solar-like stars have activity cycles on time scales of approximately 10 years. I used the Duncan et al. (1991) catalogue of S_{HK} activity measurements taken at the Mount Wilson Observatory to examine to what extent the activity of a star changes on short time scales (order of months) and long time scales (order of years). The aim was to determine if the variability in activity of the stars in the K10 sample was such that, in the time between the occultation observation and the measurement of $\log R'_{HK}$, the activity of the star can change enough to affect the interpretation of this activity-inversion relation. Recently Montalto et al. (2012) showed that the activity of WASP-3 changed from $\log R'_{HK} = -4.95$ (less active) to $\log R'_{HK} = -4.8$ (more active) between 2007 and 2010. It has been shown by Menou & Rauscher (2009) that the time scale for models of hot Jupiter atmospheres to go from their initial conditions to a statistical steady state was ~ 20 days. This suggests the time scale of hot Jupiter atmosphere variability is much shorter than the time scale of stellar activity variability. More detailed modelling

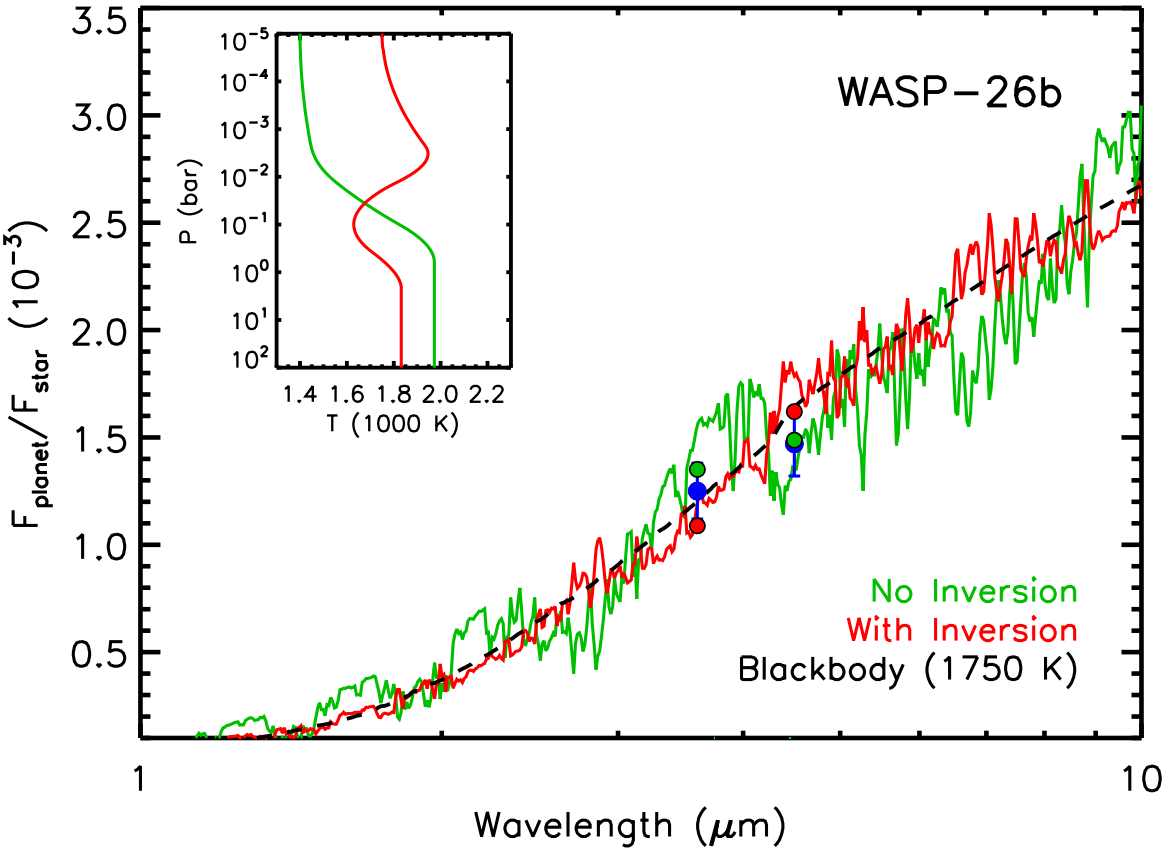

Figure 3.6: Spectral energy distribution of WASP-26b relative to that of its host star. The blue circles with error bars are our best-fitting occultation depths. The green line is a model-atmosphere spectrum, based on a model which assumes solar abundances in thermochemical equilibrium and lacks a temperature inversion, and the dark red line is a model with a temperature inversion. The band-integrated model fluxes are indicated with circles of the corresponding colours. The dashed black line shows a planetary black body model with a temperature of 1750K. Inset: temperature-pressure profiles for our models.

and additional observations are required to better understand whether variations in the UV irradiation can produce observable changes in the eclipse depths for planets near the boundary between atmospheres with and without strong thermal inversions.

I converted the S_{HK} measurements in Duncan et al. (1991) to $\log R'_{HK}$ using the method described by Noyes et al. (1984). A look-up table based on $\log R'_{HK}$ and B–V colour for the stars in the Duncan et al. (1991) catalogue was then constructed. Using this table, the within-season variation of $\log R'_{HK}$ of the stars was used as a measure of the short term variability in $\log R'_{HK}$ and the season-to-season variation in $\log R'_{HK}$ as a measure of the long term variation in $\log R'_{HK}$. This look up table was then used to estimate the variation in $\log R'_{HK}$ for the stars of K10 based on their B−V colour. It was found that the short term variability was always ≤ 0.02 dex and the long term variability was between 0.02 and 0.06 dex. This suggests that the variation in $\log R'_{HK}$ is not large enough on either short nor long term time scales to change the interpretation of K10. However, this may blur the boundary between the two classes of planets. The error bar shown in Figure 3.7 is the typical change in activity, assuming the spectra are measured over several nights. It is possible for stars to vary by much more than this amount over their rotation period (e.g. Dumusque et al. 2012). This short time scale variation will move the star on the diagram but this may not reflect changes in UV irradiation. The value of $\log R'_{HK} = -4.98$ for WASP-26 used in this analysis is taken from Anderson et al. (2011a).

I compiled updated values of $R_p/R_\star$ and the secondary eclipse depths for the stars in the K10 sample. Figure 5 of K10 was then replotted, this is shown in Figure 3.7. I include on this plot WASP-26b. As can be seen from Figure 3.7, it seems to lie very close to the boundary between the two classes. Using the convention as in Anderson et al. (2013) the abscissa value for WASP-26b is $\zeta = -0.020 \pm -0.023\% \, \mu\mathrm{m}^{-1}$, where ζ is the gradient of the measurements at $3.6\,\mu$m and $4.5\,\mu$m, i.e. $\Delta F_{3.6} - \Delta F_{4.5}/(-0.9\,\mu\mathrm{m})$, minus the gradient of the blackbody that is the best–fit to the two measurements. The theory behind this is that at $4.5\,\mu$m there are opacity sources that are not present at $3.6\,\mu$m (CO and H_2O) (Madhusudhan & Seager 2010). The $4.5\,\mu$m data probes a higher region of the atmosphere compared to the $3.6\,\mu$m data. This suggest that if the brightness temperature at $4.5\,\mu$m is greater than that at $3.6\,\mu$m then there is likely to be a thermal inversion in the atmosphere.

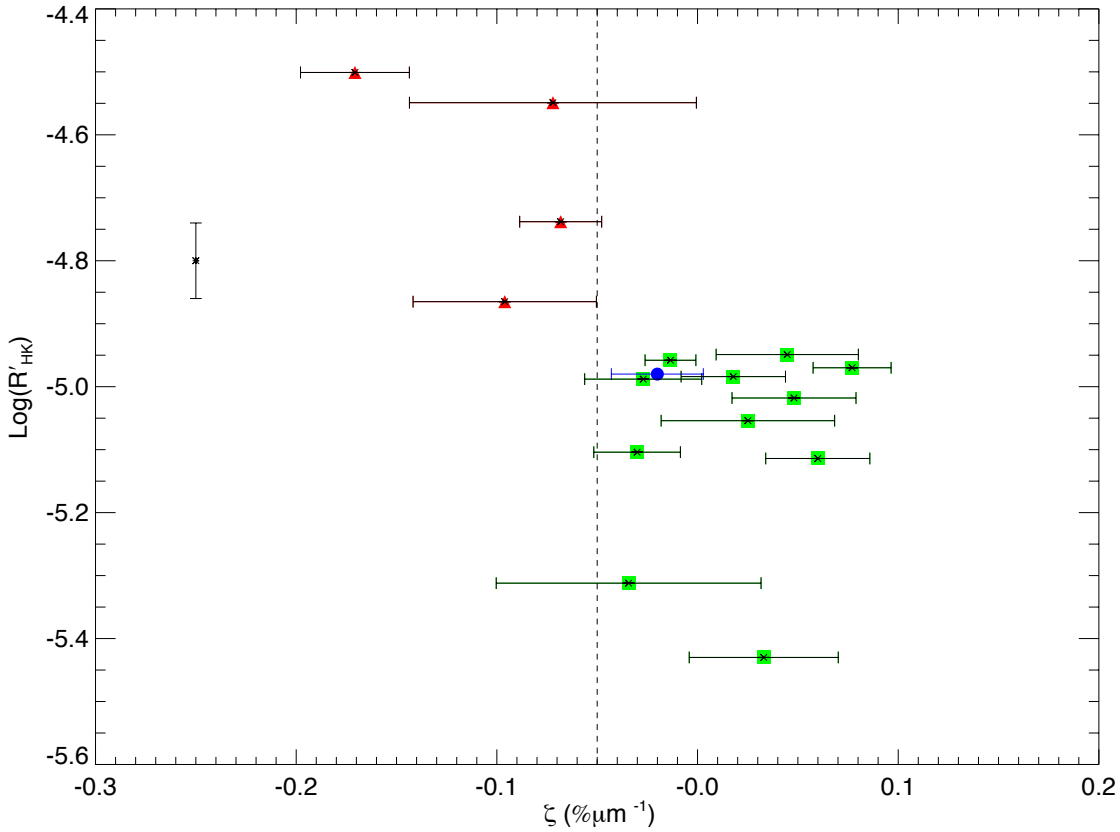

Figure 3.7: Activity-inversion plot for the stars in Knutson, Howard & Isaacson (2010). Points on the left of the dotted line (triangles) are non-inverted planets around active stars and those on the right of the dotted line (squares) are inverted planets around inactive stars. The point on the left hand side of the plot shows the typical change in $\log R'_{HK}$ (season-to-season), assuming measurements over several nights. The blue circle is WASP-26. The stars are listed in table 3.6.

Star	Log(R'_{HK})	ζ value	$R_P/R_\star$	Eclipse depth at 3.6 μm	Eclipse depth at 4.5 μm
HD189733	-4.501^*	-0.1707 ± 0.0271	Carter & Winn (2010)	Charbonneau et al. (2008)	Charbonneau et al. (2008)
TRES-3	-4.549^*	-0.0721 ± 0.0715	Southworth (2011a)	Fressin et al. (2010)	Fressin et al. (2010)
TRES-1	-4.738^*	-0.0682 ± 0.0204	Southworth (2008)	K10	Charbonneau et al. (2005)
WASP-4	-4.865^*	-0.0961 ± 0.0457	Southworth et al. (2009a)	Beerer et al. (2011)	Beerer et al. (2011)
XO-2	-4.988^*	-0.0271 ± 0.0292	Southworth (2010)	Machalek et al. (2009)	Machalek et al. (2009)
TRES-2	-4.949^*	0.0447 ± 0.0354	Southworth (2011b)	O'Donovan et al. (2010)	O'Donovan et al. (2010)
XO-1	-4.958^*	-0.0135 ± 0.0127	Burke et al. (2010)	Machalek et al. (2008)	Machalek et al. (2008)
HAT-P-1	-4.984^*	0.0178 ± 0.0260	Southworth (2008)	Todorov et al. (2010)	Todorov et al. (2010)
HD209458	-4.970^*	0.0770 ± 0.0194	Southworth (2008)	Knutson et al. (2008)	Knutson et al. (2008)
TRES-4	-5.104^*	-0.0301 ± 0.0216	Southworth (2012)	Knutson et al. (2009)	Knutson et al. (2009)
COROT-1	-5.312^*	-0.0343 ± 0.0660	Southworth (2011b)	Deming et al. (2011)	Deming et al. (2011)
WASP-1	-5.114^*	0.0599 ± 0.0259	Southworth (2008)	Wheatley et al. (2010)	Wheatley et al. (2010)
WASP-2	-5.054^*	0.0251 ± 0.0432	Southworth et al. (2010)	Wheatley et al. (2010)	Wheatley et al. (2010)
WASP-18	-5.430^*	0.0332 ± 0.0176	Southworth et al. (2009b)	Maxted et al. (2013)	Maxted et al. (2013)
HAT-P-7	-5.018^*	0.0481 ± 0.0309	Southworth (2011b)	Christiansen et al. (2010)	Christiansen et al. (2010)
WASP-26	-4.98^{**}	-0.0200 ± 0.0229	This paper	This paper	This paper

* Log(R'_{HK}) value from Knutson, Howard & Isaacson (2010)

** Log(R'_{HK}) value from Anderson et al. (2011a)

Table 3.6: Stars in Figure 3.7

3.5.4 Eccentricity

In section 1.4 I discussed the reasons that eccentricity of hot Jupiter exoplanets needs to measured. Briefly, secondary eclipse measurements make it possible to constrain the eccentricity of the orbit from timing of the secondary eclipse relative to transit. I find that the eccentricity of the orbit is small ($e = 0.0028^{+0.0097}_{-0.0022}$), which is consistent with a circular orbit at the 1σ level. I find a 3σ upper limit on the eccentricity of the planet's orbit of 0.0399 which is similar to Anderson et al. (2011a) 3σ upper limit of 0.048. The fact that there is negligible eccentricity implies that there is no significant heating of the planet caused by tidal dissipation.

3.6 Conclusion

In this chapter I present new warm *Spitzer* photometry of WASP-26 at $3.6\,\mu$m and $4.5\,\mu$m along with new transit photometry taken in the *g,r* and *i* bands. I report the first detection of the occultation of WASP-26b with eclipse depths at $3.6\,\mu$m and $4.5\,\mu$m of 0.00126 ± 0.00013 and 0.00149 ± 0.00016 respectively which correspond to brightness temperatures of 1825 ± 80K and 1725 ± 89K. My analysis shows that the atmosphere of WASP-26b is consistent with an isothermal atmosphere with the possibility of a weak thermal inversion (within the uncertainties on the brightness temperatures). If the K10 activity-inversion relation holds for WASP-26b, then it would be expected to host a thermal inversion. More secondary eclipse data at different wavelengths, particularly near-IR secondary eclipse depths near the peak of the planet's SED, will be able to better constrain the true nature of the atmosphere of WASP-26b.

4 Reanalysis of WASP-12: Full Orbit Lightcurves at 3.6 μm and 4.5 μm

4.1 Introduction

Section 1.5.2.3 discusses the information that can be gained from thermal phase curves of exoplanets. The systematic noise in Spitzer data is currently the limiting factor in getting the most information out of the data. It is possible to account for some of these systematics, e.g., IPSVs. However, there is systematic noise in IRAC photometry on timescales of hours-days at the 0.01% level that has not been well characterised (Maxted et al. 2013). Different groups analyse Spitzer data in very similar ways. The subtle difference between analysis methods is the way the IPSVs are accounted for. The goal of this analysis is to determine if different analysis methods can give consistent results. If they cannot, then comparing conclusions from independent analyses is not feasible. The method that will be used to conduct this analysis is to re-analyse the WASP-12b full orbit light curves at 3.6 μm and 4.5 μm. The reduction will be conducted using the method of Maxted et al. (2013) (as applied to WASP-18b) and the results compared to that of the analysis of Cowan et al. (2012).

Cowan et al. (2012) presented full orbit light curves of WASP-12b, a highly inflated hot Jupiter, at 3.6 μm and 4.5 μm. The planet is thought to be undergoing Roche-Lobe overflow (Li et al. 2010). If this is occurring then the shape of the planet will be more tear-drop shaped rather than spherical. This deformation of the planet is predicted to be visible in the phase curve of the planet as an extra sinusoidal variation in the light curve which would have a period of half the orbital period. This is known as ellipsoidal variation and the semi-amplitude of this effect is predicted to be 2×10^{-4}. Cowan et al. (2012) found that there was no detectable ellipsoidal variation at 3.6 μm however the 4.5 μm data showed ellipsoidal variations that were six times greater than predicted for the planet. This provided another aim for the investigation, to determine if the detected ellipsoidal variation at 4.5 μm was indeed real or is caused by uncorrected

systematic noise in the data.

Table 4.1: Basic Parameters of the WASP-12 system. The Spitzer wavelength dependent data is taken from Cowan et al. (2012) with the equilibrium temperatures taken from Cowan & Agol (2011) and the other parameters taken from Chan et al. (2012). There are two measurements of the transit depth (one at each wavelength). The reason that these measurements differ is because they probe different regions of the atmosphere and this may be evidence of stratification of the atmosphere.

Parameter (unit)	**Value**
$(R_p/R_\star)^2$ 3.6 μm	0.0123 ± 0.0003
$(R_p/R_\star)^2$ 4.5 μm	0.0111 ± 0.0003
$F_p/F_\star$ 3.6 μm	0.0038 ± 0.0004
$F_p/F_\star$ 4.5 μm	0.0039 ± 0.0003
$(R_p/R_\star)^2$	0.1119 ± 0.0020
T_{eff} (K)	6300 ± 150
$M_\star$ ($M_\odot$)	1.36 ± 0.14
$R_\star$ ($R_\odot$)	1.595 ± 0.071
M_p ($M_{Jupiter}$)	1.403 ± 0.099
R_p ($R_{Jupiter}$)	1.732 ± 0.092
$a/R_\star$	3.105 ± 0.082
T_p substellar point (K)	3555 ± 132
T_p no-albedo, no-recirculation (K)	3213 ± 119
T_p no-albedo, full-recirculation (K)	2514 ± 92

4.2 Linear least squares fitting of the WASP-12 data set

4.2.1 Observations

The 3.6 μm (channel 1) and 4.5 μm (channel 2) Spitzer IRAC (Fazio et al. 2004) data used in this analysis are those described by Cowan et al. (2012). The observations

were conducted 2010 November 17-18 and 2010 December 11-12 for channel 1 and 2, respectively. The data were acquired in sub-array mode (32 × 32 pixels) with an exposure time of 2 seconds (effective exposure time of 1.92 seconds). The images are taken in blocks of 64 which are known as data cubes. The data in each channel spans one full orbit of WASP-12b (from just prior secondary eclipse to just after the following secondary eclipse). However, the 3.6 μm data ends shortly before the egress of the second occultation.

4.2.2 Data Reduction

To reduce the data I used the same method as Maxted et al. (2013), which I describe briefly here. First the Basic Calibrated Data (BCD) were converted from MJy/Steradian to mJy. This conversion was conducted using the pixel size at the centre of the subarray. These values were taken from the image headers. The values were 1.225×1.236 arcseconds^2 for channel 1, 1.205×1.228 arcseconds^2 for channel 2. To calculate the noise in each pixel, Poisson counting statistics in conjunction with the gain and readout noise for the individual channels was used.

The data is delivered in data cubes. Each data cube contains 64 images. To calculate the mid exposure time for each image, first the header keyword BMJD_OBS was used to assign a Barycentric UTC Modified Julian date (BMJD) to the start of the exposure for the first image in each of the data cubes and then the time taken to acquire all 64 images is calculated using the header keywords AINTBEG and ATIMEEND. Then a BMJD is assigned to each of the images in the data cube assuming that the images were uniformly spaced in time.

To remove outliers I carried out inspection on the images and found one bad pixel in each channel. These were excluded from the analysis. I also found from this inspection that a faint stellar source was observed to the north east of the target. I excluded these pixels from the analysis using a 3×4 pixel mask. A time series for each pixel in each data cube was then used to identify discrepant values. The reason for this is to exclude outliers that may affect the photometry. From this, pixels that deviate

by greater than 6σ are excluded.

To estimate the sky background all the pixels in each image are used except those within 10 pixels of the target position to prevent the wings of the PSF of the target biasing the result. A 4σ mean clipping is conducted to exclude outliers. A histogram of pixel values is then constructed and fit with a Gaussian to give an estimate of the standard deviation of the sky background (σ_{BG}). Approximately 700 points were used to estimate the sky background.

Three methods of stellar centroiding were used in the analysis of these data, two of which were the CNTRD and GCNTRD from the DAOPHOT package (Stetson 1987). The third, GAUSS2D, first creates a 7×7 sub-image which is centred on the nominal stellar position. Then a least squares fit of a bivariate Gaussian fit is conducted. It was found that the mean full width at half maximum (FWHM) in x and y for channels 1 and 2 were $x = 1.27, y = 1.15$ pixels and $x = 1.06, y = 1.25$ pixels. From this and for consistency the FWHM was fixed in both axes of the bivariate Gaussian in both channels to FWHM=1.25. Aperture photometry was then conducted using the IDL Astronomy Users library[1] implementation of the DAOPHOT APER procedure (Stetson 1987). 13 uniformly spaced aperture sizes from 1.5 to 4.5 pixels were used for this procedure.

4.2.3 Polynomial Detrending

The standard method to account for the IPSVs models the change in flux as a function of polynomials of the position of the PSF. These polynomials are normally linear or quadratic in both x and y. In this analysis the amplitude of the thermal phase variation and the offset of the hot spot from phase of 0.5 are the parameters that are of interest. For this reason the transit and eclipses are not included in the fit. Also the shape of the transits and eclipses is not a linear function of the parameters of the system so cannot be included in this linear least squares fit. The baseline of the observations and

[1] *http://idlastro.gsfc.nasa.gov/*

the period of the phase variation are comparable, hence, any correlations between the model of the IPSVs and the lightcurve must be understood so that they do not bias the conclusions.

The model that will be used in this analysis is given by equation 4.1.

$$\begin{aligned} m_i &= c_{0,0} + \sum_{j=1}^{N_{\cos}} a_j \cos(j\phi_i) + \sum_{k=1}^{N_{\sin}} b_k \sin(k\phi_i) \\ &\quad + \sum_{\iota=1}^{N_x} c_{\iota,0} p_\iota(x'_i) + \sum_{\kappa=1}^{N_y} c_{0,\kappa} p_\kappa(y'_i) \\ &\quad + \sum_{\lambda=1}^{N_{xy}} \sum_{\mu=1}^{N_{xy}} c_{\lambda,\mu} p_\lambda(x'_i) p_\mu(y'_i), \end{aligned} \tag{4.1}$$

where m_i is the magnitude of WASP-12 at time t_i; $\phi_i = 2\pi(t_i - T_0)/P$ is the orbital phase relative to the time of mid-transit, T_0; p_n is a Legendre polynomial of order n; $x'_i = (x_i - \bar{x})/(x_{\max} - x_{\min})$ and similarly for y'_i ($x_{\min}$ is the minimum value of x_i, etc.). The reason that Legendre polynomials are used rather than standard polynomials is because they are orthogonal between -1 and 1 hence, any correlations that occur between the model parameters will be significantly less than they would be if standard polynomials were used. The ephemeris of Cowan et al. (2012) is used throughout unless otherwise stated, where the authors only fit the data that is within 0.15 days of the transit, T_0 = BMJD 54508.4767 for the time of mid-transit and $P = 1.0914210$ days for the orbital period.

The regions of the detector where the star is situated out-of-transit/eclipse are used to decorrelate the whole data set. It is therefore very important to see if the decorrelation that is being conducted on the data in-transit/eclipse is being interpolated or extrapolated. If the IPSV correction is being interpolated then the decorrelation is reliable, assuming that in the region that is not mapped by the decorrelation there is no sudden violent changes in sensitivity. If extrapolation is being conducted then the results need to be treated with caution because the true sensitivity of the unmapped region is unknown. For the channel 1 data, for the decorrelation in x I found that the transit data is being interpolated, the first secondary eclipse is decorrelated using out-of-transit/eclipse data that samples the detector region but not very densely, and the second occultation is mostly in a mapped region of the detector but some extrapolation is also conducted. It is widely seen that the greatest effect of the IPSVs in *Spitzer* data

is due to the motion of the PSF in the y direction on the detector. I found that in the y direction the transit and first secondary eclipse are in a mapped region of parameter space but about $\sim$ 16% of the second occultation data is being extrapolated. This means that the region of the detector where these data lie are not mapped by the out-of-transit/eclipse data. To see what effect this had on the data I created a subset of the data in eclipse (excluding the ingress and egress of the eclipse), by selecting a region that is within 0.04 phase units[2] of 0.5 phase and measured the mean and standard deviation of the brightness of the system at these times. The mean brightness of the system for the first and second occultation are -3.1085 ± 0.0070 mags and -3.1074 ± 0.0067 mags. These values are consistent so even though some extrapolation is conducted to remove the IPSVs it has not has a major impact on the results.

For the channel 2 data the decorrelation in x, the transit and first occultation, the majority of the points are in regions of the detector which are mapped by the out-of-transit/eclipse data. There are some data of the second occultation which are in under sampled regions of the detector, but interpolation is conducted here because these regions lie between sampled areas. For the decorrelation in y the majority of the points in-transit/eclipse occupy regions of the detector that are sampled by the out-of-transit/eclipse data. However, some of the second occultation that are in a region on the detector that the out-of-transit/eclipse data under-samples. An example of a graph used to conduct this visual inspection is shown in Figure 4.1.

[2]the full width of the transit/eclipse is 0.06 phase units

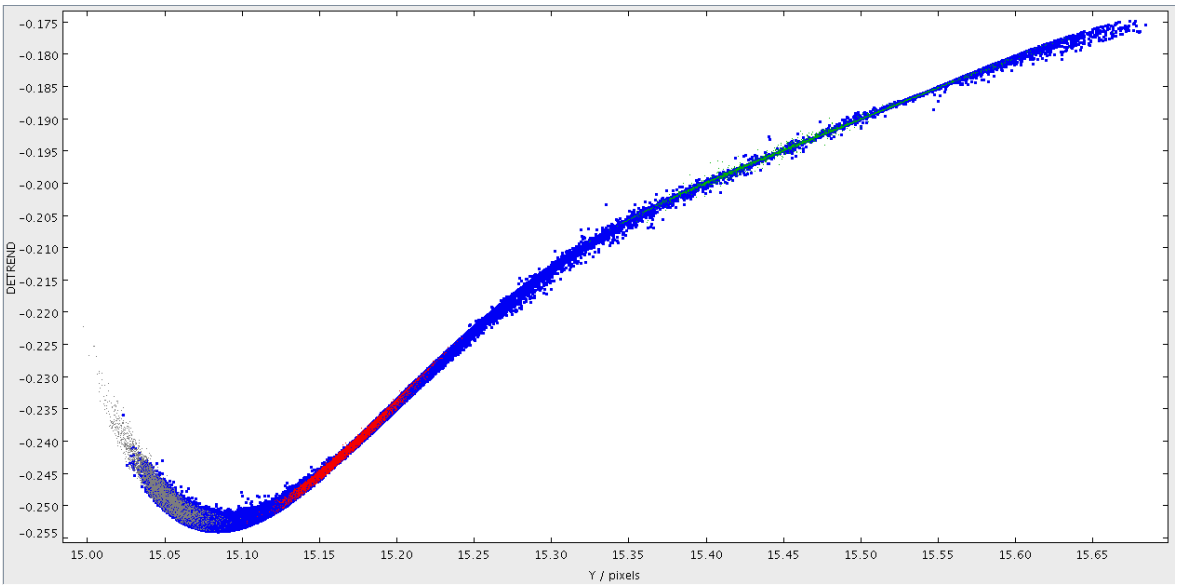

Figure 4.1: Example of a graph used to conduct this visual inspection, in this case it shows the value of the detrend against the y position . The blue points are the out-of-transit/eclipse data that is used for the decorrelation, the red points are the data in transit, the green points are the data from the first occultation and the grey points are those from the second occultation

4.2.4 Results and Discussion

I determined the optimal aperture to use by sorting all decorrelations by the RMS of the residuals and selecting the aperture with the lowest RMS. It was found that for channel 1 the best aperture to use was 2.0 pixels and for channel 2, 2.25 pixels. These were chosen because these extraction apertures gave the lowest RMS, 0.00668 for channel 1 and 0.00859 for channel 2. These values are comparable with the values of Cowan

et al. (2012). Then the Bayesian information criterion (BIC, equation 2.7) was used to find the smallest number of free parameters needed to fit the data without fitting the noise. This is done in equation 2.7 by penalising (increasing) χ^2. A more complicated detrending model (i.e one with higher order polynomials and hence more free parameters) is selected only if it decreases the χ^2 by $\geq N_{\rm par} \log_e(N)$ (Schwarz 1978). It was found that the optimum number of free parameters were $(N_{\cos}, N_{\sin}, N_x, N_y, N_{xy}) = (1, 2, 4, 8, 4)$ and $(N_{\cos}, N_{\sin}, N_x, N_y, N_{xy}) = (2, 2, 4, 8, 4)$ for channel 1 and 2 respectively. These results are seen in figure 4.2.

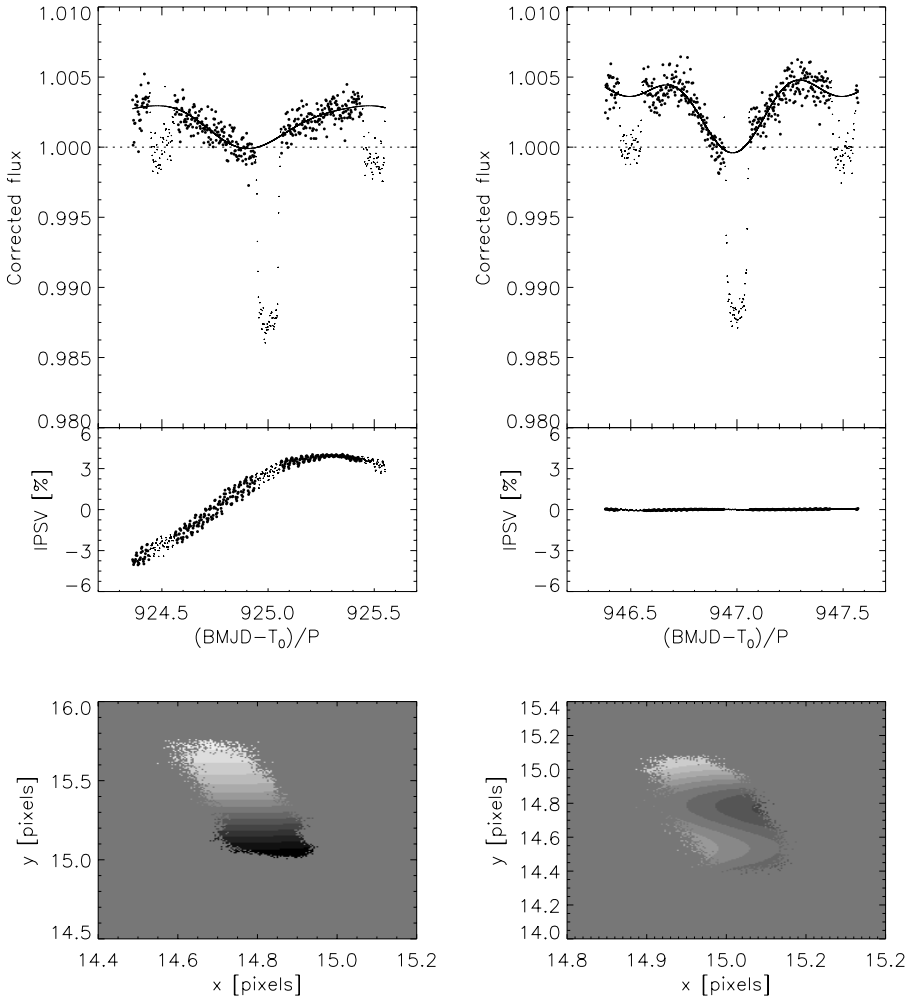

Figure 4.2: The flux of WASP-12 measured in IRAC channel 1 (left panel) and channel 2 (right panel) in an aperture of radii 2 and 2.25 pixels, respectively. After correction for intrapixel sensitivity variations (IPSVs) for the parameter sets $(N_{\cos}, N_{\sin}, N_x, N_y, N_{xy}) = (1, 2, 4, 8, 4)$ with positions measured using GCNTRD method and $(N_{\cos}, N_{\sin}, N_x, N_y, N_{xy}) = (2, 2, 4, 8, 4)$ with positions measured with the GAUSS2D method. Data are plotted averaged in 200 s bins for clarity and the best-fit sinusoidal model is also shown. The mean value in secondary eclipse is indicated with a dotted line. Note that data in eclipse (small points) are not included in the fit. The IPSVs model is shown as a function of time in the middle panels and as a function of position as a grey-scale plot in the lower panels. The grey-scale is linear between ±3.1 per cent for channel 1 and 0.2 per cent for channel 2 with positive values being white.

There are several features of both lightcurves that stand out in figure 4.2. In channel 1, the first feature that is apparent is the slope in the first secondary eclipse. The second feature is that the transit occurs after the minimum in the phase variation and also the transit is asymmetric (the ingress is lower than the egress). The third feature in the channel 1 light curve is that there is a slope in the transit as there is with the first secondary eclipse.

In channel 2 the first feature that is very obvious is the double maxima near quadrature. This feature could be the reason that Cowan et al. (2012) find a very large ellipsoidal variation at this wavelength. The second feature is the large gradient in flux from the flux maximum pre-transit to the ingress of transit. The accompanying feature that makes this even more interesting is that the gradient from the second maximum to the second eclipse is significantly smaller. A similar feature was seen by Swain et al. (2013), however, the authors thought of it as just a systematic error in the data and fitted it out. If it is a real feature, i.e., not instrumental systematic in nature, it may be astrophysical because two different telescopes observe, from different locations, a similar phenomenon at very different wavelengths. Another unusual feature of the data is the slight decrease in flux post egress of the first secondary eclipse. This could have astrophysical interpretations, e.g., a stream of material flowing from the planet to the host star if the planet is truly undergoing mass loss, but could also be noise/instrumental systematics.

The question that needs to be answered here is, are these features we see in the lightcurves real phenomena of the system or a result of systematic instrument errors? The first way to look at these is to ask if they are repeated in the data set. In channel 1 the slope in the first secondary eclipse is not repeated in the second occultation, however this could be because the data set ends prior to egress. There is only one transit in the data set it is not possible to test if the slope in the transit, the offset of the transit from the minimum in the phase variation, and the asymmetry of the transit are repeatable. In channel 2, the maximum is repeated on both sides of the orbit but the system needs to be re-observed to see if this feature is repeatable. It is not possible to determine if the dip in flux post egress of the first secondary eclipse is repeatable because there are

not enough data points post egress of the second occultation. A similar issue is the case to determine repeatability of the slopes into transit and secondary eclipse.

Another way to look at this is to see if the level at which these effects have been seen in other data sets. The level at which these effects occur is 0.01%. This is the level of unknown systematics that were seen in the WASP-18 lightcurve of Maxted et al. (2013).

A third way is to see how the model parameters vary with aperture. An advantage of the analysis method presented here is that the full covariance matrix is calculated so if there are any variations in the model parameters it is possible to determine if these are caused by correlations in the model. Figure 4.3 shows the dependency of the model parameters on aperture for the optimal decorrelation and figures 4.4, 4.5 show the correlations of the model parameters in channel 1 and 2 respectively.

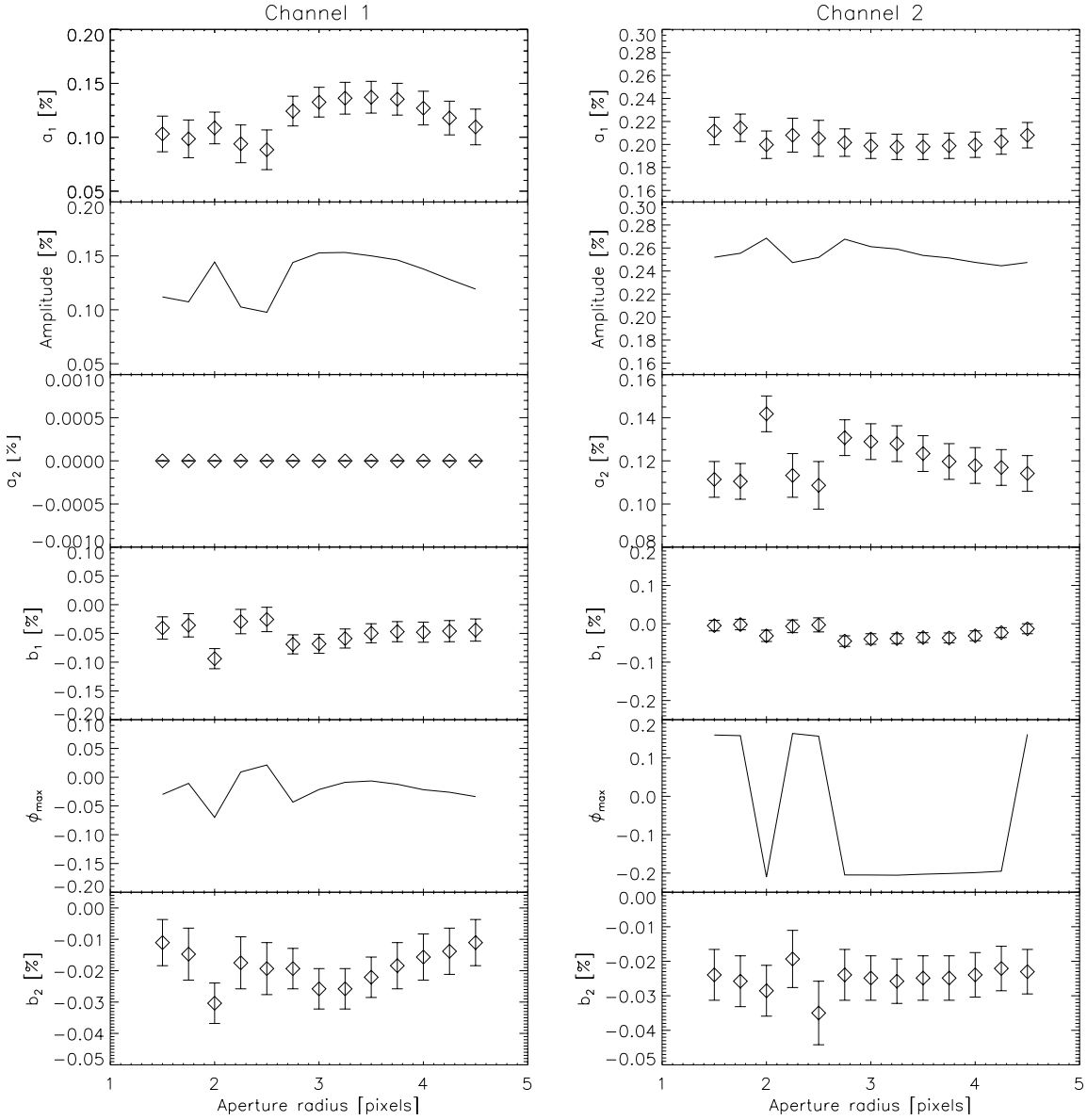

Figure 4.3: The dependency of model parameters on aperture for the optimal decorrelation for channel 1 (left) and channel 2 (right). The solid line in the upper panels shows the semi-amplitude of the phase variation. The solid line in the lower panel is the phase offset from phase 0.5 for time of maximum brightness for the thermal phase effect.

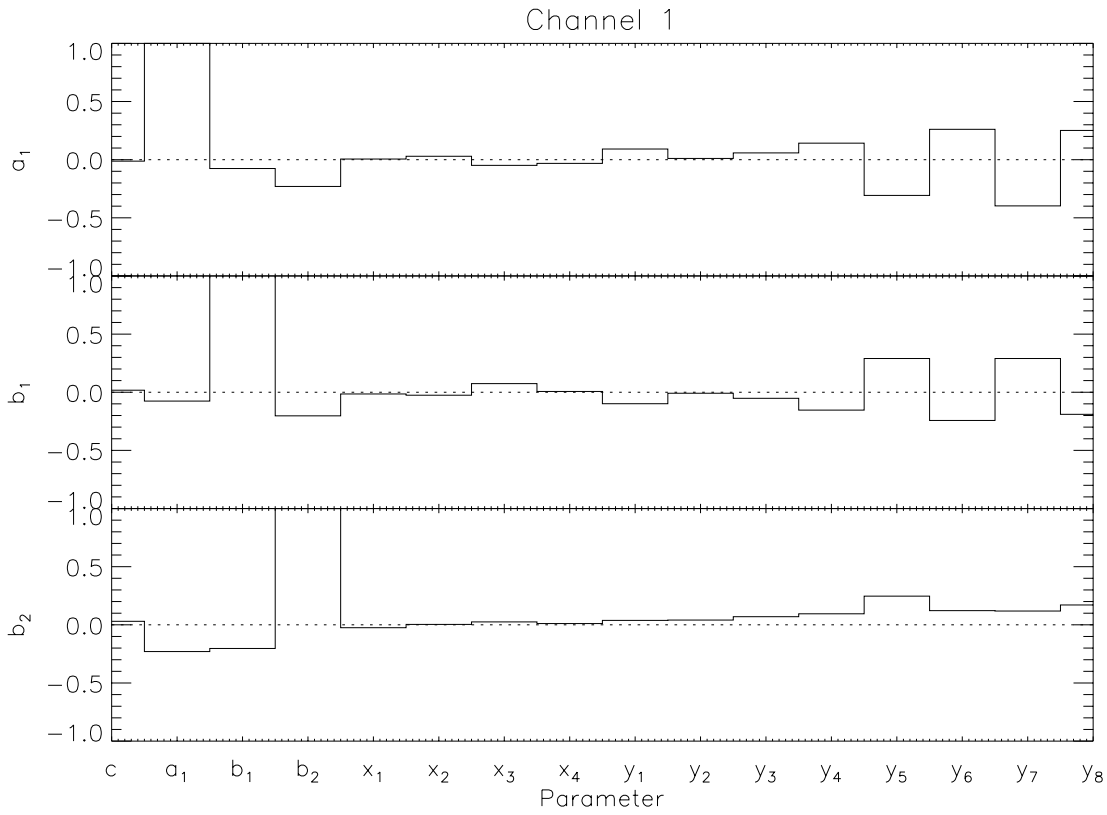

Figure 4.4: Correlations of model parameters for channel 1. The cross terms have been excluded from the plot as they have negligible correlation to the model parameters.

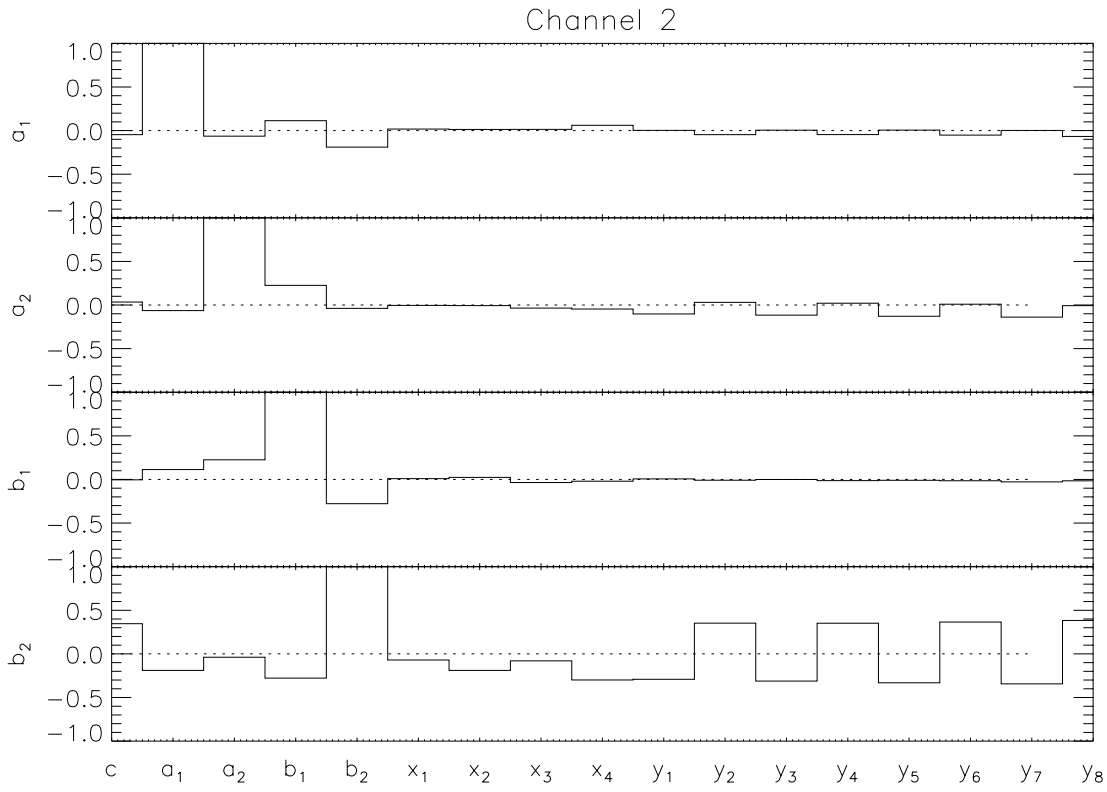

Figure 4.5: Correlations of model parameters for channel 2. The cross terms have been excluded from the plot as they have negligible correlation to the model parameters.

It can be clearly seen from Figure 4.3 that there are some trends in the model parameters. The cause of these are believed to be due to the strong correlations with the model parameters with the higher order y detrending polynomials (Figures 4.4, 4.5).

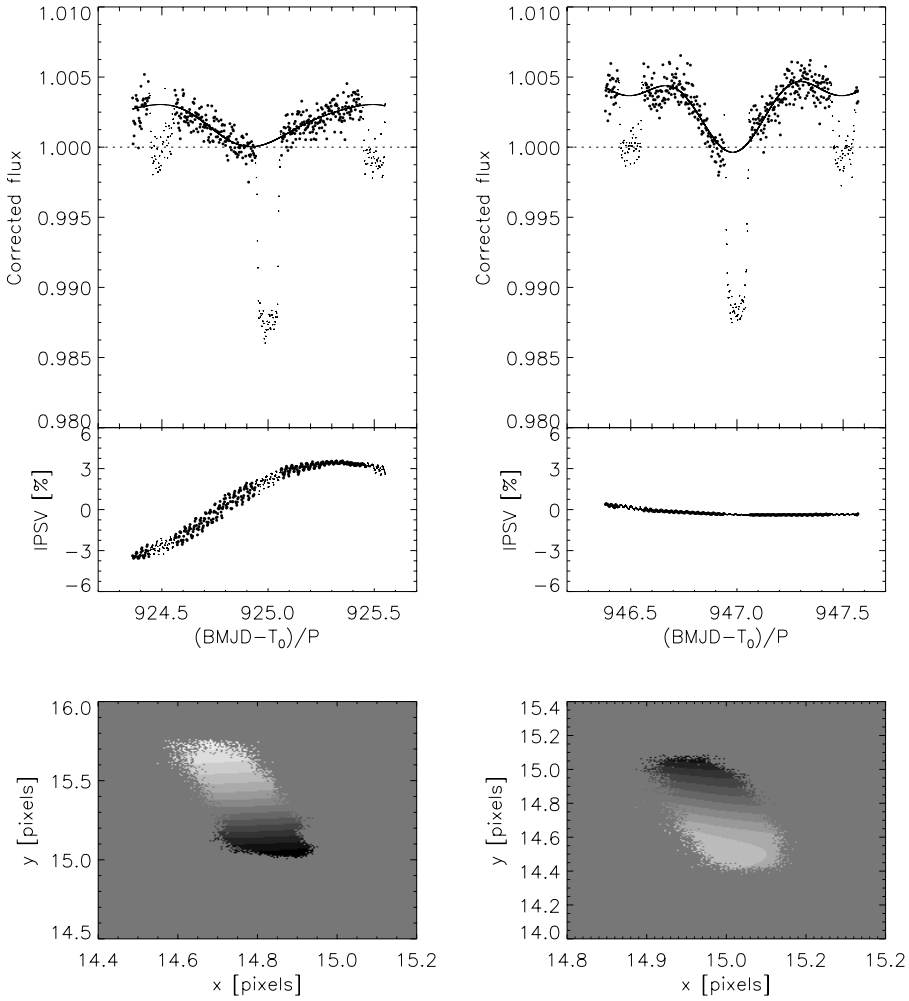

Figure 4.6: The flux of WASP-12 measured in IRAC channel 1 (left panel) and channel 2 (right panel) in an aperture of radii 2.5 and 2.75 pixels, respectively, after correction for intrapixel sensitivity variations (IPSVs) for the parameter sets $(N_{\cos}, N_{\sin}, N_x, N_y, N_{xy}) = (1, 2, 4, 8, 4)$ with positions measured using GCNTRD method and $(N_{\cos}, N_{\sin}, N_x, N_y, N_{xy}) = (2, 2, 4, 8, 4)$ with positions measured with the GAUSS2D method. Data are plotted averaged in 200 s bins for clarity and the best-fit sinusoidal model is also shown. The mean value in secondary eclipse is indicated with a dotted line. Note that data in eclipse (small points) are not included in the fit. The IPSVs model is shown as a function of time in the middle panels and as a function of position as a grey-scale plot in the lower panels. The grey-scale is linear between ±3.0 per cent for channel 1 and 0.4 per cent for channel 2 with positive values being white.

Figure 4.6 shows the lightcurve for slightly larger apertures (2.5 and 2.75 pixels for channel 1 and 2 respectively) but for the optimal decorrelation parameters. Although visually the differences are very subtle the results that come from these apertures are very different from the optimal apertures. The values of the parameters of interest are shown in table 4.2. The reason I chose to use these larger apertures is because they show clearly the large difference between the optimal aperture and non-optimal aperture. The cause of this significant difference is the large correlations between the model parameters and the higher order y Legendre polynomials coefficients.

Parameter	$3.6\,\mu$m		$4.5\,\mu$m	
	2 pixels	2.5 pixels	2.25 pixels	2.75 pixels
A[%]	0.144 ± 0.014	0.098 ± 0.018	0.247 ± 0.014	0.27 ± 0.01
$\phi_{\max}$ ($^\circ$)	-25 ± 23	8 ± 18	59 ± 56	-74 ± 25

Table 4.2: Comparison of parameters for the optimal and non optimal apertures in channel 1 and channel 2. The optimal aperture for channel 1 is 2 pixels and for channel 2 is 2.25 pixels. The large difference in the parameters is attributed to the strong correlations with the model parameters and the higher order y Legendre polynomials terms.

Even though there are subtle differences between figures 4.2 and 4.6 these make a significant difference to the parameters of interest, in this case the phase offset of maximum brightness and the amplitude of the phase variation. The reason for this is that the light curve in the region of the secondary eclipse is very flat so small differences in the model parameters can propagate through to large variations in the parameters of interest. The amplitudes and phases given in Table 4.2 were calculated by evaluating equation 4.1 over a regular grid of 65536 phase points from 0 to 1, and repeating the calculation for 1000 sets of coefficients taken from the MCMC chain. The values and errors in Table 4.2 are the means and standard deviations of the amplitudes and phase of maximum light calculated from these 1000 trials.

4.2.5 Comparison to Cowan et al. (2012)

Table 4.3 compares the results from this work and those of Cowan et al. (2012). These results show that the result of Cowan et al. (2012) are not repeatable. This is because there is not enough data to determine the source of the systematic errors present in the data set. Multiple observations can be combined to determine the origins of these systematic errors. If they are intrinsic to the system then they will repeat and be seen in future observations and if they are noise then they will not repeat. Overall, the main discrepancy between the two analyses is the uncertainties on the parameter values. My conclusion from this work is that the results of Cowan et al. (2012) may be consistent with the data, but, just that the uncertainties are underestimated. This means that there are additional fits to those of Cowan et al. (2012)that are a good fit to the data.

Parameter	$3.6\,\mu$m		$4.5\,\mu$m	
	This work	Cowan et al. (2012)	This work	Cowan et al. (2012)
A[%]	0.144 ± 0.014	0.19 ± 0.03	0.247 ± 0.014	0.20 ± 0.02
$\phi_{\max}$ (°)	-25 ± 23	-53 ± 7	59 ± 56	-74 ± 25

Table 4.3: Comparison of parameter of interest in this investigation to that of Cowan et al. (2012). A is the amplitude of the phase variation expressed as a percentage and $\phi_{\max}$ is the offset, in degrees, of the hotspot on the planet.

4.3 Conclusions

This analysis has shown that the method of Maxted et al. (2013) is a good method because it, in an unbiased way, shows the features (noise or astrophysical in nature) that are present in the data. The method uses a simple mathematical model and a linear least squares fitting routine to fit the lightcurve. The advantages of this method are that it is very fast, there is no imposed prior which could bias the interpretations of the results and the full covariance matrix is calculated. The covariance matrix is very useful as it shows any degeneracies in the model. We find that for this data set,

we are unable to reproduce the results of Cowan et al. (2012) because there are some severe correlations between the model parameters and the high order coefficients of the Legendre polynomials used to model the IPSVs. The system is currently being re-observed using the new "peak-up" mode. This mode will reacquire the target every 10 hours which will reduce the issue of the large y drift. These new observations will also show if the features seen in these lightcurves are repeatable.

5 Semi-Synthetic Secondary Eclipse Lightcurves of WASP-35b

5.1 Introduction

As was seen in the previous chapter, the systematic errors (both of known and unknown origin) in *Spitzer* data of hot Jupiters are the limiting factor in extracting the most information out of the data. The goal of this chapter is to understand to what extent observations of secondary eclipses are affected by the *Spitzer* systematic errors. More specifically the effect of these systematics on the measured time of mid-eclipse, the eclipse depth and the effect on their uncertainties. It is very important to calculate reliable uncertainties on these measurements, as underestimating the uncertainties will overestimate the significance of the results and overestimating the uncertainties leads to real features in the data being missed. Observing the secondary eclipse at different wavelengths probes different regions of the atmosphere of the exoplanet. The eclipse depth at a particular wavelength gives information about the temperature of the atmosphere at the depth probed by that wavelength. The time of mid-eclipse constrains the eccentricity of the planet and gives information of an offset from the substellar point of the hotspot on the planet. Any systematic error in either of these parameters could affect the interpretation of the derived quantities. I conduct my analysis by injecting eclipses into real *Spitzer* data and using various methods to recover the eclipse depth and the time of mid-eclipse. Ideally, a *Spitzer* observation of a non-planet hosting star on the time-scale of a secondary eclipse observation would be required. However, *Spitzer* exoplanet observations with another star in the same field as the target are very rare. Initially, I was going to use the portions of data between the transit and eclipse of the WASP-12b data set. However, there may be underlying signal, e.g., a tidal stream of material being stripped from the planet which, in conjunction with the systematic errors are causing the issues seen in the previous chapter. Instead, the full orbit observations of HAT-P-2b (Lewis et al. 2013) at 3.6 μm and 4.5 μm were chosen.

The analysis of Lewis et al. (2013) also contain partial orbit observations at 5.8 μm and 8 μm, but I do not use these data in my analysis. The planet is on a very eccentric orbit ($e = 0.5$) with a 5.6 day period. I injected an eclipse into the data between the first secondary eclipse and the transit ($\sim$ 50 hours). This portion of data should be almost flat because the planet will contribute very little to the system flux during this time. The results of this analysis will be used in the next chapter in which I present the first analysis of the secondary eclipse of WASP-35b.

5.1.1 Noise

The simplest noise that is present in astrophysical data is white noise. It has some very useful properties, firstly that the data points are independent i.e. they are uncorrelated. Secondly the data are Gaussian distributed which means there are many well known mathematical expressions that can be used to calculate the uncertainties on model parameters. Thirdly, the RMS of the data is constant across a singe data set and repeat data sets, this is a very useful property for exoplanet transits and secondary eclipse because it means that we are able to use the out-of-transit data to look for features in transit. If there is correlated noise, e.g., Pont, Zucker & Queloz (2006), it may be such that the data points are correlated which means that it can be hard to distinguish real signal from correlated noise in the data. If the data are not Gaussian distributed then the relations for confidence intervals cannot be used. Finally if the RMS is not constant through individual and repeat data sets then comparing signal in-and-out of eclipse, for example, may not be justifiable.

5.2 Method

This analysis is being used as preliminary test of the signal injection method which is to be used on the WASP-35 secondary eclipse data. First a prediction of the eclipse depth of WASP-35b was required. The Transiting ExoPlanet CATalogue (TEPCAT)

of Southworth (2011a) was used to find a similar planetary system to WASP-35, with a measured eclipse depth using *Spitzer*. The system that was found to be most similar is HD209458. The eclipse depth of HD209458 at $3.6\,\mu$m and $4.5\,\mu$m are shown in Table 5.1 (Knutson et al. 2008).

Wavelength	Eclipse Depth
$3.6\,\mu$m	0.00094 ± 0.00009
$4.5\,\mu$m	0.00213 ± 0.00015

Table 5.1: Eclipse depths of HD209458

The data in Table 5.1 was used together with the WASP-35 system parameters, taken from Enoch et al. (2011), to simulate the eclipse of WASP-35 at both $3.6\,\mu$m and $4.5\,\mu$m using the equations of Mandel & Agol (2002) to calculate the loss of flux due to the eclipse with zero limb darkening.

Two methods of recovery were used in this analysis, the standard polynomial fitting as used in Mahtani et al. (2013) and the new implementation of wavelet fitting as described in Chapter 2.4. It has been suggested that the wavelet fitting method gives more reliable results in the case that the data contains $\frac{1}{f}$ (red) noise (Carter & Winn 2009). The lightcurve model used in this analysis is that of Mandel & Agol (2002) with zero limb darkening. The free system parameters are parametrised such that they only range from 0 to 1 so that the values stay within a physical range (equations 5.1, 5.2, 5.3, 5.4).

$$\mathrm{pr}_\star = 0.5 \ln\left(\frac{r_\star}{1-r_\star}\right), r_\star = \frac{R_\star}{a} \tag{5.1}$$

$$\mathrm{pk} = 0.5 \ln\left(\frac{k}{1-k}\right), k = \frac{R_{\mathrm{planet}}}{R_\star} \tag{5.2}$$

$$\mathrm{pb} = 0.5 \ln \frac{b}{1-b}, b = \text{impact parameter} \tag{5.3}$$

$$\mathrm{depth} = \text{fractional depth of eclipse} \tag{5.4}$$

Initially a simplex algorithm (Press et al. 1992) is used to optimise these input parameters with detrending done as a linear least squares fitting to residuals for each trial set of parameters. These best fit parameters are used as the starting point for a second simplex algorithm which conducts a simultaneous optimisation of the lightcurve and detrending parameters. For the wavelet fitting, the residuals from the fit to the lightcurve and detrending models are fit with wavelets to estimate the amount of red (σ_r) and white (σ_w) noise present in the data. 10,000 lightcurve simulations were conducted for each set of polynomial detrending parameters (Table 5.2).

Run	**Order of X polynomial**	**Order of Y polynomial**	**Order of Time polynomial**
1	1	1	0
2	1	1	1
3	1	1	2
4	1	2	0
5	1	2	1
6	1	2	2
7	2	1	0
8	2	1	1
9	2	1	2
10	2	2	0
11	2	2	1
12	2	2	2

Table 5.2: Order of polynomials used for decorrelation

For each simulated lightcurve the parameters that are calculated are :

1. The difference between the input depth and that found by both the polynomial and wavelet fitting methods.

2. The difference between the input time-of-mid-eclipse and that found by both polynomial and wavelet methods.

3. The RMS of the residuals from both the polynomial and wavelet methods.

4. The amount of red (σ_r) and white (σ_w) noise (wavelet fitting only).

5. The BIC for each fit for both the polynomial and wavelet methods.

Each synthetic eclipse spans a similar length of time to a standard *Spitzer* secondary eclipse observation ($\sim$ 7 hours). The length of the HAT-P-2 data set that is used for the injection is long enough ($\sim$ 50 hours) such that many independent data sets can be created. For each set of polynomial detrending parameters a distribution of the calculated parameters listed above is produced. For each parameter I use the mean and standard deviation for parameter and uncertainty estimation respectively. Initially I used segments of binned data 2048 data points[1], in length. This however caused variable data set lengths in time due to empty bins. So instead I use 4096 data points and interpolated if any bins were empty. This provides uniform temporal sampling, which is required for the application of wavelet fitting. Figure 5.1 shows an example of a semi-synthetic light curve generated and the wavelet fit to the data.

[1]the wavelet fitting requires 2^n data points, when n is an integer

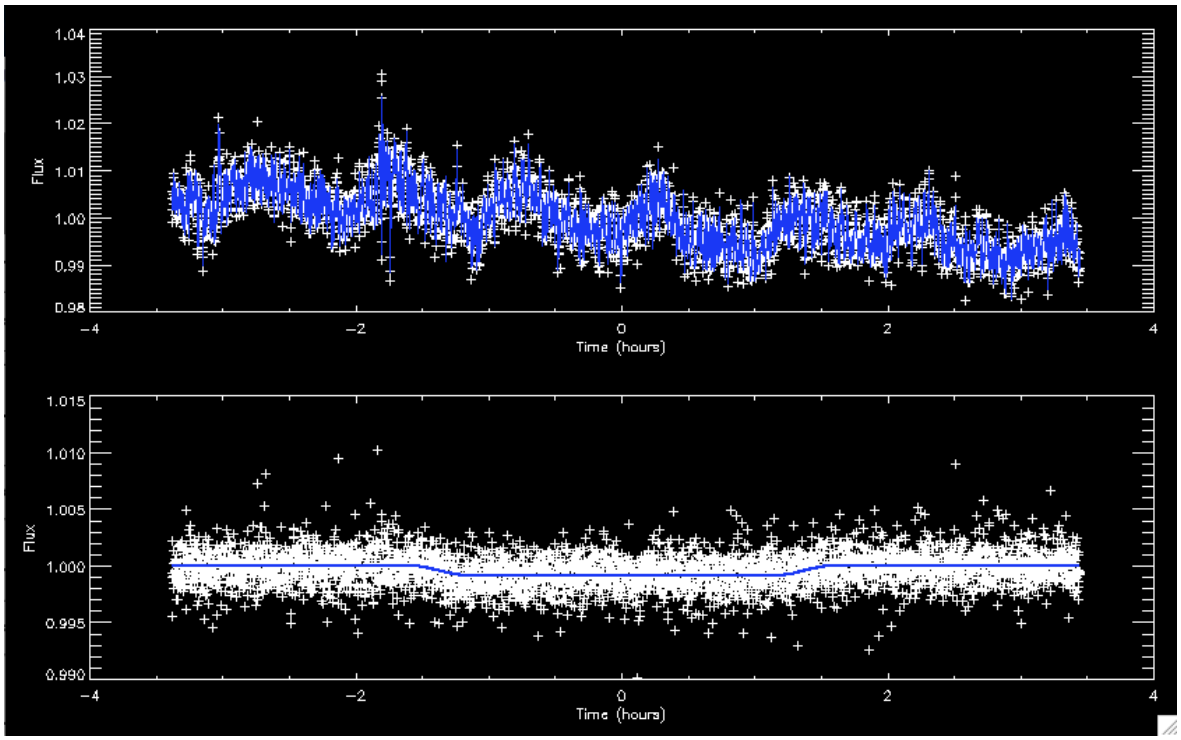

Figure 5.1: Example of a channel 1 semi-synthetic lightcurve produced and fit by this method. The white points are the data and the blue line is the wavelet fit to the data. The upper panel is the raw lightcurve and the lower panel is the detrended light curve.

The mid point of the eclipse in each semi-synthetic lightcurve is varied randomly by 0.005 days around the mid point of the data train. 10 randomly selected semi-synthetic lightcurves were then analysed with the MCMC (using the same algorithm as described in chapter 3.4.1) and the results from this were compared to the polynomial and wavelet fitting. For the polynomial fitting I used the polynomials shown in Table 5.2 to account for the IPSVs and recover of the eclipse parameters using the methods of Mandel & Agol (2002). Higher order polynomials have been used previously for longer base line observations, e.g., thermal phase curves, however for single eclipse observations the highest order normally used is a quadratic. The reason for this is that using a time trend can fit and remove some of the true eclipse signal

To make sure that the parameters that these fitting methods produced were accurate I tested their reliability by comparing the results from MCMC fit of the 10 synthetic lightcurves to that of the polynomial/wavelet fitting. I did this by taking the difference between the polynomial/wavelet fit results and those of the MCMC. The mean and the standard deviation of these difference for the depth and time of mid-eclipse is shown in Table 5.3. It can be seen that the differences between the polynomial/wavelets and MCMC results are consistent with zero for the channel 1 data but only the times of mid-eclipse for the channel 2 data are not consistent. The slight discrepancy for the channel 2 depths are negligible relative to the error bar on this parameter.

	3.6 μm				4.5 μm			
	Depth (ppm)		Tmid(s)		Depth(ppm)		Tmid(s)	
	Poly	Wave	Poly	Wave	Poly	Wave	Poly	Wave
Mean	-7.72	-6.58	-0.54	-31.83	-31.48	23.31	5.20	10.92
SD	18.52	20.15	16.28	32.07	12.05	13.85	16.57	19.91

Table 5.3: Comparison between the wavelet and polynomial fitting

5.3 Channel 1 results

Figure 5.2 shows the results of the channel 1 simulations. These results are showing how well, given 10,000 realisations of the secondary eclipse lightcurve, the methods used here recover the time-of-mid-eclipse and the depth of the eclipse. The first point to make is that both the wavelet fits and the polynomial fits give consistent results for the time-of-mid-eclipse and the depth. What this means is that nothing is gained from using the more complicated wavelet fitting code. This is good because the polynomial fitting method is the standard fitting method for removing the IPSVs in *Spitzer* data. It is also very well tested and understood. Also the wavelet fitting method is more difficult to code.

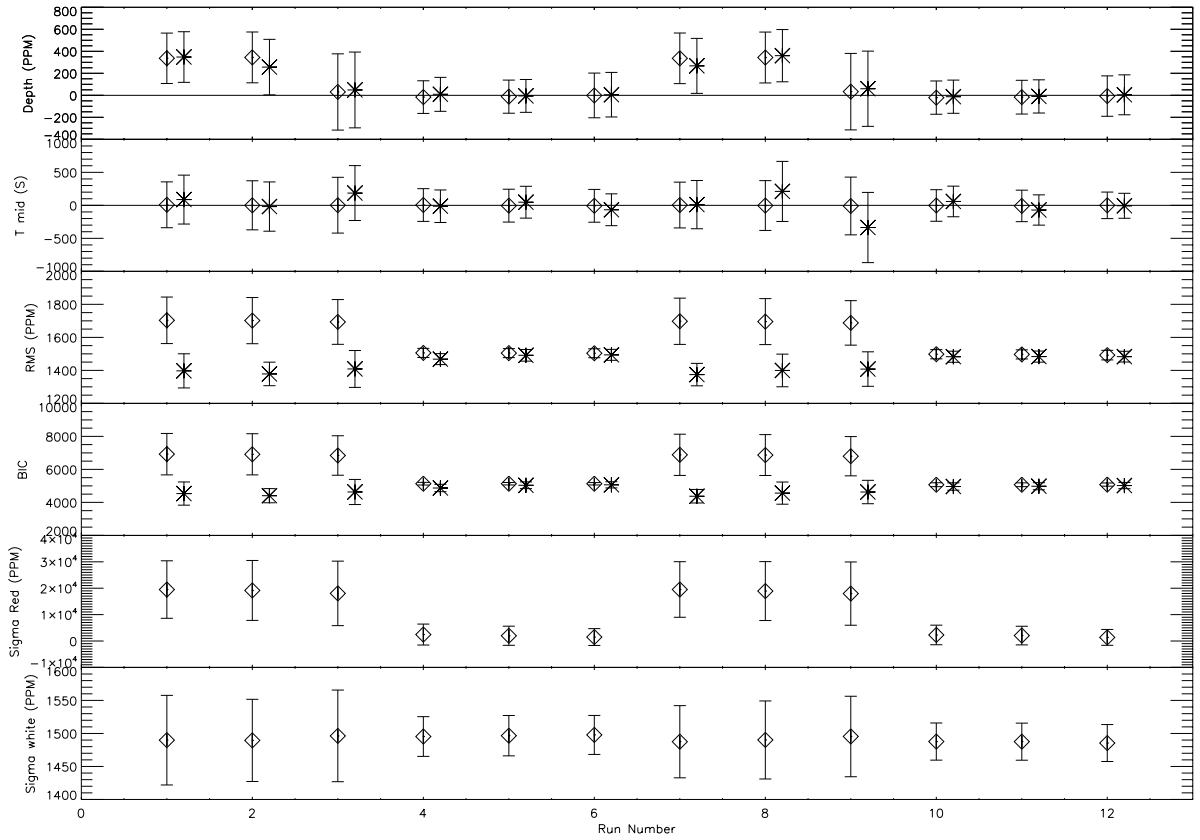

Figure 5.2: The means and standard deviations of the depth, time of mid-eclipse, RMS and the BIC for the initial channel 1 results. The diamonds are the polynomial fitting results and the stars are the wavelet fitting results. The polynomial and wavelet fits have been off set by 0.2 for clarity only. The run numbers correspond to those in Table 5.2. The solid black lines in the first two plots are at 0 to show those decorrelation methods that are biased.

From the top panel of Figure 5.2 it can be seen that when a linear y and no time or linear time decorrelation is used there is a (positive) bias in the recovered depths. This means is that the code is finding the depth of the eclipse to be larger than it should be. This is acceptable because the standard polynomial used for channel 1 occultation observations is quadratic y and not linear y. This is because it almost always reduces the BIC. This is also seen here in the fourth plot down in figure 5.2.

It may be possible, however, given the scatter (error bars) that one may find a lower BIC value but have an eclipse depth that is 1 or more sigma away from its true value. From the results of run 1 (linear x, linear y and no time trends) I selected the points (for both the polynomials and wavelet methods) where the BIC was less than (or equal to) the mean BIC and the difference in depth (from the input depth) was greater than (or equal to) one standard deviation of the depth distribution. I found that for the polynomial that this occurred 29% of the time. This is about right because 1σ incorporates 68.3% of the data, which means that 31.7% of the time the difference in depth should be out by 1σ or more. This result shows that the 1σ confidence interval for the depth is slightly overestimated but about correct. The same was done for the wavelet fitting method and I found that 51% of the time one can have a lower BIC (compared to the mean) but have a depth that is off by 1σ or more. This shows that the one sigma confidence interval for the depth is significantly underestimated and further evidence to suggest that wavelet fitting does not improve on polynomial decorrelation when fitting channel 1 *Spitzer* data. It should be noted here that the BIC quoted here for the wavelet fitting is more of a pseudo-BIC because wavelet fitting does not give a χ^2 but instead gives a log(likelihood) which is then converted to a pseudo-χ^2 to calculate the pseudo-BIC. This could be part of the reason that the wavelet BICs are lower than the polynomial BICs for the linear y decorrelation but consistent with the polynomials when a quadratic time trend is used. Also, the large amount of red noise fit with the linear y decorrelation is due the real quadratic y trend being fit as red noise. When a quadratic y trend is fit, it can be that the amount of red noise decreases to what is most likely the true amount of red noise in the data.

It can also be seen from the top plot of figure 5.2 that fitting the data with linear

y and quadratic time does remove the bias in the results but in doing so it does increase the scatter (larger error bars). The reason for this is that the quadratic time trend is trying to fit the quadratic y trend. The error bars are only slightly larger when quadratic time trend is added over linear time trend when fitting with a quadratic y trend as can be seen by comparing runs 5 and 6 (also 11 and 12). So not only is linear y a bad decorrelation choice but quadratic time in conjunction does not improve results. Looking at the results which have quadratic y fitted (runs 4,5,6 and 10,11,12) it can be seen that there is no bias in the eclipse depth. This is very reassuring because the standard decorrelation for channel 1 *Spitzer* data uses quadratic y. Also, smaller error bars on depth for these runs is further justification for quadratic y. Smaller error bars means that the code more often gives results close to the true value of the eclipse depth. For the time of mid-eclipse the runs that use quadratic y in the decorrelation shows very little bias, and in fact all methods of decorrelation have very little bias but those with linear y do have larger error bars (larger scatter). This is again further justification for the use of the quadratic y term in the decorrelation.

The RMS is normally used to determine the optimal aperture; this is done by fitting a fixed polynomial decorrelation to all apertures used for the photometry (conducted in a similar manner to Mahtani et al. 2013, see chapter 3) and then choosing the aperture with the lowest RMS. From the RMS plot it can be seen that very consistent values are found for runs using quadratic y decorrelation. Hence the polynomial used for this procedure should be a quadratic y. The x and time polynomial can be seen to make no significant difference to the quality of the fits (i.e., the RMS) so if possible the simplest decorrelation should be used. In the MCMC that my collaborators and I use, the same x and y decorrelation must be used. The conclusion for this is that a good decorrelation for this procedure is quadratic polynomials for the spacial component and none or linear polynomials for the temporal component. This is the method I used for my analysis of WASP-26b (Mahtani et al. 2013) (see chapter 3).

5.4 Channel 2 results

Figure 5.3 shows the results of the channel 2 signal injection. The most important result from this is that the depths and times of mid-eclipse are consistent regardless of the polynomials used for the decorrelation. This is also seen from the fact that the BICs for all polynomials used are all consistent. The consistency between the polynomial and wavelet results indicate that there is no reason to use the more complicated wavelet fitting on this channel 2 data. This is very good because the polynomial method is better understood and easy to implement. It is interesting to note that the red noise scatter (σ_r) is minimised when a quadratic y trend and some time trend are used for the decorrelation. This suggests that there may be some quadratic trend in the data and that this is being fit by the quadratic y trend. This requires further investigation which is beyond the scope of this work. The conclusion that comes from this is that even if a more complicated model (than is required) is used it will not affect the depth and time of mid-eclipse. This is very important because from these two parameters temperature, molecules in the atmosphere and eccentricity are concluded.

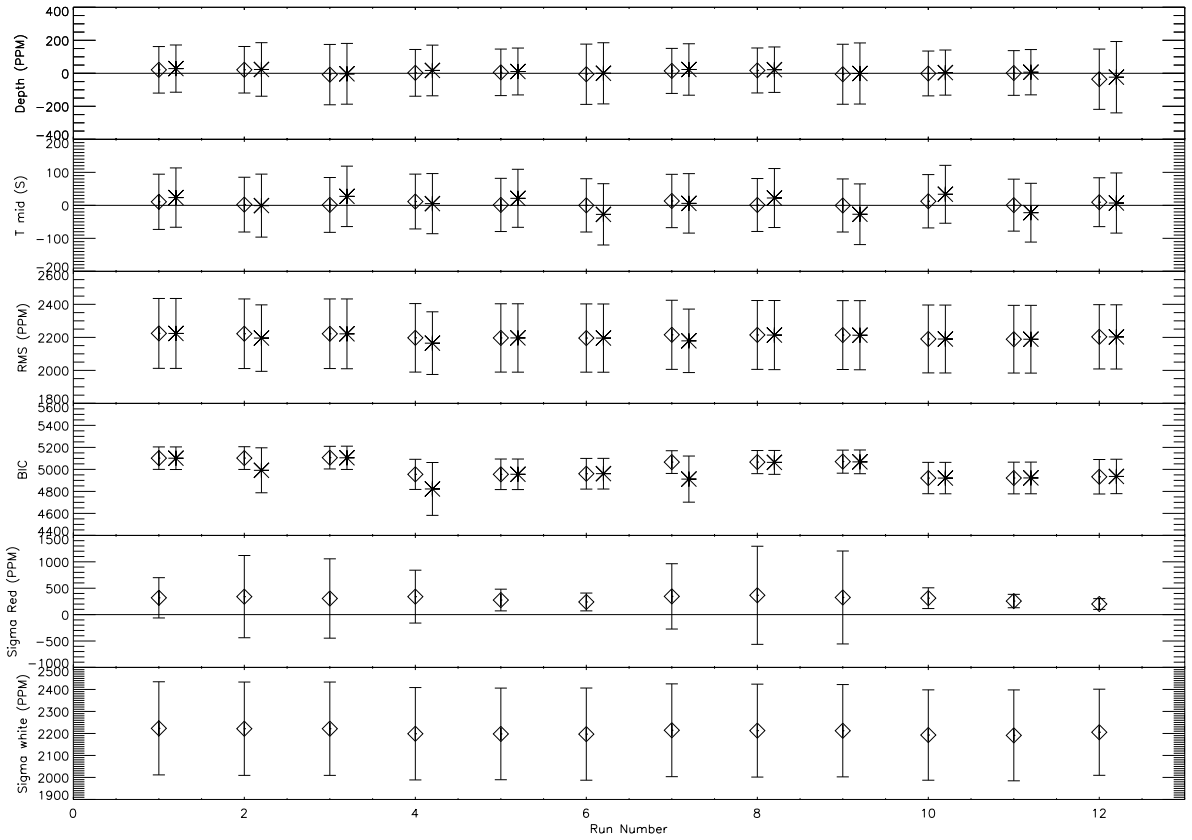

Figure 5.3: The means and standard deviations of the depth, time of mid-eclipse, RMS and the BIC for the initial channel 2 results. The diamonds are the polynomial fitting results and the stars are the wavelet fitting results. The polynomial and wavelet fits have been off set by 0.2 for clarity only. The run numbers correspond to those in Table 5.2. The solid black lines in the first two plots are at 0 to show those decorrelation methods that are biased.

5.5 MCMC comparison

10 synthetic lightcurves from each channel were then fit using the MCMC algorithm I used in the analysis of WASP-26b (Mahtani et al. 2013), to see how well the MCMC algorithm recovered the synthetic eclipses. I then compare the results from the MCMC to that of the polynomial and wavelet fitting to see how the agreement between all the results and also to see how well the MCMC algorithm recovers the true value of the eclipse. Figure 5.4 compares the recovered parameters using all three of the methods presented in this thesis. It can be seen that all the methods are consistent with each other which adds credence to the result that the wavelet method is not useful in this particular analysis. However, it can also be seen that several of the results are significantly discrepant.

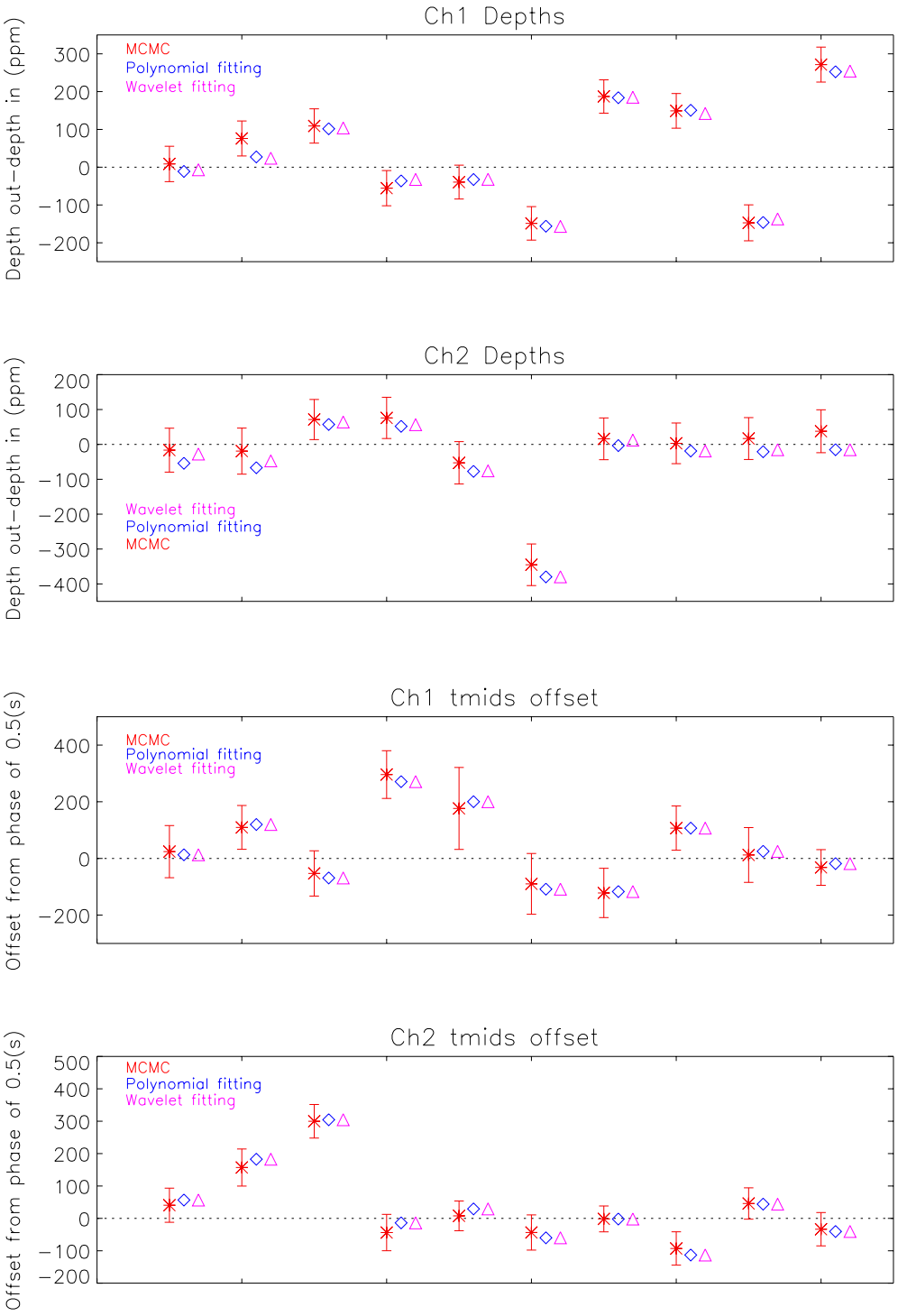

Figure 5.4: Comparison of recovered parameters using polynomial, wavelets and MCMC

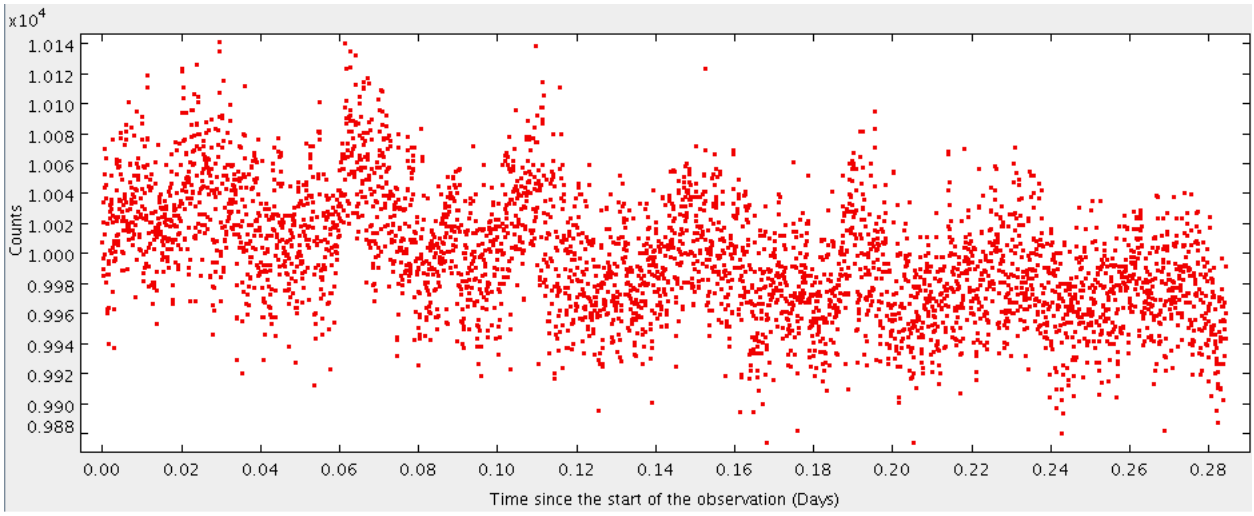

Figure 5.5: Last channel 1 simulated lightcurve. This shows that these lightcurves look very similar to the real channel 1 lightcurve (e.g. Mahtani et al. 2013) and so it is unlikely that the cause of the significant discrepancies seen in these results is down to poor lightcurve simulation.

For example the tenth simulation of the channel 1 (Figure 5.5) data and the sixth simulation for the channel 2 data show the depths are discrepant by $\sim 6\sigma$.[2] For the times of mid-eclipse the fourth simulation is off by $\sim 3.5\sigma$ and the third simulation is off by $\sim 6\sigma$ for channel 1 and 2 respectively. This is unexpected if the distribution of the MCMC recovered parameters is Gaussian, the chances of getting a result that is more than 3σ away from the mean (which in this case should be 0) is 0.27% which means error bars are not estimated correctly.

Figure 5.6 compares the MCMC distributions of the parameters recovered from the simulated lightcurves with the overall distributions of the parameters from the polynomial method. The polynomial distribution (blue curves) are the true distributions of the recovered parameters given multiple realisations of the lightcurves, i.e., repeating the observation 10,000 times. The green curves are the MCMC distributions

[2]Here the sigma is the average error of the MCMC recovered parameter

of the parameters and they are an estimate of the polynomial distribution (blue curves) given only one realisation of the lightcurve. The red curves are Gaussian distributions with the same standard deviation as the polynomials distribution and mean 0 for the parameters. It can be seen that the polynomial distributions are non-Gaussian because there are significant differences between the blue curves and the red curves. The MCMC distributions are not only biased but are also highly peaked with heavy tails. The goal of this work is to find a method to inflate the error bars on individual secondary eclipse depths such that they are more reliable. The polynomial and MCMC distributions are such that the shapes cannot be matched, however, the widths can be matched. To do this, for both channels and both the depths and mid-eclipse times, I measured the standard deviation of the polynomial distributions for each parameter and the mean MCMC error bar of all 10 simulated lightcurves. For each parameter, I added a value (in quadrature) to the mean error bar of the 10 simulated lightcurves such that this was equal to the standard deviation of the polynomial distribution. The values that needed to be added to the MCMC error bars are shown in Table 5.4.

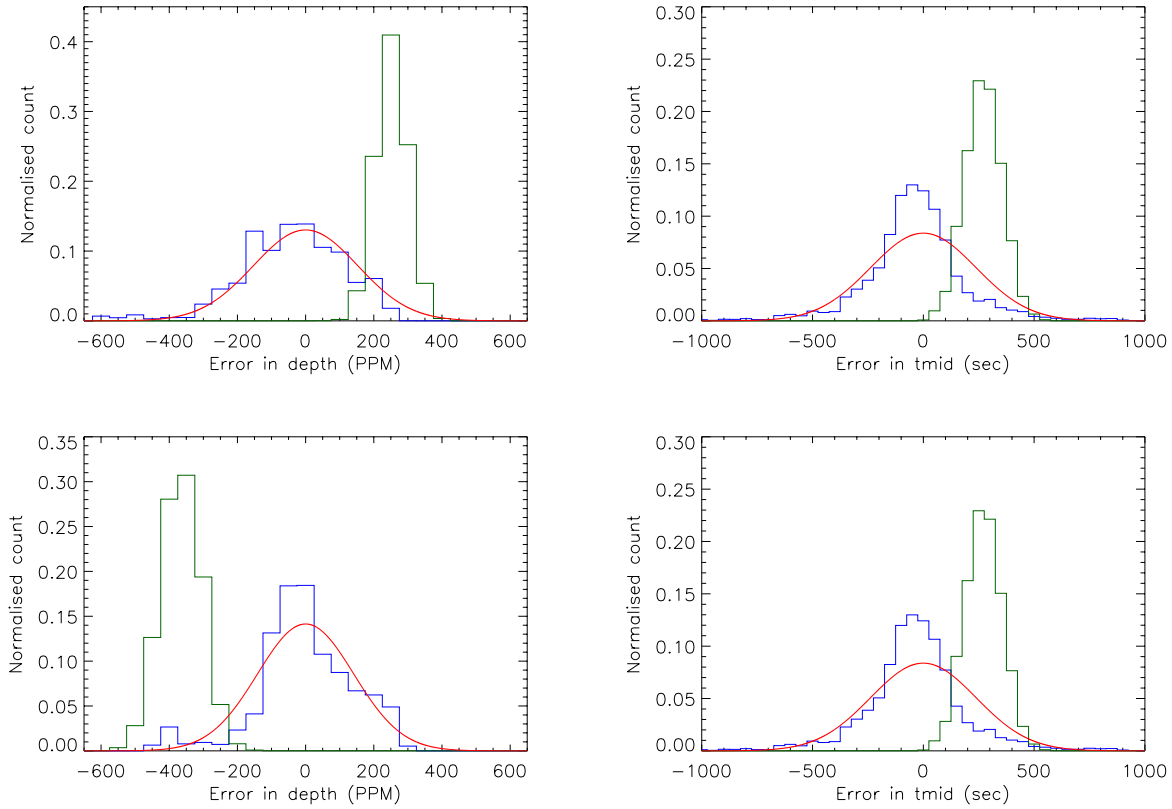

Figure 5.6: Comparison of the distributions of the two parameters of interest. The MCMC distributions shown are for the depths are the tenth simulation of the channel 1 data and the sixth simulation for the channel 2 data (green lines). The decorrelation polynomials that were used are quadratic-in-space, linear-in-time for channel 1 and was linear-in-space, no-time . The polynomial distribution for these are shown in blue. The red lines are a Gaussian distribution with the same standard deviation as the polynomial distribution and mean 0.

Wavelength	Eclipse error (PPM)	Time of mid-eclipse error (s)
3.6 μm	146	220
4.5 μm	127	67

Table 5.4: The extra amount of error that was required to inflate the error bars on the simulated WASP-35 lightcurves

5.6 Conclusions

In this chapter I have presented a method of determining realistic error bars for two parameters that come from secondary eclipse photometry, the depth of the eclipse and the time of mid-eclipse. These are very important parameters to have reliable error bars because they give the temperature of the atmosphere at the altitude probed, evidence of molecules and constraints on the eccentricity of the planets orbit. To do this I have simulated eclipses of WASP-35b using the phase curve of HAT-P-2b. However, WASP-35 and HAT-P-2 have V-band magnitudes of 10.94 and 8.69, respectively. To accurately simulate secondary eclipses of WASP-35b extra white noise needs to be added to the HAT-P-2 data. In the next chapter I re-do this analysis adding in the extra white noise to account for the difference in brightness of the two stars estimate the extra error that needs to be added to the eclipse depths and times of mid-eclipse for the real WASP-35b secondary eclipse data.

6 Warm Spitzer Occultation Photometry of WASP-35b at $3.6\,\mu$m and $4.5\,\mu$m

6.1 Introduction

In Chapter 3 I presented results from Spitzer Space Telescope observations of the secondary eclipse of WASP-26b (Mahtani et al. 2013). The method used to analyse these data is the state of the art technique for the analysis of secondary eclipse observations of hot Jupiters. Currently *Spitzer* is the most reliable telescope for conducting these observations. The depth and the time of mid-eclipse are two important parameters that come from a secondary eclipse analysis. The eclipse depth gives information on the temperature of the atmosphere at the region of the atmosphere probed by the wavelength at which the eclipse is observed, and can provide evidence for the presence of molecules in the atmosphere of the planet. If multiple wavelengths have secondary eclipse depths measured then it is be possible to constrain the spectral energy distribution (SED) of the atmosphere given some assumptions on, for example, the metallicity of the planet's atmosphere. The time of mid eclipse gives $e\cos(\omega)$ which, with an analysis including transit, radial velocity and secondary eclipse data, can strongly constrain the eccentricity of the planet's orbit. These planets are expected to be on tidally locked, circular orbits because of their proximity to their host star. So if a hot Jupiter is on an eccentric orbit could be evidence of further dynamical evolution of the system. To fully understand the conclusions drawn from these two parameters realistic error bars must be quoted on the measurement of these parameters. It is generally understood that error bars that come from MCMC analyses of secondary eclipse observations are underestimated because the correlated noise in the data is not accounted for in the analysis. In this chapter I use the method of signal injection I presented in Chapter 5 to determine realistic error bars on the depth and time of mid eclipse of the secondary eclipse of WASP-35b. This is the first analysis of this data set and will be presented in a paper following the submission of this thesis (Mahtani et al. in prep.).

6.2 Observations

I present *Spitzer* (Werner et al. 2004) InfraRed Array Camera (*IRAC*) (Fazio et al. 2004) channel 1 (3.6 μm) and channel 2 (4.5 μm) secondary eclipse (occultation) data taken on 2011 April 14 and 2011 April 17, respectively (PI: J H, Program ID 60003). The *Spitzer* data were acquired in full array mode (256 $\times$ 256) and I include in this analysis all the data used in the discovery paper by Enoch et al. (2011). Table 6.1 is a summary of the data that I have used in this analysis.

Instrument	Date(s)	
WASP-N (2 cams)	10/2008-01/2009 10/2009-01/2010	Lightcurve
WASP-S (1 cam)	10/2009-01/2010	Lightcurve
RISE (V+R)	30/11/2010	Transit Lightcurve
TRAPPIST (I+z)	23/12/2010	Transit Lightcurve
FTS (z)	01/01/2011	Transit Lightcurve
TRAPPIST (I+z)	11/01/2011	Transit Lightcurve
IRAC 3.6 μm	14/04/2011	Secondary Eclipse Lightcurve
IRAC 4.5 μm	17/04/2011	Secondary Eclipse Lightcurve
FIES	25/01/2010 and 26/01/2010	3 RV points
CORALIE	05/01/2010 and 6-14/02/2010	9 RV points

Table 6.1: Summary of data used in this analysis.

6.3 Spitzer Data Reduction

The data reduction was conducted using the Image Reduction and Analysis Facility (IRAF)[1] using the same method as Anderson et al. (2011b) and Mahtani et al. (2013), which is described briefly below.

[1]IRAF is distributed by the National Optical Astronomy Observatories, which are operated by the Association of Universities for Research in Astronomy, Inc., under cooperative agreement with the National Science Foundation.

Conversion from MJy/sr to electrons was done using equation (6.1), where the gain, exposure time and flux conversion factor were taken from the image headers.

$$\text{Factor} = \frac{\text{Gain} \times \text{Exposure Time}}{\text{Flux Conversion Factor}} \tag{6.1}$$

Aperture photometry was then conducted using the PHOT procedure in IRAF, using 21 aperture radii in the range 1.5-6 pixels and with a sky annulus of inner radius 12 pixels and outer radius 20 pixels. It was found that there were stellar like objects and bad columns in some of the data. However, an iterative 3-sigma clipping was conducted which excludes those pixels. The error on the photometry was calculated from the photon statistics and the read out noise of the IRAC detectors. The readout noise values were taken from the IDL program SNIRAC_warm.pro,[2] the values for channel 1 and 2 are 16 and 10 electrons, respectively. The position of the target was measured by fitting a 1-dimensional Gaussian to the marginal distributions of flux on x and y image axes. For each data set the times of mid-exposure were converted to BJD_{TDB} (Eastman, Siverd & Gaudi 2010) and for the occultation data the light travel time (LTT) across the system (43.05s) was accounted for by subtracting the LTT from all of the *Spitzer* times.

6.4 Analysis

6.4.1 Markov Chain Monte Carlo

The parameter space was explored using a Markov chain Monte Carlo (MCMC) algorithm (Collier Cameron et al. 2007; Pollacco et al. 2008; Enoch et al. 2010) as discussed in chapter 3.4.1. The input parameters for the star that were used in the MCMC analysis are $T_{\text{eff}} = 6050 \pm 100$ and $[\text{Fe/H}] = -0.15 \pm 0.09$ (Enoch et al. 2011). Table 3.3 show the proposal parameters used in this MCMC analysis. The estimate of the epoch

[2] *ssc.spitzer.caltech.edu/warmmission/propkit /som/snirac_warm.pro*

of mid-transit was taken from the analysis of Enoch et al. (2011) so that the WASP photometry could be excluded from analysis to reduce computational time. This value along with its uncertainty were used as a Bayesian prior in all MCMC runs which used all the follow up photometry, RV data and *Spitzer* photometry. The transit model used in the analysis was the small planet approximation of Mandel & Agol (2002) with 4-parameter limb darkening coefficients taken from Claret (2004). The limb darkening coefficients were determined using an initial interpolation in $\log g_*$ and [Fe/H] and an interpolation in $T_{\rm eff}$ at each MCMC step. The limb darkening parameters used for the best-fit lightcurves are given in Table 6.2. The secondary eclipse model approximated the star and planet as two uniform discs of constant surface brightness. The projected spin-orbit angle was fixed to the value $\lambda = 0$ in the fit.

Light Curve	a_1	a_2	a_3	a_4
RISE	0.611	−0.135	0.591	−0.330
TRAPPIST 1	0.652	−0.346	0.636	−0.325
TRAPPIST 2	0.652	−0.346	0.636	−0.325
FTS	0.652	−0.346	0.636	−0.325

Table 6.2: Limb darkening coefficients

6.4.2 Trend Functions and Aperture size

Figure 6.1 shows an example of the 3.6 μm (top) and 4.5 μm (bottom) light curves produced by the photometry in IRAF. As has been seen in other secondary eclipse observations (e.g. Mahtani et al. 2013), the 3.6 μm data has a ramp during the initial stages of the observations. This occurs because the telescope has slewed from its old position to its new position and is adjusting to a new equilibrium. To see the effect of this portion of the data on the results, I clipped the first hour of both data sets. I found that the system parameters were negligibly affected by the clipping of this data. It can be seen that there is a periodic trend in the data. This is due to the variation

in the position of the target on the detector caused by flexure of the instrument as an electric heater is turned off and on.[3] The *IRAC* detectors are known to exhibit inhomogeneous intrapixel sensitivity (e.g. Knutson et al. 2008), which means there is variable sensitivity across an individual pixel. This, along with the PSF movement, results in the measured flux varying depending on the position of the PSF on the detector. Also, when small apertures are used pixelation occurs due to the undersampling of the PSF of the target (Anderson et al. 2011b). These systematics will be accounted for in the trend functions as described in chapter 2.3.3.1.

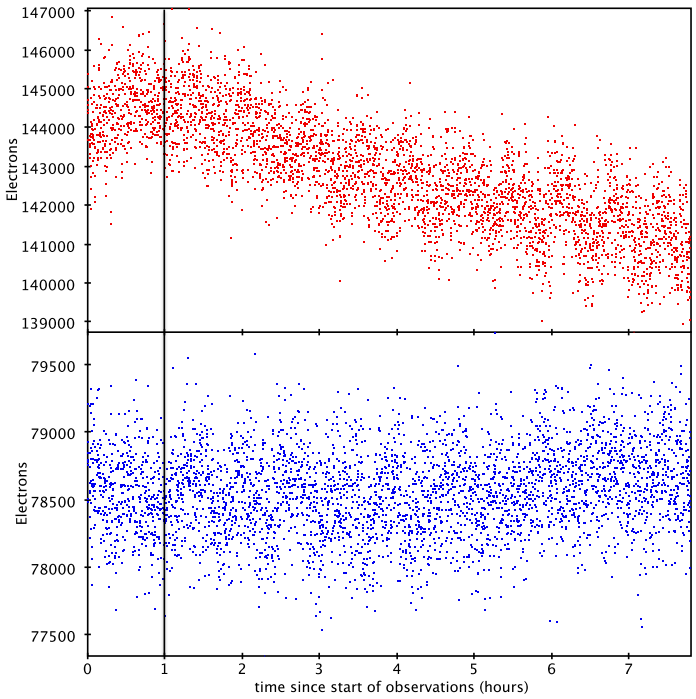

Figure 6.1: Examples of the 3.6 μm (top) and 4.5 μm (bottom) light curves produced by the photometry in IRAF. The line at 1 hour shows the data that were clipped.

For each set of trial lightcurve model parameters the residuals from the model

[3] *ssc.spitzer.caltech.edu/warmmission/news/21oct2010memo.pdf*

are calculated and then the coefficients of the detrending model are calculated using singular value decomposition applied to the entire data set. Initially, a linear-in-time and quadratic-in-space trend function was used on all 21 apertures to fit the secondary eclipse data. The RMS of the residuals was used to determine the optimal aperture size. Once this was determined, combinations of none, linear and quadratic trend functions in time and space were used on the best aperture to determine the best fitting trend function.

To determine which trend function gave better results the Bayesian Information Criterion (BIC, equation 2.7) was used.

Using the RMS of the residuals it was found that the best aperture to use was 2.5 pixels in both channels. The system parameters are negligibly affected by the choice of aperture radius around this value. It was found that the quadratic-in-space with linear time trend function gave the best fit to the channel 1 data and that the linear-in-space with no time trend function gave the best fit to the data to the channel 2 data. It was found that the addition of the quadratic term for the spatial decorrelation and linear time improved our BIC by ~ 110 in channel 1 over our base line model of no-time and linear space. For channel 2 there was no improvement in the BIC for models more complicate than no-time and linear space. Figure 6.2 shows the best raw and detrended lightcurve as determined by this analysis and Table 6.3 shows the best system parameters of this analysis.

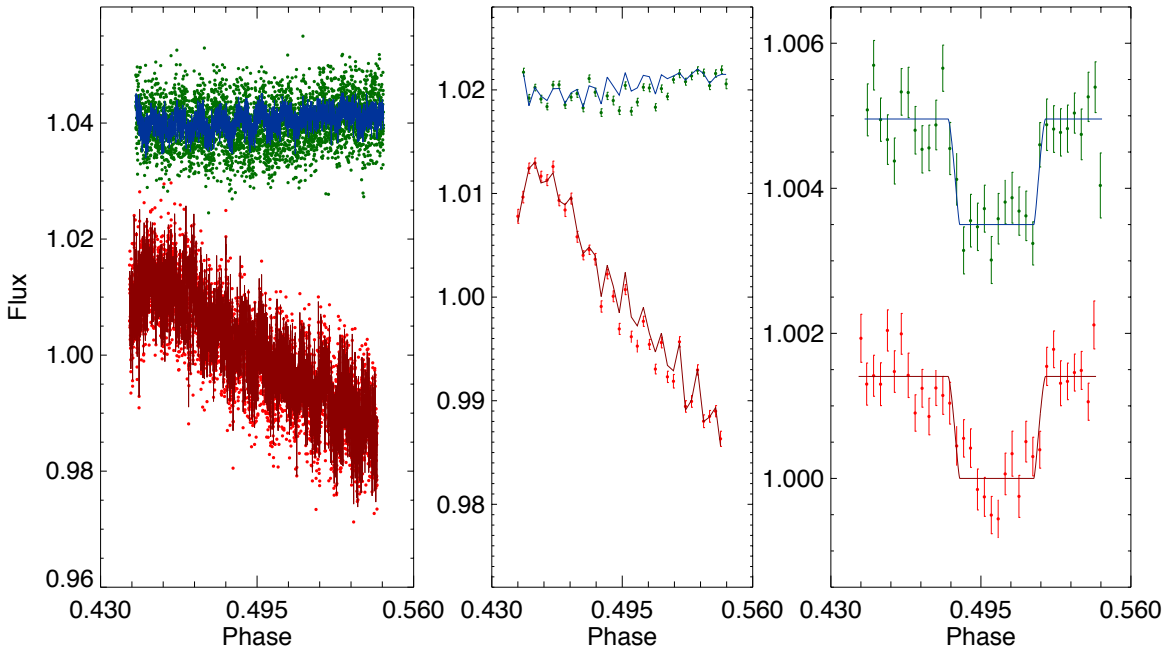

Figure 6.2: (Left): The raw light curves with the trend functions, the upper points are the channel 2 data and the lower points are the channel 1 data, the solid lines are the trend functions for each data set. (Middle) Binned light curves with trend models. (Right) The binned light curve with trend function removed and best fitting eclipse models (solid lines). The secondary eclipse can clearly be seen in both channels.

Parameter (Unit)	Value
P (d)	3.161529±0.000020
$T_{\rm c}$ (HJD)	2455547.28762±0.00010
T_{14} (d)	0.12743±0.00058
$T_{12} = T_{34}$ (d)	0.01513±0.00056
$\Delta F = R_{\rm P}^2/{\rm R}_*^2$	0.01530±0.00016
b	$0.284^{+0.047}_{-0.061}$
i (°)	$88.01^{+0.45}_{-0.37}$
K_1 (km s^{-1})	0.0960±0.0071
γ (km s^{-1})	17.7181±0.0041
$e\cos\omega$	$0.00298^{+0.00088}_{-0.00085}$
$e\sin\omega$	$0.023^{+0.016}_{-0.018}$
e	0.023±0.016
ω (°)	$82.^{+3.}_{-23.}$
$\phi_{\rm mid-occultation}$	$0.50190^{+0.00056}_{-0.00054}$
T_{58} (d)	$0.1330^{+0.0040}_{-0.0042}$
$T_{56} = T_{78}$ (d)	$0.01589^{+0.00085}_{-0.00078}$
M_* ($M_\odot$)	$1.071^{+0.022}_{-0.021}$
R_* ($R_\odot$)	$1.105^{+0.028}_{-0.027}$
$\log g_*$ (cgs)	$4.381^{+0.018}_{-0.019}$
ρ_* ($\rho_\odot$)	$0.793^{+0.054}_{-0.052}$
$T_{\rm eff}$ (K)	5960^{+83}_{-82}
[Fe/H]	-0.150±0.090
$M_{\rm P}$ ($M_{\rm Jup}$)	0.726±0.055
$R_{\rm P}$ ($R_{\rm Jup}$)	$1.330^{+0.039}_{-0.037}$
$\log g_{\rm P}$ (cgs)	$2.972^{+0.037}_{-0.039}$
$\rho_{\rm P}$ ($\rho_{\rm J}$)	$0.308^{+0.034}_{-0.031}$
a (AU)	0.04313±0.00029
$T_{\rm P,A=0}$ (K)	1455±28

Table 6.3: System parameters of the WASP-35 system

6.5 Results and Discussion

6.5.1 Error bar correction

WASP-35 and HAT-P-2 have V-band magnitudes of 10.94 and 8.69, respectively, so to accurately simulate secondary eclipses of WASP-35b extra white noise needs to be

added to the HAT-P-2 data. I first calculated for each channel the amount of binning of the HAT-P-2 data set that was required such that the simulated data had the same cadence as the real WASP-35b lightcurves. The time sampling required for the HAT-P-2 data was 6.86s so the sections of data selected from this sample were binned by a factor of 17.4. Using the mean flux and mean error on from the photometry of WASP-35 the HAT-P-2 (data after binning) I calculated the fractional uncertainty of the flux (σ_f/f). The amount of extra white noise that needs to be added into the HAT-P-2 data such that it has the same fractional uncertainty as the WASP-35 data was 0.00254 and 0.003478 for channel 1 and 2 data respectively. The data train used was 4096 data points because 2^n, where n is an integer, data points were required for wavelet fitting. I then injected eclipses with the same depth as WASP-35b into the HAT-P-2 data and fit it using a polynomial and wavelet fitting method 10,000 times. I found that the distributions of the polynomial and wavelet fits were consistent with each other so no extra information is gained by using the more complicated wavelet fitting. The distributions the depth and mid-eclipse times for the channel 1 data are shown in Figures 6.3 and 6.4 and similar results were found for the channel 2 data. In the following I only use the results from the polynomial fitting. Using the standard deviation of the recovered eclipse depths and times of mid-eclipse I evaluate the amount of systematic noise that needs to be added to the WASP-35 uncertainties such that they have the same value as the standard deviation of the polynomial fits. Table 6.4 gives the amount of extra error that needs to be added in to the error bars on the two parameters calculate using this method.

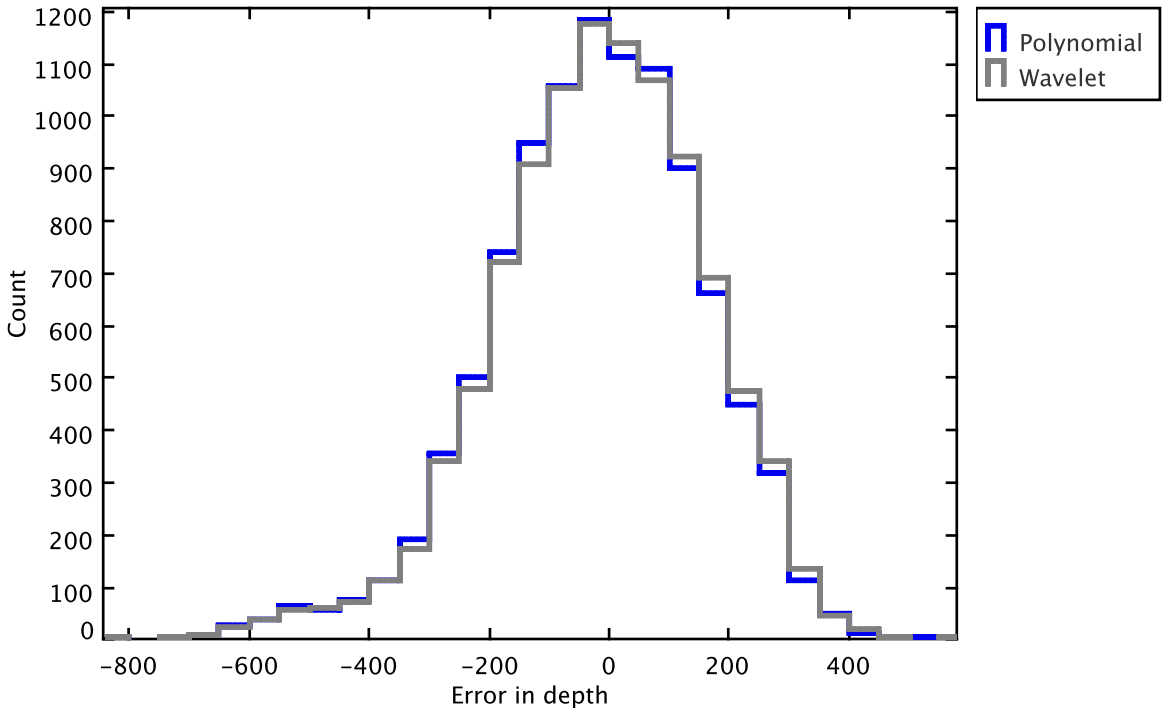

Figure 6.3: The distributions of the secondary eclipse depths recovered using the polynomial and wavelet fitting of the semi-synthetic secondary eclipse lightcurves of WASP-35b with the extra white noise added into the HAT-P-2 data.

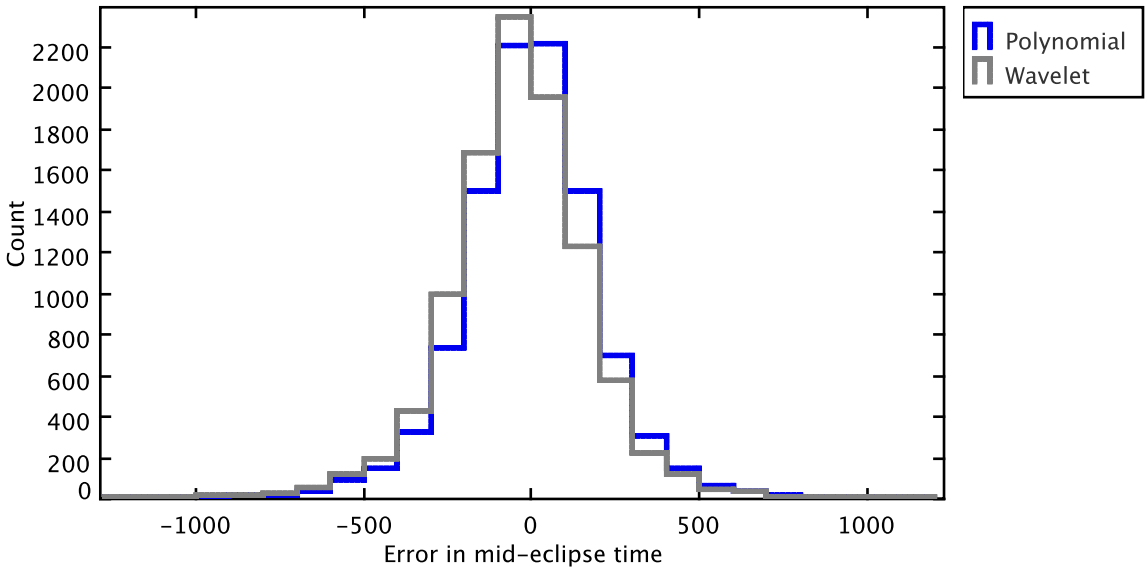

Figure 6.4: The distributions of the secondary eclipse times of mid-eclipse recovered using the polynomial and wavelet fitting of the semi-synthetic secondary eclipse lightcurves of WASP-35b with the extra white noise added into the HAT-P-2 data.

Wavelength	Eclipse error (PPM)	Time of mid-eclipse error (s)
3.6 μm	140	150
4.5 μm	130	125

Table 6.4: The extra amount of error that was required to inflate the error bars on the simulated WASP-35 lightcurves

6.5.2 Eclipse Depths and Brightness Temperatures

I find that the eclipse depths for WASP-35 at 3.6 μm and 4.5 μm relative to an out-of-eclipse value of 1 that come directly out of the MCMC (i.e., no extra noise correction) are 0.00141 ± 0.00011 and 0.00146 ± 0.00012, respectively. These eclipse depths correspond to brightness temperatures of 1654±51K and 1461±50K. To find these blackbody

temperatures the expected flux ratios were calculated using Planck functions at different temperatures for the planet and synthetic spectra from stellar models (Philip, Upgren & Janes 1991) for the star. These flux ratios were then integrated over the *Spitzer* band passes to calculate the expected measured flux ratio. The temperatures above correspond to the best fitting Planck function temperature to the individual eclipse depths. The errors were calculated using a simple Monte Carlo method. The brightness temperatures suggest that, on average, the emission at mid-infrared wavelengths from the irradiated hemisphere of WASP-35b is consistent with the spectrum of a non-thermally inverted atmosphere.

Figure 6.5 shows the activity-inversion as described in Knutson, Howard & Isaacson (2010) with the addition of the circle which is WASP-26 and the open triangles is WASP-35b. WASP-35b had 2 spectra taken using the WHT with the ISIS spectrograph as part of an activity monitoring program of exoplanet host stars (Vilela and Southworth in prep and see Mancini et al. 2014 for details on data reduction) on the night of 2012/12/23, the two open triangles give an indication of the scatter in the measured activity proxy over the course of one night. It is interesting to see that the blackbody temperatures of the secondary eclipses of WASP-35 suggest that the atmosphere is a not-thermally inverted. However, their positions on the plot suggest that the atmosphere of WASP-35 should be thermally inverted, if the relation is real and holds. Inflating the error bars on the eclipse depths by the values in Table 6.4 gives 180ppm for both channel 1 and 2, these now give blackbody temperatures of 1658 ± 79 and 1461 ± 74 for channel 1 and 2 respectively . As expected the error bars on the blackbody temperatures increase but they are still consistent with a non inverted atmosphere. These eclipse depths need to be fitted with atmospheric models as was done for my WASP-26b analysis (Mahtani et al. 2013). This would give a better indication of whether the atmosphere of WASP-35b is inverted.

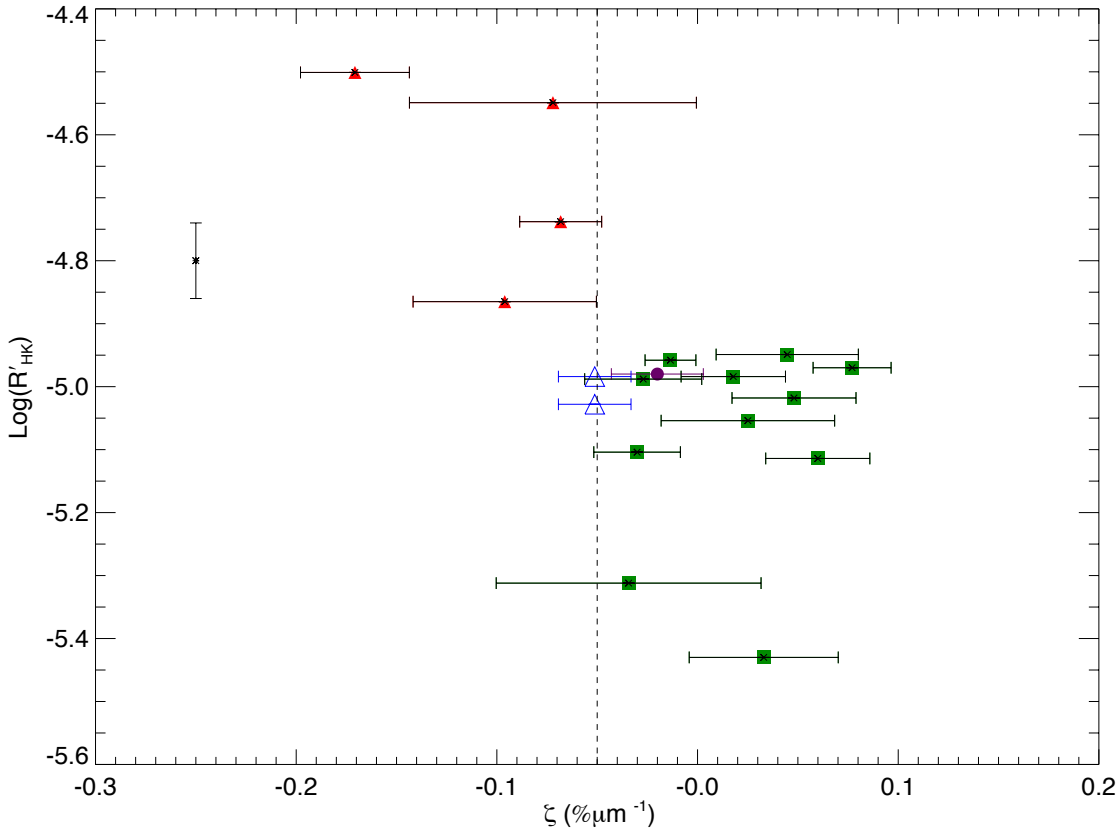

Figure 6.5: Activity-inversion plot for the stars in Knutson, Howard & Isaacson (2010). Points on the left of the dotted line (triangles) are non-inverted planets around active stars and those on the right of the dotted line (squares) are inverted planets around inactive stars. The point on the left hand side of the plot shows the typical change in $\log R'_{HK}$ (season-to-season), assuming measurements over several nights. The circle is WASP-26 and the open triangles are WASP-35b.

6.5.3 Eccentricity

The MCMC results give the time of mid-eclipse to be $0.50190^{+0.00056}_{-0.00054}$. This gives an offset from a phase of 0.5 of 520 ± 150 seconds. This suggests a non-zero eccentricity at the 3.5σ level. This result come from the simultaneous fit of both the channel 1 and channel 2 data so for the inflation of error bars I will use the conservative value of

150 seconds. This gives a new error for the offset of 520 ± 212 seconds. This reduces the significance of the eccentricity to 2.5σ. It has already been seen that the true distributions of this parameter are non-Gaussian so to better test the significance I looked at distributions from the simulated lightcurves. I calculated what proportion of the 10000 simulated lightcurves (for both channel 1 and 2) for a circular orbit that were fit by the polynomial methods have an absolute value of the offset of more than 520 seconds. My findings show that this only happens at most 3% of the time. If this tentative detection of a non-circular orbit can be confirmed it may be relevant to the formation history of this hot Jupiter and the effects of tidal heating on its current structure, as discussed in section 1.4

6.6 Conclusion

In this chapter I present new warm *Spitzer* photometry of WASP-35b at $3.6\,\mu$m and $4.5\,\mu$m. I report the first detection of the occultation of WASP-35b with eclipse depths (after error bar inflation for extra noise) at $3.6\,\mu$m and $4.5\,\mu$m of 0.00141 ± 0.00018 and 0.00146 ± 0.00018, respectively which correspond to brightness temperatures of 1654 ± 51K and 1461 ± 50K. My analysis suggests that the atmosphere of WASP-35b is consistent, according to the brightness temperatures, with a non-thermally inverted atmosphere. However, if the Knutson, Howard & Isaacson (2010) activity-inversion relation holds for WASP-35b, then it would be expected to host a thermal inversion. A full spectral retrieval is required to better constrain the true nature of the atmosphere of WASP-35b and also to determine if any additional secondary eclipse data can give any further constraint. I also find that the eccentricity of the planet's orbit is non-zero.

7 Discussion, Conclusions and Future Work

7.1 Hot Jupiter atmospheric variability

The work I have conducted during my Ph.D. has led me to thinking about orbit-to-orbit-variability in the atmospheres of hot Jupiters. Just looking at the Earth, there is significant variability in the cloud coverage. For an outside observer this would change the observed emission spectrum. Moving to a more applicable analogy, Jupiter and Saturn are seen to have large storms which can well up material from lower regions of the atmosphere and hence change the emergent emission spectrum (Fletcher et al. 2011). To be able to detect variability we first need to be able to conduct reliable repeat observations of secondary eclipses. Recent work by Wong et al. (2014) has shown that their repeat observations of secondary eclipse depths at 4.5 μm are precise better than 79ppm. However, Hansen, Schwartz & Cowan (2014) presented results that found that repeat observations of secondary eclipses observed with *Spitzer* were discrepant by 500ppm or that the error bars are underestimated by a factor of 3. The eclipse depths of the planets in the Hansen, Schwartz & Cowan (2014) sample, with their published uncertainties, were fit with Planck functions at the central wavelength of the bandpass they were observed. Using the BIC for each eclipse depth were calculated and these results are shown in Figure 7.1.

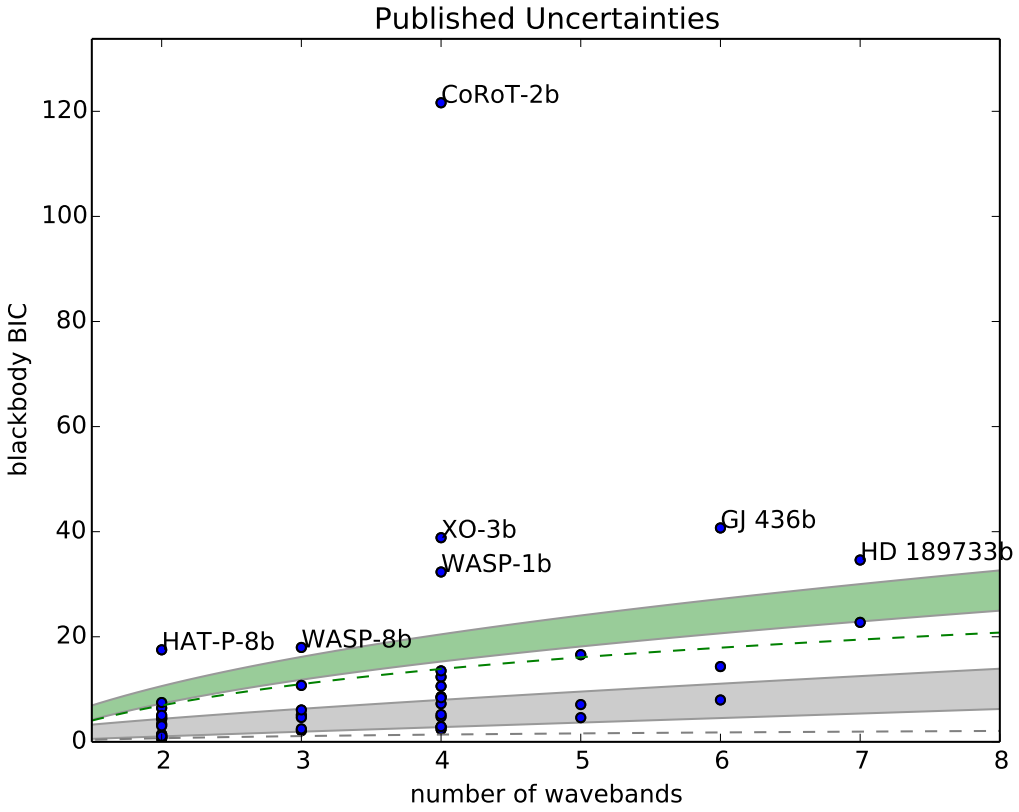

Figure 7.1: Comparing the BIC for the published eclipse depths and the published uncertainties to perfect ($\chi^2 = 0$, dotted line) and good ($\chi^2 = N$, solid shaded regions) fits to a blackbody (grey) and spectral retrieval (green) (Hansen, Schwartz & Cowan 2014).

The grey dotted line in Figure 7.1 shows the predicted BIC for a given number of observations assuming a perfect fit to the data (i.e., $\chi^2 = 0$). The shaded grey region is the 68.3% confidence interval of the χ^2 distribution given a reduced χ^2 of 1. In this case the only parameter that is free is the temperature of the blackbody and hence $K = 1$. For spectral retrieval the normal number of free parameters is 10, 6 for the T-P profile and 4 for the molecular abundances. The same BIC calculations were conducted for the spectral retrieval method and are plotted as the green dotted line ($\chi^2 = 0$) and shaded green region($\chi^2 = 1$). Points that lie above the green shaded region are better

fit by the spectral retrieval method than blackbody fits. Points that lie between the two shaded regions are better fit by the blackbody model. It can be seen that there are 7 planets here that are better fit by spectral retrieval.

The same calculations were done but the uncertainties are inflated by adding in the 500 PPM error (Figure 7.2) or multiplying the error bars by a factor of 3 (results similar to Figure 7.2).

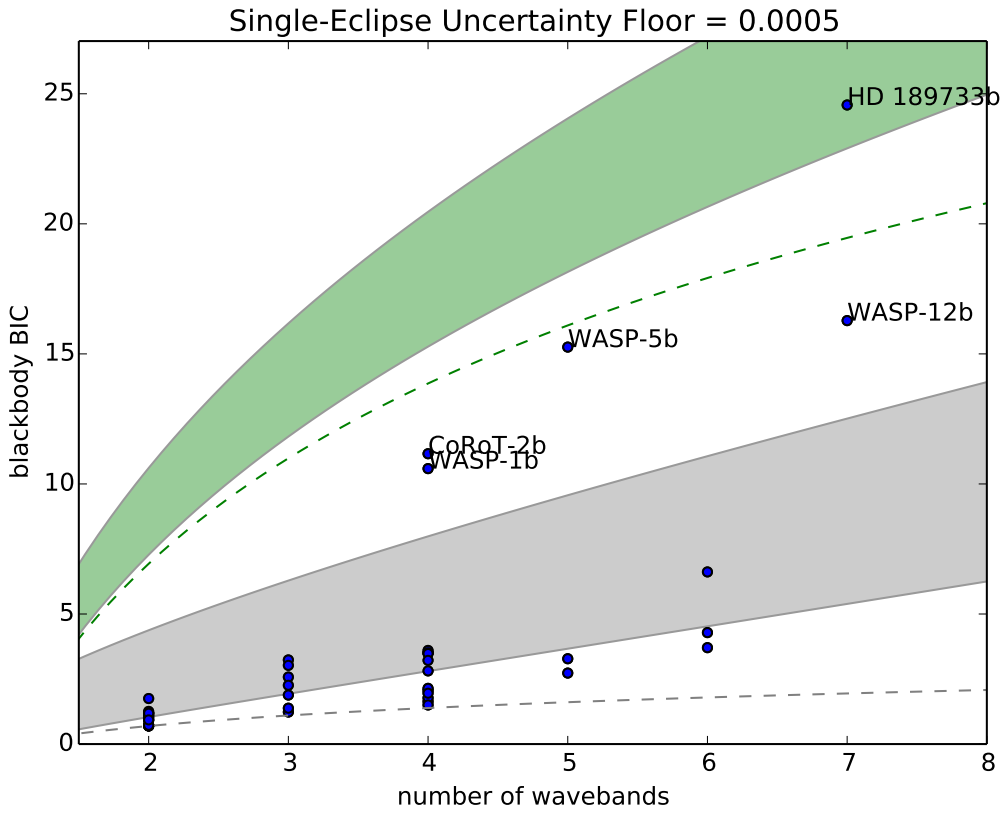

Figure 7.2: Comparing the BIC for a black body fit to the published eclipse depths with 500ppm added in quadrature to the published uncertainties to perfect ($\chi^2 = 0$, dotted line) and good ($\chi^2 = N$, solid shaded regions) fits to a blackbody (grey) and spectral retrieval (green) Hansen, Schwartz & Cowan (2014).

One will always get a better fit using a more complicated model because there are

more free parameters. The BIC is used to determine if a more complicated model is justifiable. Figures 7.2 shows that, apart from HD189733 b, all other planets with secondary eclipse observations show no evidence that the extra free parameters in the spectral retrieval model justify its use.

The results of Wong et al. (2014) show that secondary eclipse depths at 4.5 μm in the same observing set up as used in their work, are repeatable to very high accuracy. This also means that if variability occurs it may be detectable. In this case the orbit-to-orbit variability must be larger that 79ppm to be detectable. These results of Hansen, Schwartz & Cowan (2014) could be due to the different observing modes of the data. This is evidence for the need of a homogeneous analysis of secondary eclipse data and needs to be conducted if we want to look for orbit-to-orbit variations in other *Spitzer* secondary eclipse data.

Although no orbit-to-orbit variability was detected for the eclipse depths of XO-3b (Wong et al. 2014) this does not mean that all hot Jupiters have non-variable atmospheres. It should also be noted that the atmospheres of eccentric giant planets such as XO-3b are dominated by diurnal forcing because of the variable stellar flux impacting the atmosphere. For example, the incident stellar flux of XO-3b varies by a factor of ~ 3 between perigee and apogee. Although this could mean that this class of hot Jupiters are more likely to show variability, the fact that this system does not show that, should not discourage the same analysis for other systems.

A recent paper by Parmentier, Showman & Lian (2013) showed that orbit-to-orbit variability could be due to variations in the high atmospheric absorber that causes thermal inversions to form. It has been hypothesised (Hubeny, Burrows & Sudarsky 2003; Fortney et al. 2008) that the high atmospheric absorber could be TiO. However, due to its high mean molecular weight it should gravitationally settle to high pressure regions of the atmosphere, and hence having TiO at high altitudes is very difficult. Another problem is that cold traps on the night-side of the planet would cause the TiO to condense and rain out of the high altitude regions of the atmosphere (Parmentier, Showman & Lian 2013). A mechanism that was thought to bring this heavy molecule to low pressure regions of the atmosphere was convection. This had been parametrised

by the K_{ZZ} parameter in atmospheric models. In Parmentier, Showman & Lian (2013) models have shown that winds from the nightside to the dayside of the planet could drive this material to the upper atmosphere such that it is able to form a thermal inversion. They also predict that this should result in strong temporal and spatial variability of this absorber. Their models show that for particles that are larger than $\sim 1\,\mu$m the variability of this absorber could cause variability in the presence of a thermal inversion on timescales of 10-100 Earth days. The presence of a thermal inversion is currently deduced by observing the eclipse depths at $3.6\,\mu$m and $4.5\,\mu$m using *Spitzer*. So repeat sets of these observations (where each pair of observations is observed as close together as possible) could allow the detection of variable thermal inversions in hot Jupiters. To determine what level of variability is detectable for a particular system, one could use the signal injection method used here but to vary the injected depths. With this information, one could use the slope measurement techniques presented in Knutson, Howard & Isaacson 2010 to determine at what level of variation, changes the interpretation of the atmosphere (with/without a thermal inversion). If this variability is smaller than the uncertainty on the eclipse depth, the analysis can be redone to determine at what level the variability needs to be such that the switch from inverted to non-inverted (or vice versa) occurs for that system.

TiO is also important in the formation of silicate in the atmosphere of hot Jupiters (Parmentier, Showman & Lian 2013). Silicates form clouds and hazes and so variations in TiO could lead to variations cloud coverage on hot Jupiters. This could be seen as variations in the albedo and hence reflected light component of secondary eclipses which could be measured by the Kepler space telescope. So this work suggests that a reanalysis of Kepler data of the most highly irradiated hot Jupiters could lead to the detection of temporal variability in the atmospheres of hot Jupiters. Also, variations in cloud coverage would also cause variations in the eclipse depths of hot Jupiters which could be measured with *Spitzer*.

Wong et al. (2014) also analysed their global fit of all of their secondary eclipses for deviations from a uniform disk model. It is generally assumed when analysing these data that the measured light from the planet is uniform over the disc. However, during

ingress/egress it can be imagined that the planet is being sliced from pole to pole by the limb of the star. By analysing the residuals from a uniform disk model during this time it may be possible to detect features in the atmosphere, for example an offset in the hotspot from the sub-stellar point (e.g. Knutson et al. 2007). The results of this analysis (shown in Figure 7.3) found that no deviation from a uniform disk were seen above the noise level and the upper limit placed on this kind of variability is 500ppm. Similar work has been conducted for HD189733b by Majeau, Agol & Cowan (2012) and de Wit et al. (2012).

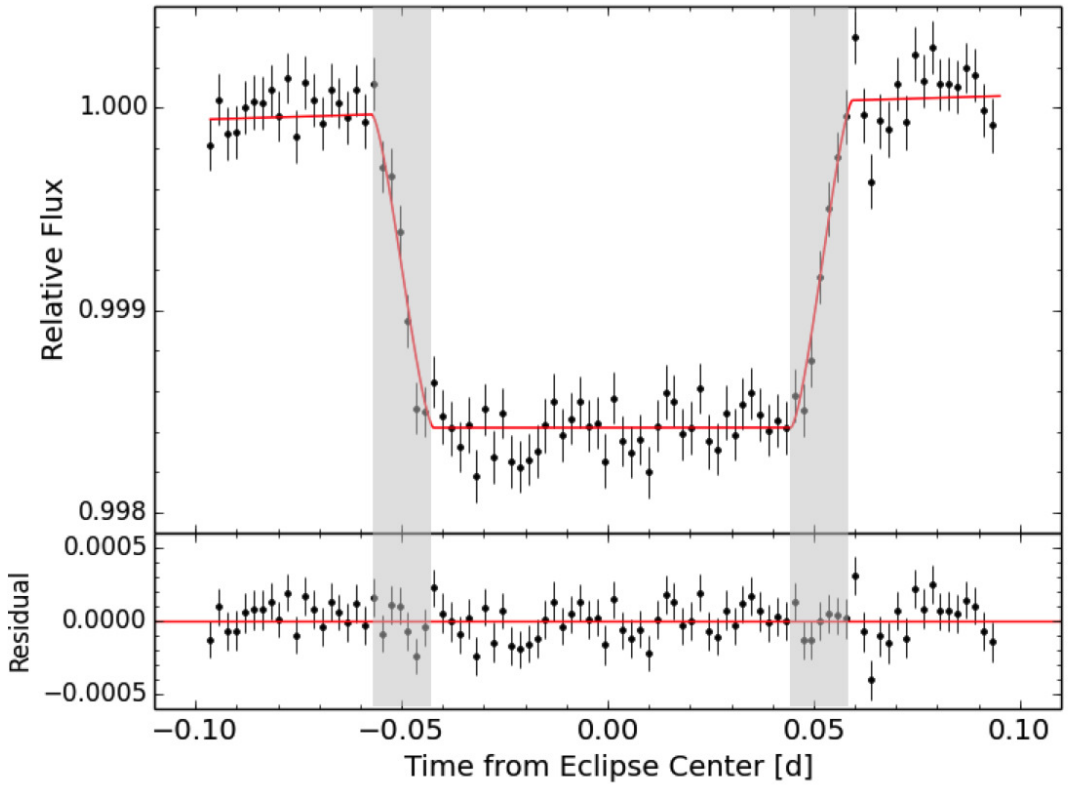

Figure 7.3: Combined data of all 12 secondary eclipses from Wong et al. (2014) binned on a time scale of 3 minutes. The uniform disk model is over plotted (solid line) on the data (black points with error bars). The shaded regions denote the ingress and egress of the lightcurve where the deviations from a uniform disk would be seen if they were to be there and detectable.

7.2 Future work

I am interested in conducting further work to see if there is any detectable orbit-to-orbit variability in the atmospheres of hot Jupiters. The way I propose to do this is to first choose a well studied system (e.g., HD189733 or HD209458) and to re-reduce and analyse all the Spitzer 3.6 μm and 4.5 μm data. The goal of redoing this analysis is to

alleviate any differences in analysis methods that could lead to systematic errors. Then I will take the mean eclipse depth of all the individual eclipse depth measurements at each wavelength and inject that into a portion of a phase curve for that system. If no phase curve is measured then I will look for a star of similar spectral type and brightness that does have a phase curve measured and use that data for the signal injection. Then I will inflate the error bars using the methods I presented in this thesis and compare the eclipse depths. Any potential variability will be seen when plotting these eclipse depths against time.

The variability that will be present will be a combination of both the host star and the planet. Hence, there is ambiguity as what proportion of any variability seen is stellar and planetary in nature. Stellar variability includes magnetic activity, granulation and pulsations. To asses these a constant monitoring program is needed. To estimate the contribution of the magnetic activity of star to any variability detected, I want to use the proxy $\log(R'_{HK})$. With long term observations of this proxy for magnetic activity I would like to use the new Gaussian process methods (e.g. Gibson et al. 2012) to fit these measurements. This will also allow one to predict the value of $\log(R'_{HK})$ between the data points. Working along side stellar variability experts (e.g., Suzanne Aigrain who has a long term monitoring program of HD189733b) I would find methods of using this data to determine the stellar magnetic activity contribution to any variability detected. To determine the level of stellar variability (e.g., pulsations and granulation) that contributes to any orbit-to-orbit variability in eclipse depths is not an easy task. Asteroseismology will be needed to understand photometric variability of stars. We have found many planets around Sun-like stars. However, solar-like stars oscillate on time-scales of minutes to hours. However, the level of variability is only a few ppm (Aerts, Christensen-Dalsgaard & Kurtz 2010). This level is only achievable through space based missions. With the development of the next generation of telescopes (e.g., PLATO, TESS) this level may be achievable. This would mean this systematic error could be removed from any potentially detectable variability in eclipse depths so that only the variation of the planet is estimated.

To asses the possibility that variability could be caused by a nearby or companion

star, high spatial resolution, adaptive optics images can be taken of the star at multiple wavelengths. If no other stars are detected in these images it is possible to use the limiting magnitude of the telescope and instrument used to determine an upper limit to the amount of variability caused by any unseen close by stars.

A long term goal of this work is to build a catalogue of eclipse depths that have all been analysed in a homogeneous manner. Eventually I want to develop the code used in this work to allow this method to be used on any secondary eclipse data. This will allow a homogeneous study of secondary eclipses at all wavelengths and allow for a thorough catalogue to be established. A catalogue of eclipse depths will be of use when optimum target selection is required for the next generation of telescopes.

7.3 Looking Forward: From Spitzer to JWST and beyond

Currently atmospheric characterisation is only possible for the hot Jupiters and other large planets that orbit bright stars. In the future, with missions such as The Next Generation Transit Survey (NGTS), The James Webb Space Telescope (JWST), The European Extremely Large Telescope (EELT) and Transiting Exoplanet Survey Satellite (TESS) planets analogues to the Earth will be able to detect the signals of their atmospheres. So accounting for the systematic errors in the data will be vital for detecting these very small amplitude signals. In these data we will be looking for the signatures that are indicative of life on another world. There are hundreds of hot Jupiters that have been found by the SupeWASP survey, so these can be used to develop and improve this method (through a homogeneous analysis) so that when potentially life-bearing planets are found, this method will be fully developed and ready to help look for these very faint signals in the data. This method of signal injection into *real* data is a step that needs to be conducted during the commissioning of these next generation of telescopes. This method will allow the most information to be gained from the data.

7.4 Conclusions

In this thesis I have investigated how to account for systematic errors that are present in *Spitzer* secondary eclipse photometry of hot Jupiters. The next step is to take this information and see how inflating the error bars on these data affects the conclusions drawn from fitting atmospheric models to the data. It will also allow for further investigations into orbit-to-orbit variability to be conducted. With the new generation of telescopes that are being built, the field of exoplanet atmospheres is going to have many dedicated instruments. It is thus a very exciting time to be working in this area.

Publications

Refereed

D. P. Mahtani, P. F. L. Maxted, D. R. Anderson, A. M. S. Smith, B. Smalley, J. Tregloan-Reed, J. Southworth, N. Madhusudhan, A. Collier Cameron, M. Gillon, J. Harrington, C. Hellier, D. Pollacco, D. Queloz, A. H. M. J. Triaud, and R.G. West
Warm Spitzer occultation photometry of WASP-26b at 3.6 and 4.5 μm
2013, MNRAS, 432, 693

P. F. L. Maxted, A. M. Serenelli, T. R. Marsh, S. Cataln, D. P. Mahtani, and V. S. Dhillon WASP 1628+10 an EL CVn-type binary with a very low mass stripped red giant star and multiperiodic pulsations
2014, 444,208

Bibliography

Aerts C., Christensen-Dalsgaard J., Kurtz D., 2010, Asteroseismology, Astronomy and Astrophysics Library. Springer

Agol E., Cowan N. B., Knutson H. A., Deming D., Steffen J. H., Henry G. W., Charbonneau D., 2010, ApJ, 721, 1861

Albrecht S., Winn J. N., Butler R. P., Crane J. D., Shectman S. A., Thompson I. B., Hirano T., Wittenmyer R. A., 2011, ApJ, 744, 189

Albrecht S. et al., 2012, ApJ, 757, 18

Anderson D. R. et al., 2011a, A&A, 534, A16

Anderson D. R. et al., 2010, ApJ, 709, 159

Anderson D. R. et al., 2011b, MNRAS, 416, 2108

Anderson D. R. et al., 2013, MNRAS, 430, 3422

Asplund M., Grevesse N., Sauval A. J., Scott P., 2009, Annu. Rev. Astron. Astrophys., 47, 481

Bakos G. Á., Lázár J., Papp I., Sári P., Green E. M., 2002, PASP, 114, 974

Baliunas S. L. et al., 1995, ApJ, 438, 269

Ballard S. et al., 2010, PASP, 122, 1341

Ballard S. et al., 2011, ApJ, 743, 200

Baraffe I., Chabrier G., Barman T. S., Allard F., Hauschildt P. H., 2003, A&A, 402, 701

Barclay T. et al., 2013, Nature, 494, 452

Baruteau C. et al., 2014, Protostars and Planets VI, 667

Batalha N. M. et al., 2011, ApJ, 729, 27

Batalha N. M. et al., 2013, ApJS, 204, 24

Batygin K., Stevenson D. J., 2010, ApJL, 714, L238

Bayes M., Price M., 1763, Philosophical Transactions, 53, 370

Beerer I. M. et al., 2011, ApJ, 727, 23

Bennett D. et al., 2008, ApJ, 648, 663

Berta Z. K., Irwin J., Charbonneau D., Burke C. J., Falco E. E., 2012, AJ, 144, 145

Beuzit J.-L. et al., 2008, in Society of Photo-Optical Instrumentation Engineers (SPIE) Conference Series, Vol. 7014, Society of Photo-Optical Instrumentation Engineers (SPIE) Conference Series, p. 18

Bodenheimer P., Laughlin G., Lin D. N. C., 2003, ApJ, 592, 555

Borucki W. J. et al., 2010, Science, 327, 977

Bouchy F. et al., 2005, A&A, 444, L15

Brandt T. D. et al., 2014, ApJ, 786, 1

Burke C. J. et al., 2010, ApJ, 719, 1796

Burrows A., Hubeny I., Budaj J., Knutson H., Charbonneau D., 2007, ApJ, 668, L171

Burrows A., Sharp C. M., 1999, ApJ, 512, 843

Burrows A. S., 2014, Proceedings of the National Academy of Science, 111, 12601

Carroll B. W., Ostlie D. A., 1996, An introduction to modern astrophysics; 1st ed. Addison-Wesley, Reading, MA

Carter J. A., Winn J. N., 2009, ApJ, 704, 51

Carter J. A., Winn J. N., 2010, ApJ, 709, 1219

Cegla H., 2013, PhD thesis, Queens Quniversity Belfast

Chabrier G., Baraffe I., Allard F., Hauschildt P., 2000, ApJ, 542, 464

Chamberlain J. W., 1978, Theory of planetary atmospheres: an introduction to their physics and chemistry, Vol. 22. Academic Press

Chan T., Ingemyr M., Winn J. N., Holman M. J., Sanchis-Ojeda R., Esquerdo G., Everett M., 2012, aj, 144, 90

Charbonneau D. et al., 2005, ApJ, 626, 523

Charbonneau D. et al., 2009, Nature, 462, 891

Charbonneau D., Brown T. M., Noyes R. W., Gilliland R. L., 2002, ApJ, 568, 377

Charbonneau D., Knutson H. A., Barman T., Allen L. E., Mayor M., Megeath S. T., Queloz D., Udry S., 2008, ApJ, 686, 1341

Chen G., van Boekel R., Madhusudhan N., Wang H., Nikolov N., Seemann U., Henning T., 2014a, A&A, 564, A6

Chen G. et al., 2014b, A&A, 563, A40

Christiansen J. L. et al., 2010, ApJ, 710, 97

Claret A., 2004, A&A, 428, 1001

Collier Cameron A. et al., 2007, MNRAS, 380, 1230

Cosentino R. et al., 2012, in Society of Photo-Optical Instrumentation Engineers (SPIE) Conference Series, Vol. 8446, Society of Photo-Optical Instrumentation Engineers (SPIE) Conference Series

Cowan N. B., Agol E., 2011, ApJ, 729, 54

Cowan N. B., Agol E., Charbonneau D., 2007, MNRAS, 379, 641

Cowan N. B., Machalek P., Croll B., Shekhtman L. M., Burrows A., Deming D., Greene T., Hora J. L., 2012, ApJ, 747, 82

Dawson R. I., Murray-Clay R. A., Johnson J. A., 2015, ApJ, 798, 66

de Wit J., Gillon M., Demory B.-O., Seager S., 2012, 548, A128

Deming D. et al., 2011, AJ, 726, 95

Deming D. et al., 2011, ApJ, 726, 95

Deming D., Seager S., Richardson L. J., Harrington J., 2005, Nature, 434, 740

Désert J.-M. et al., 2011, ApJ, 197, 14

Díaz R. F. et al., 2012, A&A, 538, A113

Dumusque X. et al., 2012, Nature, 491, 207

Dumusque X., Udry S., Lovis C., Santos N. C., Monteiro M. J. P. F. G., 2011, A&A, 525, A140

Duncan D. K. et al., 1991, ApJS, 76, 383

Eastman J., Gaudi B. S., Agol E., 2013, PASP, 125, 83

Eastman J., Siverd R., Gaudi B. S., 2010, PASP, 122, 935

Enoch B. et al., 2011, aj, 142, 86

Enoch B., Collier Cameron A., Parley N. R., Hebb L., 2010, A&A, 516, A33

Fabrycky D. C. et al., 2012, ApJ, 750, 114

Fazio G. G. et al., 2004, ApJS, 154, 10

Finkbeiner A., 2014, Nature, 511, 22

Fletcher L. N. et al., 2011, Science, 332, 1413

Föhring D., Dhillon V. S., Madhusudhan N., Marsh T. R., Copperwheat C. M., Littlefair S. P., Wilson R. W., 2013, MNRAS, 435, 2268

Ford E. B., 2005, AJ, 129, 1706

Ford E. B., 2006, ApJ, 642, 505

Ford E. B. et al., 2012a, ApJ, 750, 113

Ford E. B. et al., 2012b, ApJ, 756, 185

Ford E. B. et al., 2011, ApJS, 197, 2

Fortney J. J., 2004, PhD thesis, THE UNIVERSITY OF ARIZONA

Fortney J. J., Hubbard W. B., 2003, Icarus, 164, 228

Fortney J. J., Lodders K., Marley M. S., Freedman R. S., 2008, ApJ, 678, 1419

Fortney J. J., Marley M. S., 2007, ApJL, 666, L45

Fortney J. J., Marley M. S., Barnes J. W., 2007, ApJ, 659, 1661

Fortney J. J., Saumon D., Marley M. S., Lodders K., Freedman R. S., 2006, ApJ, 642, 495

Fressin F., Knutson H. A., Charbonneau D., O'Donovan F. T., Burrows A., Deming D., Mandushev G., Spiegel D., 2010, ApJ, 711, 374

Gardner J. P. et al., 2006, Sp. Sci. Rev., 123, 485

Gaudi B. S., Winn J. N., 2007, ApJ, 655, 550

Gelman A., Carlin J. B., Stern H. S., Rubin D. B., 2003, Bayesian Data Analysis. New York: Chapman and Hall

Gibson N. P., Aigrain S., Roberts S., Evans T. M., Osborne M., Pont F., 2012, MNRAS, 419, 2683

Graham J. R. et al., 2007, ArXiv e-prints

Gray D., 2005, The Observation and Analysis of Stellar Photospheres. Cambridge University Press

Guyon O., Hinz P. M., Cady E., Belikov R., Martinache F., 2014, ApJ, 780, 171

Hall J. C., 2008, Living Reviews in Solar Physics, 5, 2

Handler G., 2013, Asteroseismology, Springer Netherlands, p. 207

Hansen B. M. S., 2008, ApJS, 179, 484

Hansen C. J., Schwartz J. C., Cowan N. B., 2014, MNRAS, 444, 3632

Hartmann L., Soderblom D. R., Noyes R. W., Burnham N., Vaughan A. H., 1984, ApJ, 276, 254

Haswell C., 2010, Transiting Exoplanets. Cambridge University Press, New York

Helled R. et al., 2013, in Protostars and Planets VI, University of Arizona Press

Henry G. W., Marcy G. W., Butler R. P., Vogt S. S., 2000, ApJL, 529, L41

Howell S. B. et al., 2014, PASP, 126, 398

Hubeny I., Burrows A., Sudarsky D., 2003, ApJ, 594, 1011

Ibgui L., Burrows A., 2009, ApJ, 700, 1921

Ingraham P. et al., 2014, apjl, 794, L15

Jackson B., Greenberg R., Barnes R., 2008a, ApJ, 678, 1396

Jackson B., Greenberg R., Barnes R., 2008b, ApJ, 681, 1631

Jehin E. et al., 2011, The Messenger, 145, 2

Jenkins J. M., 2002, AJ, 575, 493

Kaib N. A., Raymond S. N., Duncan M. J., 2011, ApJL, 742, L24

Kalas P. et al., 2008, Science, 322, 1345

Kasper M. et al., 2010, in Society of Photo-Optical Instrumentation Engineers (SPIE) Conference Series, Vol. 7735, Society of Photo-Optical Instrumentation Engineers (SPIE) Conference Series, p. 2

Knutson H. A., Charbonneau D., Allen L. E., Burrows A., Megeath S. T., 2008, ApJ, 673, 526

Knutson H. A. et al., 2007, Nature, 447, 183

Knutson H. A., Charbonneau D., Burrows A., O'Donovan F. T., Mandushev G., 2009, ApJ, 691, 866

Knutson H. A., Howard A. W., Isaacson H., 2010, ApJ, 720, 1569, (K10)

Knutson H. A. et al., 2012, ApJ, 754, 22

Koch D. G. et al., 2010, ApJL, 713, L79

Kozai Y., 1962, AJ, 67, 591

Leger A. et al., 2009, A&A, 506, 287

Lewis N. K. et al., 2013, ApJ, 766, 95

Li S.-L., Miller N., Lin D. N. C., Fortney J. J., 2010, Nature, 463, 1054

Lovis C. et al., 2011, A&A, 528, A112

Machalek P., McCullough P. R., Burke C. J., Valenti J. A., Burrows A., Hora J. L., 2008, ApJ, 684, 1427

Machalek P., McCullough P. R., Burrows A., Burke C. J., Hora J. L., Johns-Krull C. M., 2009, ApJ, 701, 514

Macintosh B. et al., 2006, in Society of Photo-Optical Instrumentation Engineers (SPIE) Conference Series, Vol. 6272, Society of Photo-Optical Instrumentation Engineers (SPIE) Conference Series, p. 0

Madhusudhan N., 2012, ApJ, 758, 36

Madhusudhan N. et al., 2011, Nature, 469, 64

Madhusudhan N., Knutson H., Fortney J. J., Barman T., 2014, Protostars and Planets VI, 739

Madhusudhan N., Seager S., 2009, ApJ, 707, 24

Madhusudhan N., Seager S., 2010, ApJ, 725, 261

Mahtani D. P. et al., 2013, MNRAS, 432, 693

Mahtani et al. D. P., in prep.

Majeau C., Agol E., Cowan N. B., 2012, ApJL, 747, L20

Mancini L. et al., 2014, aa, 562, A126

Mandel K., Agol E., 2002, ApJL, 580, L171

Marcy G. W., Butler R. P., Williams E., Bildsten L., Graham J. R., Ghez A. M., Jernigan J. G., 1997, AJ, 481, 926

Marois C., Macintosh B., Barman T., Zuckerman B., Song I., Patience J., Lafrenière D., Doyon R., 2008, Science, 322, 1348

Maxted P. F. L. et al., 2013, MNRAS, 428, 2645

Maxted P. F. L., Serenelli A. M., Southworth J., 2015, A&A, 575, A36

Mayor M. et al., 2003, The Messenger, 114, 20

Mayor M., Queloz D., 1995, Nature, 378, 355

Mazeh T. et al., 2013, ApJS, 208, 16

McLaughlin D., 1924, ApJ, 60, 22

Memo S., 2010, Spitzer memo.
http://ssc.spitzer.caltech.edu/warmmission/news/21oct2010memo.pdf

Menou K., Rauscher E., 2009, ApJ, 700, 887

Micela G., Bakos G. Á., Lopez-Morales M., Maxted P. F. L., Pagano I., Sozzetti A., Wheatley P. J., 2014, Experimental Astronomy

Middelkoop F., 1982, A&A, 107, 31

Ming Y., Hui-Gen L., Hui Z., Jia-Yi Y., Ji-Lin Z., 2013, ApJ, 778, 110

Montalto M. et al., 2012, MNRAS, 427, 2757

Moutou C. et al., 2014, MNRAS, 444, 2783

Nesvorný D., Kipping D. M., Buchhave L. A., Bakos G. Á., Hartman J., Schmitt A. R., 2012, Science, 336, 1133

Noyes R. W., Hartmann L. W., Baliunas S. L., Duncan D. K., Vaughan A. H., 1984, ApJ, 279, 763

Noyes R. W., Weiss N. O., Vaughan A. H., 1984, ApJ, 287, 769

Nymeyer S. et al., 2011, ApJ, 742, 35

O'Donovan F. T., Charbonneau D., Harrington J., Madhusudhan N., Seager S., Deming D., Knutson H. A., 2010, ApJ, 710, 1551

Parmentier V., Showman A. P., Lian Y., 2013, aa, 558, A91

Pepe F. et al., 2013, Nature, 503, 377

Philip A. G. D., Upgren A. R., Janes K. A., 1991, Precision Photometry: Astrophysics of the Galaxy. L. Davis Press

Pollacco D. et al., 2008, MNRAS, 385, 1576

Pollacco D. L. et al., 2006, PASP, 118, 1407

Pont F., Zucker S., Queloz D., 2006, MNRAS, 373, 231

Press W. H., Teukolsky S. A., Vetterling W. T., Flannery B. P., 1992, Numerical Recipes in C (2Nd Ed.): The Art of Scientific Computing. Cambridge University Press, New York, NY, USA

Queloz D., 2006, Nature, 439, 400

Quintana E. V. et al., 2013, ApJ, 767, 137

Rasio F., Ford E., 1996, Science, 274, 954

Rossiter R., 1924, ApJ, 60, 15

Rouan D., Baglin A., Copet E., Schneider J., Barge P., Deleuil M., Vuillemin A., Léger A., 1998, Earth Moon and Planets, 81, 79

Sanchis-Ojeda R., Rappaport S., Winn J. N., Levine A., Kotson M. C., Latham D. W., Buchhave L. A., 2013, ApJ, 774, 54

Schwarz G., 1978, The Annals of Statistics, 6, 461

Seager S., Dotson R., 2010, Exoplanets, Space Science Series. University of Arizona Press

Seager S., Mallén-Ornelas G., 2003, ApJ, 585, 1038

Sing D. K., Lopez-Morales M., 2009, A&A, 493, L31

Sing D. K., Vidal-Madjar A., Désert J.-M., Lecavelier des Etangs A., Ballester G., 2008, ApJ, 686, 658

Skowron J. et al., 2014, ArXiv e-prints

Smalley B. et al., 2010, A&A, 520, A56

Smith A. M. S. et al., 2012, A & A, 545, A39

Smith A. M. S., Anderson D. R., Skillen I., Cameron A. C., Smalley B., 2011, MNRAS, 416, 2096

Southworth J., 2008, MNRAS, 386, 1644

Southworth J., 2010, MNRAS, 408, 1689

Southworth J., 2011a, MNRAS, 417, 2166

Southworth J., 2011b, MNRAS, 417, 2166

Southworth J., 2012, MNRAS, 426, 1291

Southworth J. et al., 2009a, MNRAS, 399, 287

Southworth J. et al., 2009b, ApJ, 707, 167

Southworth J. et al., 2009c, MNRAS, 396, 1023

Southworth J., Mancini L., Maxted P. F. L., Bruni I., Tregloan-Reed J., Barbieri M., Ruocco N., Wheatley P. J., 2012, MNRAS, 422, 3099

Southworth J. et al., 2010, MNRAS, 408, 1680

Spiegel D. S., Silverio K., Burrows A., 2009, ApJ, 699, 1487

Steffen J. H. et al., 2013, MNRAS, 428, 1077

Steffen J. H. et al., 2012a, MNRAS, 421, 2342

Steffen J. H. et al., 2012b, ApJ, 756, 186

Stetson P. B., 1987, PASP, 99, 191

Stevenson K. B. et al., 2012, ApJ, 754, 136

Subaru Telescope Press Release, 2011. http://subarutelescope.org/Pressrelease/2010/12/20/index.html3

Swain M. et al., 2013, Icarus, 225, 432

Szabó R., Szabó G. M., Dálya G., Simon A. E., Hodosán G., Kiss L. L., 2013, A&A, 553, A17

Tegmark M. et al., 2004, Physical Review D, 69, 103501

Todorov K., Deming D., Harrington J., Stevenson K. B., Bowman W. C., Nymeyer S., Fortney J. J., Bakos G. A., 2010, ApJ, 708, 498

Todorov K. O. et al., 2012, ApJ, 746, 111

Tregloan-Reed J., Southworth J., 2013, MNRAS, 431, 966

Triaud A. H. M. J. et al., 2010, A&A, 524, A25

Wall J. V., Jenkins C. R., 2003, Practical Statistics for Astronomers. University of Cambridge

Wang J., Fischer D. A., Horch E. P., Huang X., 2015, ApJ, 799, 229

Werner M. W. et al., 2004, ApJS, 154, 1

Wheatley P. J. et al., 2010, arXiv:1004.0836

Wheatley P. J. et al., 2013, in European Physical Journal Web of Conferences, Vol. 47, European Physical Journal Web of Conferences, p. 13002

Wilson O. C., 1978, ApJ, 226, 379

Wong I. et al., 2014, ApJ, 794, 134

Zahnle K., Marley M., Freedman R., Lodders K., Fortney J., 2009, ApJ, 701

Zeng L., Sasselov D., 2013, PASP, 125, pp. 227

Zhou G., Bayliss D. D. R., Kedziora-Chudczer L., Salter G., Tinney C. G., Bailey J., 2014, MNRAS, 445, 2746